


## FORMS

 <b>Report Documentation Page</b>			
1. Report No. Final		2. Government Accession No.	
4. Title and Subtitle Effect of Boron on Intergranular Hot Cracking in Ni-Cr-Fe Superalloys Containing Niobium		3. Recipient's Catalog No. N/A	
7. Author(s) R. G. Thompson		5. Report Date June 22, 1990	
9. Performing Organization Name and Address University of Alabama at Birmingham Department of Materials Engineering UAB Station, Birmingham, AL 35294		6. Performing Organization Code N/A	
12. Sponsoring Agency Name and Address National Aeronautics & Space Administrators Washington, D.C. 20546-001 NASA/Marshall Space Flight Center Marshall Space Flight Center, AL 35812		8. Performing Organization Report No. N/A	
15. Supplementary Notes		10. Work Unit No. N/A	
16. Abstract Solidification mechanisms had a dominant influence on microfissuring behavior of the test group. Carbon modified the Laves formation significantly and showed that one approach to alloy design would be balancing carbide formers against Laves formers. Boron's strong effect on microfissuring can be traced to its potency as a Laves former. Boron's segregation to grain boundaries played at best a secondary role in microfissuring.		11. Contract or Grant No. NAS8-38084	
17. Key Words (Suggested by Author(s)) Microfissuring      DTA Liquation cracking      Sulfur Boron      Segregation Carbon      Solidification		13. Type of Report and Period Covered Final	
18. Distribution Statement		14. Sponsoring Agency Code	
19. Security Classif. (of this report)	20. Security Classif. (of this page)	21. No. of pages	22. Price

(NASA-CR-186714) EFFECT OF BORON ON  
INTERGRANULAR HOT CRACKING IN Ni-Cr-Fe  
SUPERALLOYS CONTAINING NIOBIUM Final Report  
(Alabama Univ.) 115 p CSCL 11F

N90-26115

Unclass  
G3/26 0294764

## Table of Contents

Executive Summary .....	1
Introduction .....	2
Procedures and Results .....	2
Specimen Selection .....	2
Specimen Chemistry .....	3
Thermal History of Alloys .....	3
Microstructural Analysis .....	3
Differential Thermal Analysis .....	4
Gleeble Thermal Analysis .....	4
Scanning Auger Microscopy .....	5
Discussion .....	5
Alloy Melting and Solidification .....	5
Simulated Welding Thermal Cycles .....	7
Interfacial Segregation Effects .....	7
Microfissuring Susceptibility Mechanisms .....	8
Conclusions .....	11
Figure 1 - Gleeble Thermal Cycle .....	12
Figure 2 - DTA Runs of Commercial Alloy 718 .....	13
Figure 3 - Solidification of Boron Alloys .....	14
Figure 4 - Typical Range of Sulfur Segregation .....	15
Table 1 - Alloy Chemistry .....	16
Table 2 - Thermal History of Alloys .....	17
Table 3 - Summary of DTA Results .....	18
Table 4 - Results of Scanning Auger Microscopy Peak Height Ratios to Ni .....	19
Table 5 - General Electric Report of Spot Varestraint Cracking Data on Alloys of this Study .....	21
Appendix A - Metallography .....	A
Appendix A2 - SEM, Energy Dispersion X-ray Analysis of Precipitates in Samples .....	A2.1
Appendix A3 - TEM, Energy Dispersion X-ray Analysis of Particles in Thin-Films .....	A3

Appendix B - Differential Thermal Analysis (DTA) of Test Specimens of Micrographs of DTA Solidification Microstructures .....	B1
Appendix C - Microstructures from Gleeble Weld Simulation .....	C
Appendix D - Scanning Auger Microscope (SAM) .....	D
NASA Form 1626 .....	22

## EXECUTIVE SUMMARY

The role of boron in intergranular liquation cracking (microfissuring) is now better understood. Boron both increases the solidification range of 718-type alloy compositions and promotes Laves phase formation. This combination is detrimental to welding because it increases the probability that liquid will still exist on the grain boundaries of the heat affected zone (HAZ) when residual stress begins to develop. This is the situation that is most likely to result in microfissuring.

A new discovery of this study is that carbon can mitigate the deleterious effect of boron by changing the solidification to primary carbide formation instead of Laves. This has the effect of reducing the solidification range and reducing the possibility of the simultaneous existence of grain boundary liquid and residual stress. This was consistent in the differential thermal analysis, Gleeble simulation, and vareststraint test results.

Data on the intergranular chemistry of 718-type alloys shows that boron is not strongly segregated intergranularly. However, these results establish that sulfur and phosphorus do segregate to the grain boundaries. It also revealed that sulfur strongly segregates to the carbide and Laves phase interfaces. This explains the ability of sulfur to increase the solidification range of carbide formation.

It can be concluded that boron should be avoided if it is not necessary for high temperature mechanical properties. Sulfur and phosphorus should be minimized. Carbon can be increased in certain chemical compositions to good benefit. However, excess carbides can increase the solidification time thus they should generally be avoided.

Finally, there should be a generally applicable alloying scheme that balances the carbide formers against the Laves formers to eliminate Laves formation and thus produce a microfissuring resistant alloy.

**FINAL REPORT**  
**"EFFECTS OF BORON ON INTERGRANULAR HOT**  
**CRACKING IN NI-CR-FE SUPERALLOYS CONTAINING NB"**

**Introduction**

The primary mission of this research was to define the mechanistic role of boron in microfissuring of 718-type superalloys. Because of the experimental procedure selected, it was also necessary to evaluate the roles of sulfur and carbon on microfissuring.

Nickel base alloys, particularly those like alloy 718 are susceptible to HAZ microfissuring during welding. This is unfortunate since the 718 base composition is expected for use in current and future advanced engine designs. The need to eliminate microfissuring stems from the facts that; it is difficult to inspect for, fatigue strength is compromised due to the loss of crack initiation time, and it can act as a point of stress concentration and site for hydrogen embrittlement growth.

Previous studies(1-3) have not identified the mechanism by which various alloy and impurity elements degrade or benefit the resistance to microfissuring. It was proposed that the only serious detrimental element was boron(1). This is in contrast to other studies(2,3) that have found elements like sulfur and carbon deleterious to microfissuring resistance. It is difficult to experimentally isolate an element like boron which is present in concentrations of only a few parts-per-million.

This study took the approach of using a series of eight alloys that formed an experiment involving C, B, and S. The approach was to examine the effect of these elements individually and in combination. By studying the mechanisms by which these alloys influenced microfissuring, it was possible to determine the individual and synergistic effects that they have on microfissuring.

**Procedures and Results**

**Specimen Selection**

A 2x3 factorial experiment using carbon, sulfur and boron was attempted from a set of alloys produced by General Electric. The alloy set was based on modifications to an alloy 718 type base chemistry. The desired combinations were:

	B	1	1	1	1	2	2	2	2	1-low concentration
	C	1	1	2	2	1	2	1	2	2-high concentration
	S	1	2	1	2	1	1	2	2	
<b>Spec#</b>		<b>20</b>	<b>14</b>	<b>11</b>	<b>10</b>	<b>13</b>	<b>12</b>	<b>3</b>	<b>5</b>	
<b>Subs#</b>			<b>25</b>	<b>22</b>	<b>27</b>					

Although it was hoped that #11 and #14 would allow Si to substitute for C and P to substitute for S, it was determined after some

experimentation to abandon that substitution. Instead, alloys 22 and 25 were substituted for 11 and 14 respectively. These alloys were from a different study but they met the general requirement of high and low S and C with a 718 base composition. Alloy 27 was used as a control to give overlap with alloy 10 to test the validity of mixing the two alloy groups. It was found that these substitutions had some draw backs. First, each of the substitutes contained typical impurities or alloy levels different from the test group. These elements, such as silicon, promoted Laves phase and the low carbon level still caused carbide precipitation. Thus the substitutes behaved more like a combination of elements similar to alloy 5. They did provide some insight as discussed in the following sections.

### Specimen Chemistry

The chemistry of each alloy in the study is given in Table 1.

### Thermal History of Alloys

The thermal processing of the alloys is documented in Table 2.

### Microstructural Analysis

#### Light Microscope

Micrographs of initial microstructures used for DTA, Gleeble and Auger are presented in Appendix A1 for all specimens. Metallography on initial materials was performed using standard metallographic procedures. Oxalic acid was used for all etchings. The micrographs show relatively clean, equiaxed microstructure after a 1100C thermal anneal.

#### SEM Micrographs

Micrographs at approximately 3000x are presented in Appendix A2.1 for specimens 5, 10, 12, 13, and 14. These micrographs show typical precipitate structures and the locations of analysis points used for chemical identification.

#### SEM Energy Dispersive X-ray Analysis

EDS analysis of precipitates found in specimens 10, 12, 14, 20, 5, and 13 are presented in Appendix A2.2. The spectra are divided into four general types:

- spectra that resemble matrix (A2.2.1)
- spectra that resemble Nb-carbide (A2.2.2)
- spectra that resemble Laves phase (A2.2.3)
- spectra that resemble delta ( $\text{Ni}_3\text{Nb}$ ) (A2.2.4)

Spectra that resemble matrix are characterized by small Nb peak, small Ti peak, and major Ni, Cr, and Fe peaks in descending intensities. Spectra that resemble Nb-carbide are characterized by a primary Nb peak

and a small Ti, Ni, Cr, and Fe peaks. The spectra of Laves phase have roughly equal Nb, Ni, Fe, and Cr peaks. The spectra of delta phase have a Ni peak larger than found in the matrix and roughly equal Nb, Fe, and Cr peaks.

#### TEM Energy Dispersive Analysis

TEM-EDS analysis of specimens 12(A3.1), 13(A3.2), and 20(A3.3) are presented in Appendix A3. A TEM micrograph of specimen 12 is presented in A3.1. Specimen 20 was practically devoid of precipitates. The other extreme was specimen 12 which had a multitude of precipitates from which one area was examined in detail. From this area, 16 spectra were taken from various particles. These spectra show several things of importance. First, the particles are embedded in the matrix and the spectra of all particles has a strong matrix signature (A3.1.1) Two particles are typical in this matrix; a Nb-carbide particle identified by the large Nb and Ti peaks (A3.1.2) and a carbide containing Nb, Hf and Zr (A3.1.3). The Hf and Zr appear at the expense of the Ti and Nb. Spectra in A3.1.4 is of a Nb-carbide that has little matrix embedded with it.

Particles found in specimen 13 were very small and from the spectra in A3.2.1 appear to be oxide inclusions.

#### Differential Thermal Analysis

DTA results for all specimens are presented in Appendix B. The melting and solidification curves contain characteristic shapes which have been marked matrix, NbC and/or Laves. When carbon is present, the DTA results show a characteristic shoulder that appears with the initial stage of bulk melting and the final stage of primary gamma solidification. This shoulder is the proeutectic  $\gamma + \text{NbC}$  reaction. A lower temperature reaction which appears on cooling is the eutectic reaction believed to involve  $\gamma + \text{carbide} + \text{Laves}$ .

The solidus and liquidus temperatures for each reaction are found by taking the point where the tangent to the baseline meets the tangent to the reaction curve of interest. These temperatures are presented in Table 3.

The reproducibility of these results is presented in Appendix B2. Note that these results are very reproducible.

Micrographs of the alloy microstructure following the DTA thermal cycle are presented in Appendix B3. Also presented in B3 are chemical spectra from SEM-EDS analysis. These are presented to correlate the DTA reaction peaks with the phase responsible for the reaction.

#### Gleeble Thermal Analysis

Gleeble experiments were conducted at four peak temperatures (1190C, 2010C, 1230C, and 1250C) which encompass all of the liquation

temperatures found in these alloys. These Gleeble thermal cycles are shown in Figure 1. Samples were heated to the peak temperature and quenched in water to "freeze in" the microstructure for metallographic analysis. The Gleeble results are summarized in Table 3 and micrographs of the samples from the Gleeble tests are presented in Appendix C.

### Scanning Auger Microscopy

SAM was performed on all samples in the test group. About 400 spectra were taken of surface chemistries of grain boundaries, cleavage facets, ductile ruptures, carbides, Laves and other second phase particles. Samples were prepared by cutting 1mmx1mmx10mm specimens from the alloys. The specimens were then put into a hydrogen charging cell to embrittle the grain boundaries for fracture in the SAM. The parameters for hydrogen embrittlement are given in Appendix D1. Samples for SAM were placed in the SAM and fractured using a slow strain rate. The fractured surfaces were then analyzed using standard SAM techniques. Typical spectra from each sample are presented in D2. The results from the SAM study are presented in Table 4. Since over 400 spectra were taken, the presentations represent typical results obtained.

In order to determine if the observed Auger chemical spectra is a surface film or bulk chemistry, depth profiles were made by sputtering the surface under analysis with argon ions. It can be assumed that the spectra presented are for unsputtered surfaces unless otherwise designated. The spot probe used to obtain chemical spectra was 1 to 3 microns in diameter. The largest diameter was usually used unless particle size or other features required a smaller probe size.

### Discussion

#### Alloy Melting and Solidification

The DTA was used to evaluate the effects of B, C, and S on alloy melting and solidification. The method for doing this can be shown with DTA data from a commercial alloy 718 as presented in Figure 2. The initial microstructure is free of Laves phase but contains some NbC. When this microstructure is heated (Figure 2A) a smooth baseline is established until the NbC-solidus (1245C) is reached. The sample absorbs heat during NbC melting and then the rate of this reaction changes as bulk(gamma) melting begins. During solidification (Figure 2B), the gamma solidification reaction is encountered first followed by a second exothermic peak associated with NbC proeutectic solidification. The final solidification reaction is the system eutectic which has been described as a gamma+Laves+carbide. The microstructure verifies this solidification sequence. Note that this 718 microstructure contains a significant amount eutectic which, when heated, produces an endothermic reaction associated with eutectic melting (Figure 2C). The NbC and gamma melting reactions are also identified. This exercise points out that alloy 718 melting reactions, that is the heating of the initial microstructure, are dependent on the initial microstructure. This is clear from Figure 2 where the Laves



peak is present during the heating segment of the DTA run only if Laves was present in the initial microstructure. However, the solidification reactions which occur during cooling are dependent on chemistry and solidification rate as seen in Figure 3. The DTA is capable of evaluating this behavior.

#### Interstitial Free (#20)

The interstitial free alloy had the smallest freezing range, 48C, due to the lack of carbide or eutectic solidification reactions (Bl.6).

#### Single Level Effects B(13) S(25) C(22)

The effect of a single interstitial element can be dramatic, as with B (alloy 13) which acts as a strong Laves former and increases the solidification range to 174C (a factor of 3.5 increase over alloy 20) (Bl.5). It should be noted that phosphorus (alloy 14) has a similar effect (Bl.9). Carbon (alloy 22) also has a dramatic effect in that it produces carbide precipitation which increases the solidification range, gamma liquidus to carbide solidus, to 116C (note that this solidification range did not include the Laves reaction which presumably appeared because the alloy contains other interstitials) (Bl.7). Sulfur appears to have a dual effect by accentuating both the carbide and Laves reactions (alloy 25 had residual carbon and Laves formers) (Bl.8).

The alloy set had a varying Nb content that may have had an effect on the magnitude of the Laves reactions. For example, alloy 20 had 4.4wt% Nb while alloy 13 had 5.4wt% Nb. While B appears to be a strong Laves former the observed behavior is probably influenced by the increase in Nb concentration. However, in defense of boron's influence on Laves formation it can be noted that boron not only increased the amount of Laves formation, it also changed its morphology from that of a gamma-Laves mixture (which is normally reported in alloy 718) to a blocky, unmixed Laves precipitate.

#### Binary Interactions BC(12) SC(10,27) SB(3)

Binary interactions proved very important. The BC interaction was most dramatic with carbon causing a complete solidification change from strongly Laves eutectic in the boron alloy (13) to completely carbide (Bl.4) in the BC alloy (12). This observation should be tempered with the fact that BC alloy had the low Nb concentration (4.4wt%) which could contribute to the loss of Laves formation. The solidification range for BC was very small, only 62C. The SC interaction produced strong carbide formation and a microstructure like the BC alloy. The solidification range, 60C, was the same as that of the BC alloy (Bl.3). (Alloy 27 which contained other interstitials had the same solidification range as #22 when considering the gamma liquidus to carbide solidus range). Alloy 3, used as the SB binary interaction alloy, actually contained phosphorus also which, based on P behavior, probably accentuated the Laves eutectic behavior (B and P gave

identical DTA results). However, the solidification range for alloy 3 was smaller than for either P or B alone.

#### Ternary Interaction BCS(5)

Alloy 5 actually contained both P and Si along with B, C, and S. The solidification range was large as would be expected for Laves solidification. The ternary interaction was similar to that found for 718 base alloys with typical interstitial levels.

These results show that the interstitial chemistry of alloy 718 can be thought of in terms of carbide or Laves formers. The Laves formers tend to extend the solidification range while the carbide formers have little effect on it. However, the carbide formers can suppress the Laves formation as was the case with the BC alloy and thereby dramatically reduce the solidification range. Commercial 718 alloy behaves like alloy #5 in this study in that the commercial chemistry cannot offset the multitude of Laves formers and a duplex carbide/Laves solidification is obtained with the attendant large solidification range (Figure 3).

#### Simulated Welding Thermal Cycles

Gleeble simulation of the weld heating cycle was used to examine the relationship of the DTA melting reactions done at a slow heating rate to that of the weld HAZ which is a relatively rapid heating rate. The Gleeble results do indeed reinforce what was discovered in the DTA work:

- B, P, and SB(P) alloys(13,14,3) initiate liquation below 1190C. These were all strong Laves forming alloys.
- BCS alloy(5) initiated liquation at about 1210C.
- CS and BC alloys(10,12) both initiate liquation between 1210C and 1230C. These are the carbide forming alloys.
- Alloy 20 initiates liquation at 1250C.

The Laves formers, in the absence of carbon, produce a wide melting range and presumably an even wider solidification range. The addition of carbon apparently raises the eutectic thus giving a smaller melting and solidification range. If enough carbon (relative to Laves formers) is present, then the eutectic is completely suppressed and melting and solidification ranges are similar to the interstitial free alloy.

#### Interfacial Segregation Effects

The distribution of the interstitial elements could have significant effects on the solidification and melting behavior of the alloys. If the interstitial elements are strongly segregated on the boundaries or at the phases which melt, they can more strongly influence the behavior than if they are dilutely and homogeneously distributed. Also, whether or not the interstitials partition to the solid or liquid during solidification strongly affects the solidification of the alloy.

The general finding of this study was that when the alloy was doped with an interstitial, that interstitial appeared as a grain boundary segregant. Thus B, S, and P all appeared on the grain boundaries when they were present in the alloy at high concentration. However, sulfur was always found at the NbC-matrix interface in huge amounts (10 to 40 times greater at the precipitate interface than on the grain boundary) as seen in Figure 4. Sputtering to remove the surface layer removed the sulfur concentration thus proving that it was not part of the bulk chemistry of either the matrix or carbide. Phosphorus was also found to be more often associated with grain boundary segregation than either sulfur or boron. Boron was found on the grain boundaries but never associated with any precipitate. However, sulfide particles were often found on fracture surfaces.

These findings provide significant new information about the possible role of boron on microfissuring. This can be evaluated by comparing the BC alloy (12) and the B alloy (13). Note that both alloys are doped with B and both have about the same B level on the grain boundaries. As will be noted later, the BC alloy exhibited little cracking (using the total crack length as the measure of cracking) compared to alloy B. Since there was a large difference in the cracking behavior but little difference in the grain boundary boron concentration, intergranular boron must not be the cause of cracking susceptibility. This strongly suggests that the solidification range has a much greater effect on microfissuring than does the intergranular segregation level exhibited by boron.

The sulfur concentration at the carbide-matrix interface has the most potential to dramatically affect liquation and thus microfissuring. The reason for this is the large concentrations of sulfur possible at the precipitate-matrix interface. Furthermore, it appeared that sulfur was also heavily segregated at the Laves-matrix interface although this was difficult to confirm due to the eutectic nature of the Laves phase and its general Auger spectrum that looks like matrix. The obvious implication is that S partitions to the liquid phase during solidification and is eventually rejected during the final solidification stages, which are either carbide formation or eutectic formation. Due to the common association of S with the carbide interface, it must be concluded that some mutual chemical attraction is present. The potential effect of this S segregation could be on controlling the shape of the carbide or on the liquation behavior of the carbide-matrix interface. However, the alloys containing sulfur were not found to be exceptionally prone to microfissuring nor did they exhibit eutectic behavior in the Gleeble rapid heating tests.

#### Microfissuring Susceptibility Mechanisms

Table 5 presents microfissuring susceptibility results from spot vareststraint tests on the alloys of this study. Although both the total crack length and average crack length are reported, all correlations and references to cracking in this report refer to the total crack length measurement. Past experience of this researcher and others has

been that total crack length correlates best with cracking susceptibility. In the General Electric test group, the strong Laves formers in the absence of carbon gave the greatest level of microfissuring. Just as Laves appears to strongly promote microfissuring, carbon appears to improve microfissuring resistance. It should once again be noted that alloys containing carbon also had the lower niobium content which could also contribute to reduced Laves formation. Sulfur gave no strong indication as to its effect on microfissuring from the cracking data.

### **Effect of Boron on Microfissuring Susceptibility**

Boron promotes a long solidification range through promotion of Laves formation. The boron containing alloy(13) had the lowest melting point in the Gleeble weld simulation tests which indicates its ability to promote intergranular liquation during rapid heating. Alloy 13 also had the most microfissuring susceptibility. However, such behavior is not necessarily unique to boron. It was also observed in the behavior of phosphorus additions(alloy 14). Although researchers at General Electric found that only boron significantly promoted microfissuring based on statistical results of many compositions, this research shows on a specimen by specimen basis that the boron effect on microfissuring is not unique. Any combination of elements which cause a long solidification range and promote a significant amount of low-melting eutectic phase will have similar microfissuring susceptibilities.

Boron's contribution to microfissuring susceptibility can be negated through elimination of the low melting phase which it promotes. Such was the case with alloy 12 where the carbon level was increased and the Nb level reduced so that the Laves solidification was suppressed. The result was that microfissuring was also suppressed even in the presence of a large boron concentration.

### **Effect of Solidification on Microfissuring Susceptibility**

The solidification temperature range appears to be a good first order approximation for microfissuring susceptibility. This finding should be modified to also encompass the amount of eutectic formed at the low-temperature end of solidification. Examples of short solidification range and low microfissuring are alloys 20, 12, and 10. Alloy 5 is an exception, but it contained 0.1C which modified its solidification such that it had a very small Laves DTA peak. Although technically it had a large solidification range, the amount of Laves formed may have been insignificant in terms of microfissuring. The large carbon levels (possibly combined with smaller Nb contents) used in this study appear to alter the solidification path sufficiently to reduce microfissuring, probably by reducing the volume fraction of Laves phase. This was most notable when the Laves was completely precluded from the solidified microstructure.

A large solidification range with significant Laves present, as indicated by the size of the DTA peak, produced the most

microfissuring(total crack length). This is evidenced in alloys 13, 14 and 3.

#### **Effect of Segregation on Microfissuring Susceptibility**

A dramatic result of this study was found in alloys 12(CB) and 13(B). Both had about the same level of grain boundary B segregation but alloy 12 had very little microfissuring(total crack length) similar to the clean alloy (20). This must be a reflection of the dominating effect that solidification has on microfissuring as compared to the observed B segregation to grain boundaries.

Sulfur appears to have little to do with the microfissuring levels of this study. That might be due to the fact that most of the sulfur was either tied-up as a sulfide or segregated to the carbide/matrix and eutectic/matrix interfaces. This may be why sulfur appeared to have no effect. Sulfur may really just have the ~~same~~ effect on all specimens because it was found in both samples with and without sulfur doping.

#### **Interstitial Concentrations**

The absolute concentrations of interstitials used in this study are well above those normally encountered in commercial alloy 718. This may be the cause of certain differences in trends between the General Electric test group and the auxiliary test group (22, 25, 27), especially with respect to the carbon concentration. The auxiliary test group all showed a tendency to Laves formation which is probably a result of elements like Si which increase Laves formation. The large carbon concentration in conjunction with the lower Nb content of the carbon-bearing alloys in the General Electric group probably changed the solidification relative to the commercial carbon level. This allowed the GE alloys to solidify completely as primary carbide and completely avoid Laves formation.

## Conclusions

1. Boron increases microfissuring by its potency as a Laves former and the resultant long solidification range that Laves-forming alloys have.
2. Boron's behavior is not different in this respect from an element like P which gave strikingly similar results to B in both the DTA and microfissuring tests.
3. The segregation of boron to grain boundary surfaces is evident in alloys doped with 0.01wt% B. However, this level of segregation is not sufficient to offset solidification effects associated with primary carbide solidification compared to solidification to a Laves eutectic.
4. Boron is not unique in its ability to promote microfissuring or in the mechanism through which it promotes microfissuring.
5. Carbon, in large concentrations (>0.1%), can significantly alter the solidification behavior of the 718-type composition and completely reverse the effect of a Laves former like boron. This was observed in a boron alloy with 5.4wt% Nb and a boron-carbon alloy with 4.4wt% Nb.
6. Sulfur segregates strongly to carbide and eutectic interfaces whether or not it is present as an intentionally added dopant. This probably explains why sulfur additions did not strongly alter microfissuring data.
7. Results from Gleeble simulation of the welding heating cycle provided information to verify that results from DTA studies were applicable to microfissuring studies.
8. Alloy design for minimizing microfissuring should consider various options such as:
  - extra low interstitial compositions,
  - high carbon compositions,
  - compositions which balance carbide formers against Laves formers, and
  - compositions which can be made free of second phase precipitates which liquate and produce a liquid with a large solidification range.

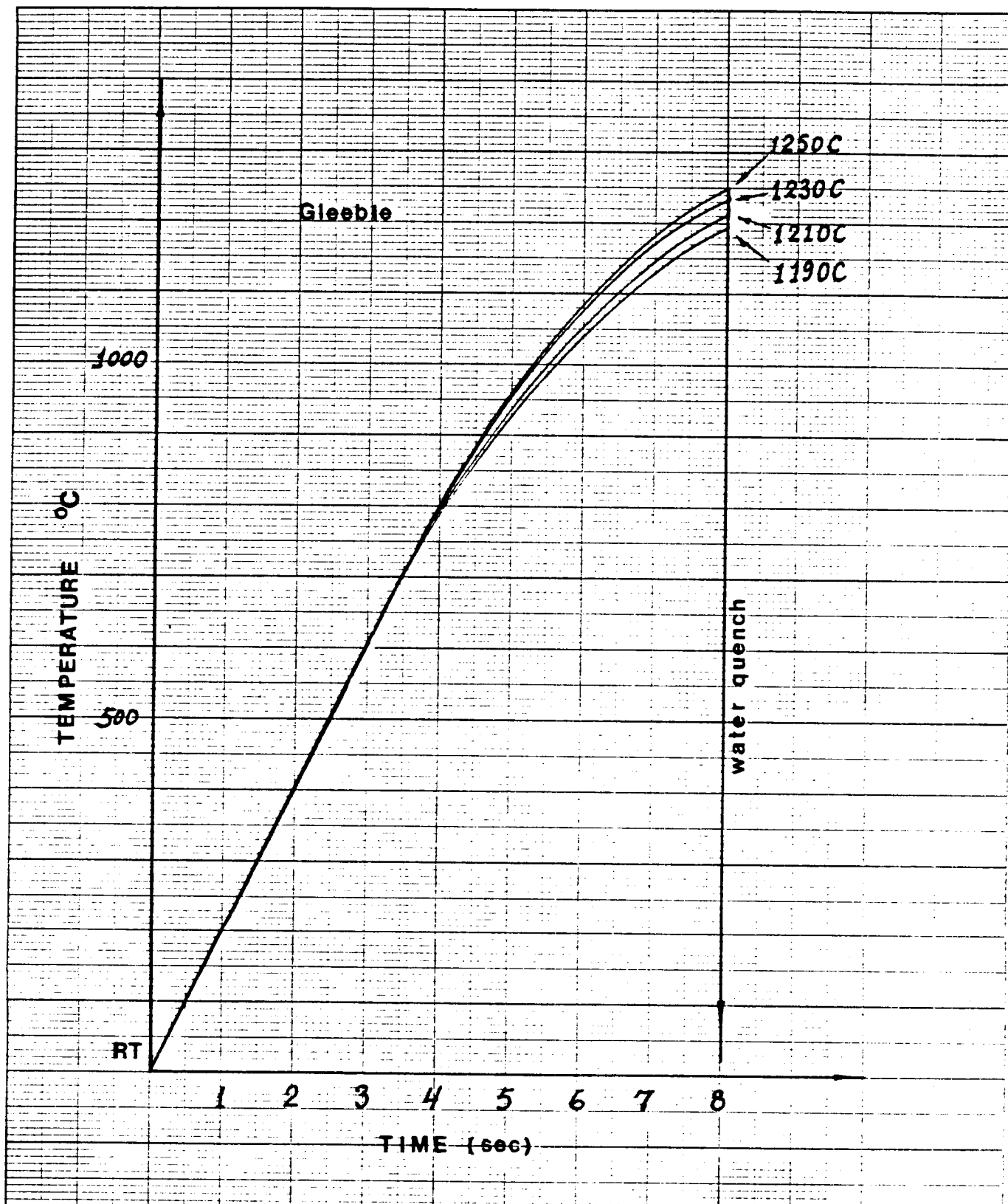
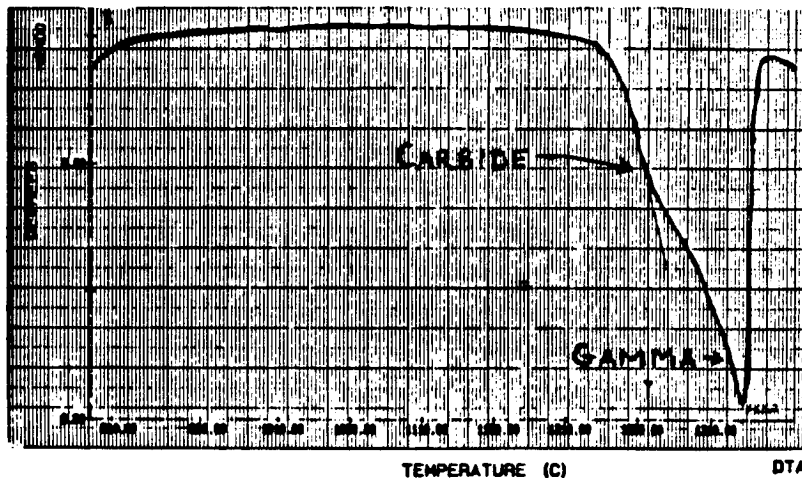


Figure 1. Thermal cycle used in Gleeble machine for simulation of HAZ heating.

photo



photo

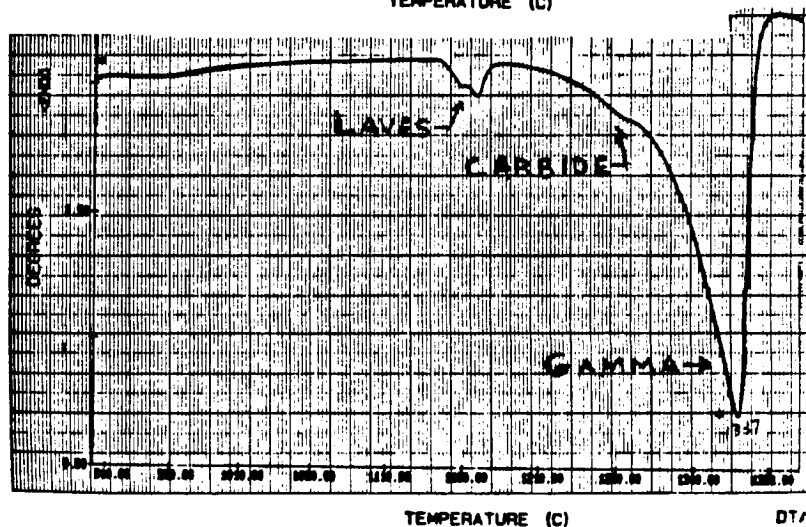
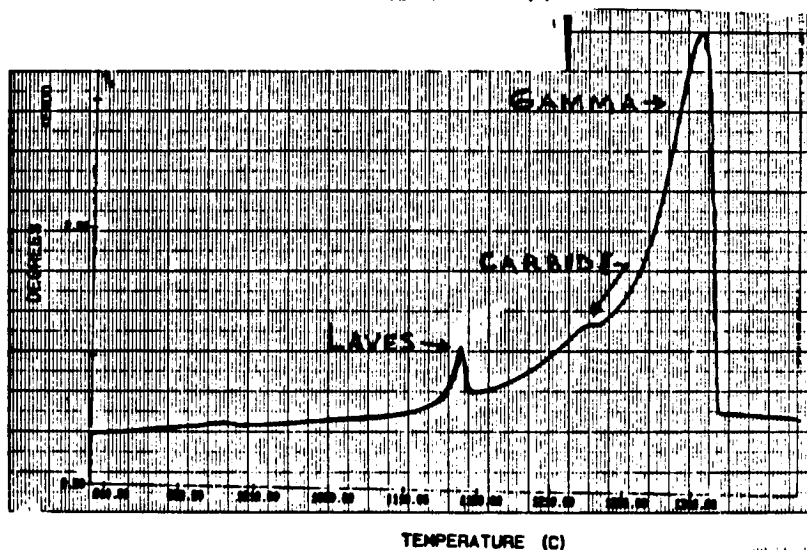
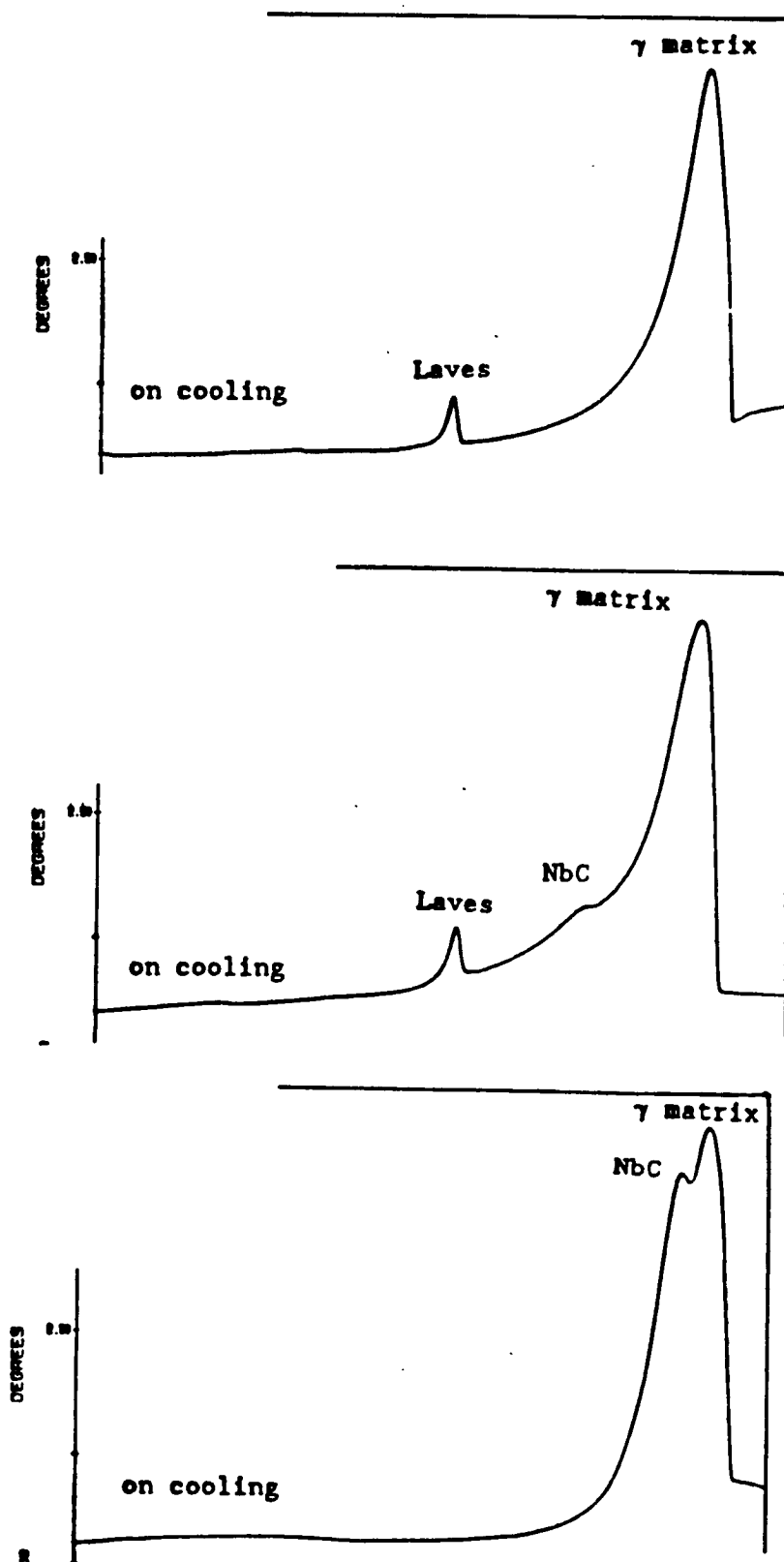


Figure 2. DTA runs of commercial alloy 718 melted with only carbide (top), solidified (middle), and melted with Laves and carbide which resulted from solidification in DTA (bottom). Accompanying micrographs of microstructure prior to first melting (top) and after solidification in DTA (bottom).

ORIGINAL PAGE IS  
OF POOR QUALITY





ORIGINAL PAGE IS  
OF POOR QUALITY

Figure 3. Composite of solidification of Boron alloys 13 (top), commercial alloy 718 (middle), and 12 (bottom). Note how carbon eliminates the Laves phase.

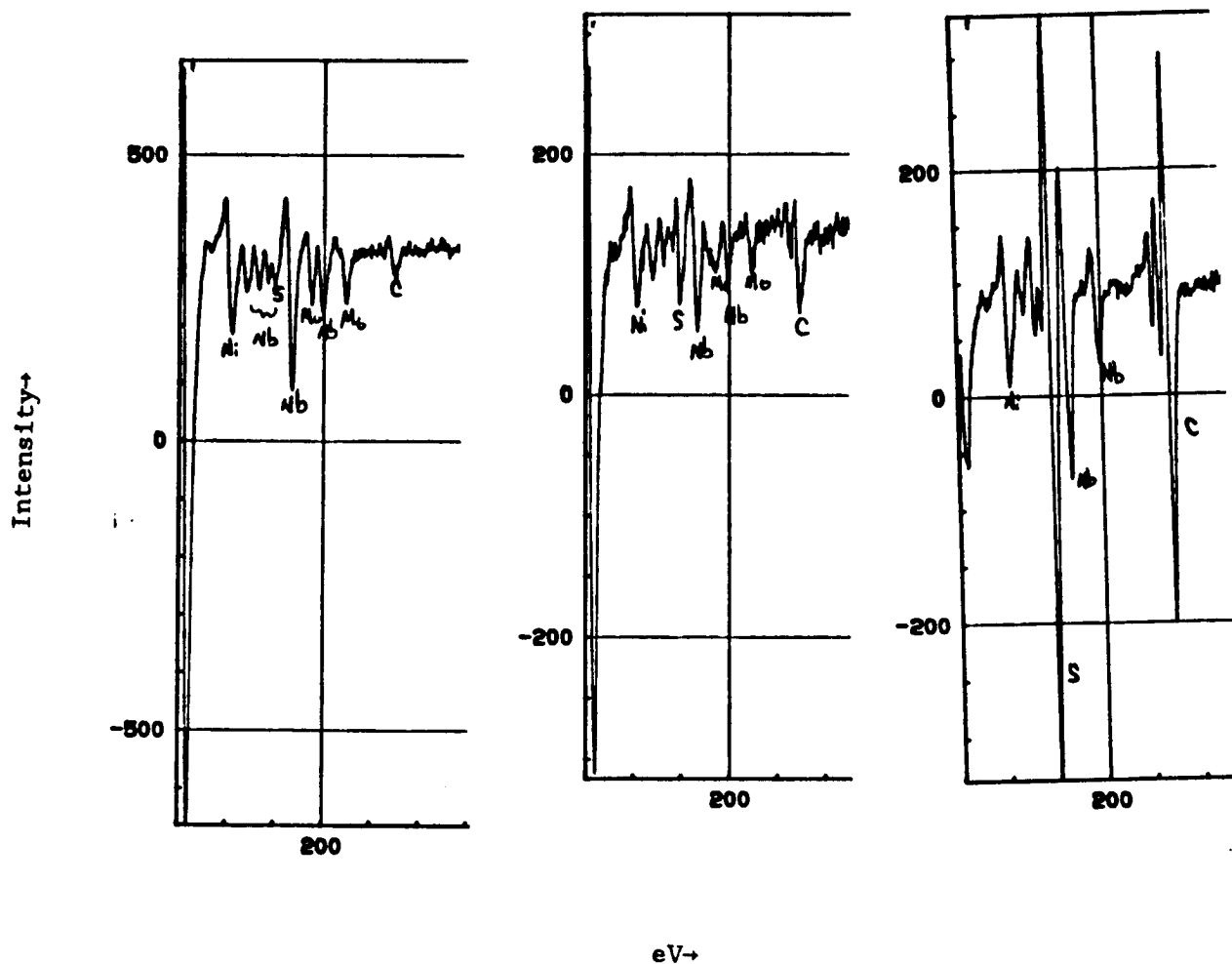


Figure 4. Composite of alloy 27 showing typical range of sulfur segregation. Far left is "clean" boundary after sputtering, middle is typical grain boundary sulfur segregation in doped alloy. Far right is huge sulfur segregation at a carbide/matrix interface typical of all samples.

TABLE 1

ALLOY CHEMISTRY

Alloy	Ni	C	Si	S	P	Co(Nb)	B	Fe	Mo	Hf	Zr	Cr	Al	Ti
3 (BS(P))	Bal	LAP	LAP	0.015	0.015	5.4	0.01	17	3.5	LAP	0.1	20	0.5	1.0
5 (BSC +)	Bal	0.1	0.35	0.015	0.015	4.4	0.01	17	3.5	LAP	LAP	20	0.5	1.0
10 (CS)	Bal	0.1	LAP	0.015	LAP	4.4	LAP	17	3.5	0.1	LAP	20	0.5	1.0
27 (CS +)	53.18	0.065	<0.01	0.09	<0.001	5.07	0.003	Bal	3.15		<0.01	19.17		
12 (CB)	Bal	0.1	LAP	LAP	LAP	4.4	0.01	22	2.5	0.1	0.1	20	0.5	1.0
13 (B)	Bal	LAP	LAP	LAP	LAP	5.4	0.01	17	3.5	0.1	LAP	20	0.5	1.0
14 (P)	Bal	LAP	LAP	LAP	0.015	5.4	LAP	22	3.5	LAP	LAP	20	0.5	1.0
20 (none)	Bal	LAP	LAP	LAP	LAP	4.4	LAP	17	2.5	LAP	LAP	20	0.5	1.0
22 (C +)	53.18	0.065	<0.01	0.003	<0.001	5.07	0.003	Bal	3.15		<0.01	19.17	0.58	1.11
25 (S +)	53.77	0.023	<0.01	0.09	<0.001	4.39	0.002	Bal	3.15		<0.01	20.46	0.53	1.09

TABLE 2

THERMAL HISTORY OF ALLOYS

## First Cold-roll Followed by Anneal

Alloy No.	Starting Thickness	Final Thickness	Reduction (%)
13	0.2404"	0.1850"	23.0
20	0.2437"	0.1876"	24.7
12	0.2534"	0.2154"	15.0
05	0.2480"	0.1882"	24.0
14	0.2480"	0.2169"	12.5
03	0.2542"	0.1895"	25.0
10	0.2395"	0.1801"	24.8
11	0.2534"	0.2154"	15.0

Annealed at 1000C for 30 min. (in a box furnace) followed by air cool.

## Second Cold-roll Followed by Anneal

Alloy No.	Starting Thickness	Final Thickness	Reduction (%)
13	0.1790"	0.1506"	15.9
20	0.1825"	0.1544"	15.4
12	0.2135"	0.1894"	11.3
05	0.1876"	0.1504"	19.4
14	0.2173"	0.2024"	6.9
03	0.1904"	0.1691"	11.2
10	0.1793"	0.1484"	17.2
11	0.1871"	0.1307"	30.1

Annealed for 1 hr. at 1000C and air cooled for 45 min. prior to 3rd cold roll.

## Third Cold Roll of Some of the Alloys to Level Out Sample Thickness

Alloy No.	Starting Thickness	Final Thickness	Reduction (%)
03	0.1638"	0.1609"	1.77
12	0.1887"	0.1767"	6.36
14	0.2010"	0.1853"	7.81

All the rest were not subjected to the 3rd cold roll.

## Final Anneal for Recrystallization

1 hour at 1000C in box furnace followed by air cool, plus  
1 hour at 1100C in box furnace followed by air cool.

## Sample Preparation for Gleeble

3 specimens were cut out of each anneal sample and vacuum sealed and then annealed at 1100C for 1 hour followed by water quench.

TABLE 3

SUMMARY OF DTA RESULTS

## SOLIDIFICATION

Alloy	$\gamma_{\text{liquidus}}$	$\gamma_{\text{solidus}}$	NbC <sub>start</sub>	NbC <sub>finish</sub>	Eutectic	$\Delta T_s^*$
3 (BS (P))	1300	-	-	-	1140	160
5 (BSC+)	1324	-	1284	-	1145	179
10 (CS)	1325	-	1298	1265	-	60
12 (CB)	1332	-	1320	1270	-	62
13 (B)	1319	-	-	-	1145	174
14 (P)	1338	-	-	-	1150	188
20 (none)	1325	1277	-	-	-	48
22 (C+)	1327	-	1279	1209	1102	225
25 (S+)	1330	-	1235	1191	1110	220
27 (CS+)	1327	-	1278	1212	1106	221
Commercial 718	1312	-	1243	-	1140	172

## MELTING

3 (BS(P))	1320	1195	-	-	-	125
5 (BSC+)	1324	-	1290	1250	-	74
10 (CS)	1333	-	1300	1265	-	68
12 (CB)	1338	-	1318	1269	-	69
13 (B)	1321	1225	-	-	-	96
14 (P)	1328	-	-	-	1180	148
20 (none)	1338	1271	-	-	-	67
22 (C+)	1339	-	1293	1246	1159	180
25 (S+)	1345	-	1282	1236	1160	185
27 (CS+)	1340	-	1293	-	1159	181
Commercial 718	1331	-	1270	1245	-	86

\*  $\Delta T_s$  - Solidification Temperature Range ( $^{\circ}\text{C}$ )\*  $\Delta T_m$  - Melting Temperature Range ( $^{\circ}\text{C}$ )

Table 4. Results of Scanning Auger Microscopy Peak Height Ratios to Ni.

Peak Height Ratios*													
Specimen/ Area	P* 119	S 150	Nb 168	B* 179	Mo 222	C 273	N* 281	Ti 419	O 507	Cr 529	Fe 652	Ni 848	Appendix
#3													
g.b.	.23	.06	.16	.03	.08	.19	.15	.07	.16	.62	.24	1.00	D2.1.1
matrix	.00	.02	.13	.00	.03	.17	.12	.07	.21	.48	.21	1.00	D2.1.2
#5													
g.b.	.22	.00	.14	.00	.06	.15	.09	.06	.10	.57	.25	1.00	D2.2.1
g.b. x	.00	.00	.09	.00	.06	.15	.26	.07	.13	.55	.24	1.00	D2.2.1B
matrix	.00	.00	.04	.00	.00	.12	.12	.06	.28	.54	.24	1.00	D2.2.2
carbide	.00	1.90	1.17	.00	.08	2.29	.86	.64	.91	.62	.29	1.00	D2.2.3
carbide x	.00	.18	.85	.00	.07	1.10	.67	.39	.60	.50	.29	1.00	D2.2.3B
carbide +	.00	.00	.83	.00	.11	1.05	.64	.35	.24	.50	.27	1.00	D2.2.3C
#10													
g.b. #1	.00	.04	.12	.02	.05	.18	.15	.05	.09	.53	.23	1.00	D2.3.1
g.b. #2	.00	.11	.13	.02	.06	.24	.16	.06	.06	.58	.23	1.00	D2.3.2
matrix	.00	.05	.08	.00	.03	.11	.09	.08	.24	.67	.30	1.00	D2.3.3
carbide	.31	.63	1.69	.00	.17	2.92	1.08	.82	1.77	.55	.31	1.00	D2.3.4
#12													
g.b. #1	.00	.00	.20	.04	.05	.11	.07	.06	.15	.59	.23	1.00	D2.4.1
g.b. #2	.00	.00	.16	.03	.05	.09	.06	.06	.06	.59	.25	1.00	D2.4.2
matrix	.00	.00	.11	.00	.05	.10	.11	.09	.16	.62	.29	1.00	D2.4.3
#13													
g.b.	.00	.03	.12	.03	.05	.06	.06	.06	.09	.64	.28	1.00	D2.5.1
matrix	.00	.03	.12	.00	.04	.10	.08	.07	.03	.59	.27	1.00	D2.5.2
#20													
g.b. #1	.06	.04	.13	.00*	.08	.24	.09	.07	.48	.68	.27	1.00	D2.6.1
g.b. #1 x	.06	.00	.10	.00*	.04	.07	.30	.10	.13	.63	.26	1.00	D2.6.1B
g.b. #2	.00	.00	.10	.00*	.03	.09	.06	.06	.19	.59	.26	1.00	D2.6.2
matrix	.00	.00	.10	.00*	.04	.12	.09	.09	.26	.64	.26	1.00	D2.6.3
precipitates	.00	.76	.08	.00*	.02	.12	.23	.15	.94	.45	.24	1.00	D2.6.4
#22.1													
g.b. #2	.00	.02	.13	.00	.04	.07	.11	.07	.41	.68	.30	1.00	D2.7.1
g.b. #2 x	.00	.00	.15	.00	.07	.00	.21	.07	.05	.57	.29	1.00	D2.7.1B
matrix	.00	.00	.12	.00	.02	.09	.10	.09	.12	.62	.29	1.00	D2.7.2
carbide	.00	.00	3.86	.00	.00	5.42	1.49	.98	.45	.62	.36	1.00	D2.7.3
eutectic	.00	1.01	.24	.00	.07	.10	.16	.11	.40	.56	.30	1.00	D2.7.4

Specimen/ Area	P*	S	Nb	B*	Mo	C	N*	Ti	O	Cr	Fe	Ni	Appendix
<u>#25.1</u>													
g.b. #1	.00	.01	.11	.00*	.06	.06	.07	.06	.23	.63	.28	1.00	D2.8.1
g.b. #1 x	.00	.02	.12	.00*	.03	.00	.28	.07	.11	.60	.31	1.00	D2.8.1B
matrix	.00	.02	.04	.00*	.03	.06	.07	.05	.25	.63	.33	1.00	D2.8.2
carbonitride	.00	4.00	.68	.00*	.10	1.24	1.32	.85	.88	.46	.39	1.00	D2.8.3
eutectic	.00	.14	.16	.00*	.05	.13	.16	.14	.30	.57	.28	1.00	D2.8.4
<u>#27.3</u>													
g.b.	.00	.14	.20	.00	.08	.15	.14	.12	.36	.70	.33	1.00	D2.3Acast.1
g.b. x	.00	.00	.28	.00	.08	.06	.25	.09	.05	.71	.33	1.00	D2.3Acast.1B
matrix	.00	.00	.15	.00	.05	.06	.14	.09	.20	.56	.27	1.00	D2.3Acast.2
carbide	.00	4.61	1.88	.00	.12	3.42	2.64	2.07	1.08	.63	.40	1.00	D2.3Acast.3
<u>#27.4</u>													
g.b.	.00	.09	.05	.00	.02	.10	.05	.06	.14	.59	.25	1.00	D2.3B(1093).1
matrix	.00	.00	.22	.00	.10	.08	.14	.10	.23	.84	.34	1.00	D2.3B(1093).2
carbide	.00	.00	1.33	.00	.10	1.72	.57	.41	.58	.62	.32	1.00	D2.3B(1093).3
eutectic	.00	2.12	.81	.00	.09	.80	.77	.60	.41	.48	.24	1.00	D2.3B(1093).5
carbide/ interface	.00	1.81	.97	.00	.07	1.34	.80	.58	.57	.59	.29	1.00	D2.3B(1093).4

\* element peak height relative to Ni peak height (element/Ni)

x sputtered

+ resputtered

\* Because P overlaps with a small Nb peak, it must have a ratio of about 1:1 with Nb to be significant.

\* B overlaps with chlorine spectra

\* N overlaps with Ti spectra

TABLE 5

General Electric Report of Spot Vareststraint  
Cracking Data on Alloys of This Study

Alloy	Total Crack Length (mm) Homogenized at 1093C	Average Crack Length (mm) Homogenized at 1093C
3 (BS (P))	6.8	0.97
5 (BSC +)	2.3	0.36
10 (CS)	2.6	0.21
12 (CB)	3.6	0.89
13 (B)	10.1	1.21
14 (P)	9.9	0.51
20 (none)	1.3	0.33
From UAB Study		
22 (C +)	18.2	0.72
25 (S +)	19.4	-
27 (CS +)	21.84	0.66



**Appendix A**  
**Metallography**

**A1 Metallography of Initial Microstructures**

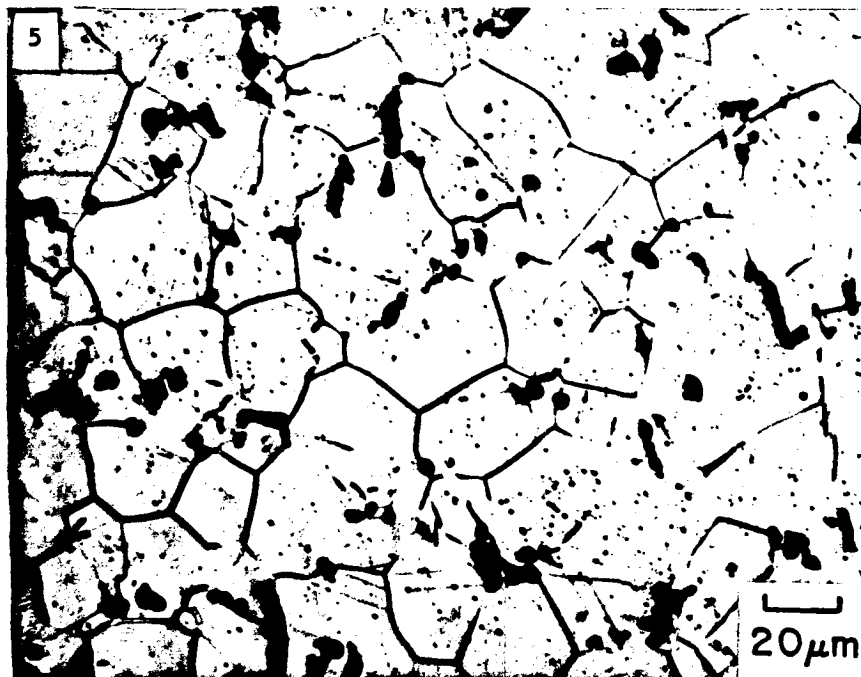
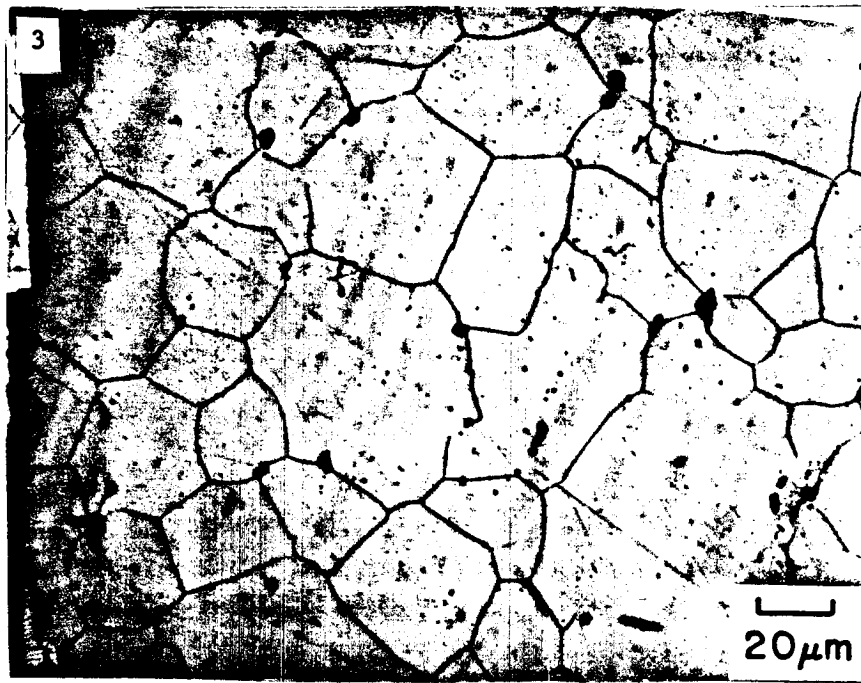
- A1.1 Alloys 3 (BS) and 5 (BSC)
- A1.2 Alloys 10 (CS) and 11 (Si)
- A1.3 Alloys 12 (BC) and 13 (B)
- A1.4 Alloys 14 (P) and 20 (none)
- A1.5 Alloys 22 (C+) and 25 (S+)
- A1.6 Alloy 27 (CS+)

**A2 SEM-EDS of Typical Phases Found in the Initial Microstructures**

- A2.1 Matrix
- A2.2 Nb-Carbide
- A2.3 Laves Phase
- A2.4 Delta Phase

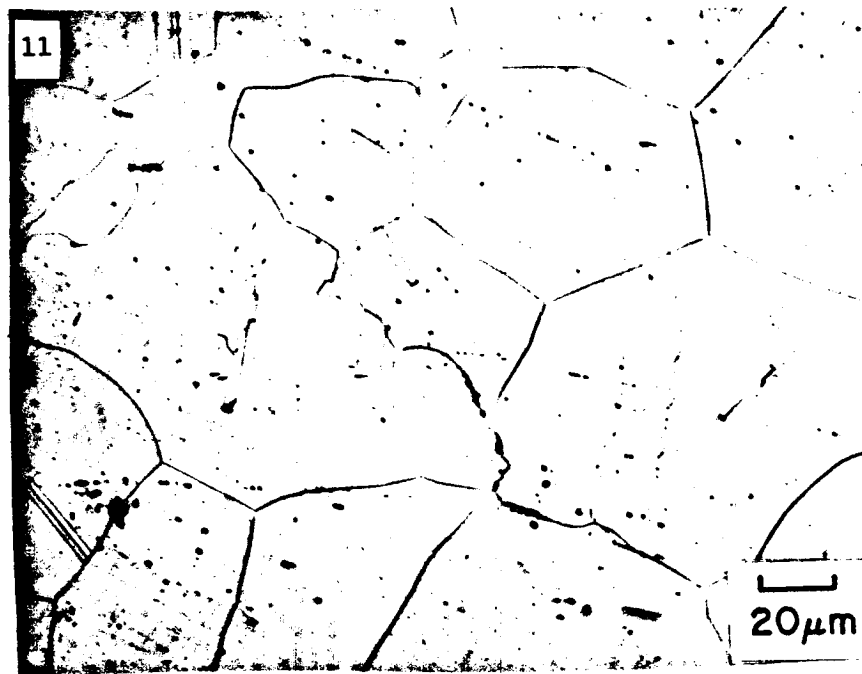
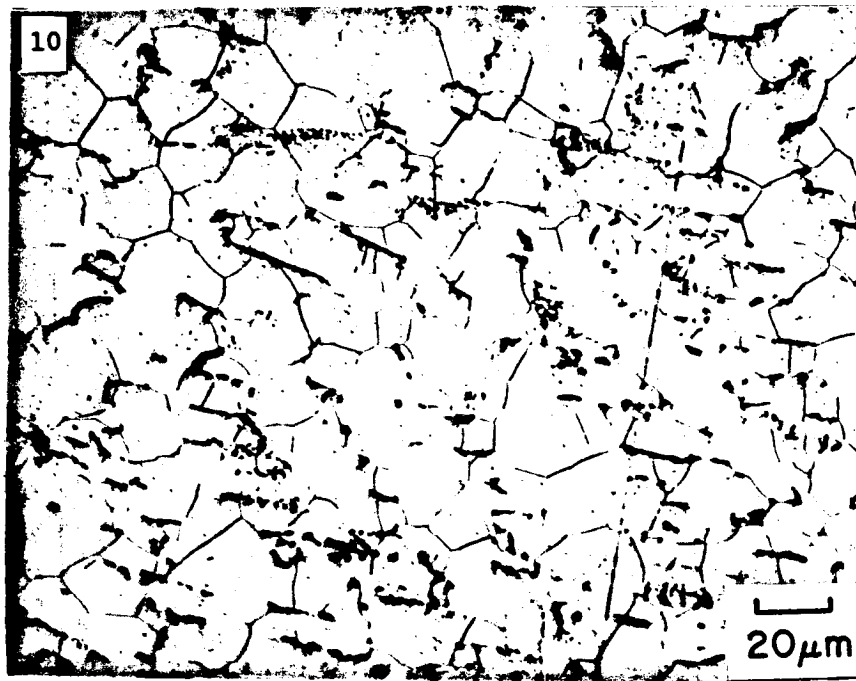
**A3 TEM-EDS of Typical Phases Found in the Initial Microstructures**

- A3.1 Alloy 12 (BC)
- A3.2 Alloy 13 (B)
- A3.3 Alloy 20 (none)



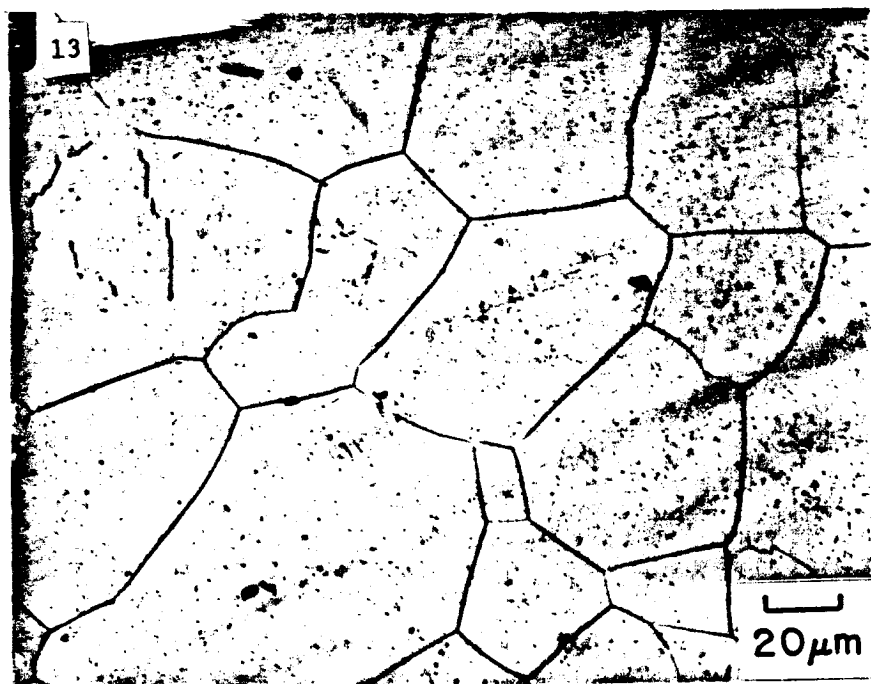
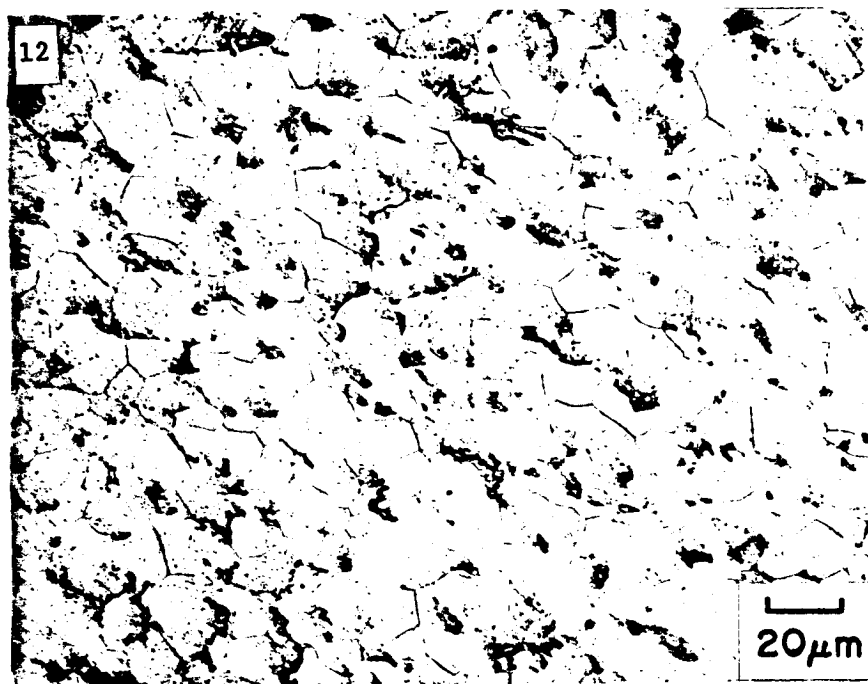
Top - Microstructure of Alloy 3 (BS) after 1100C homogenization.

Bottom - Microstructure of Alloy 5 (BCS) after 1100C homogenization.



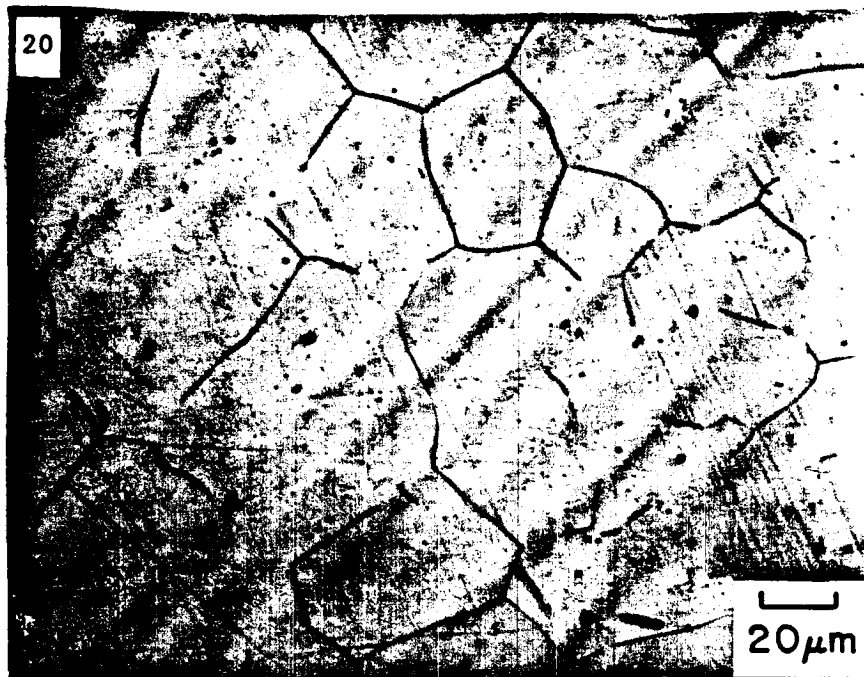
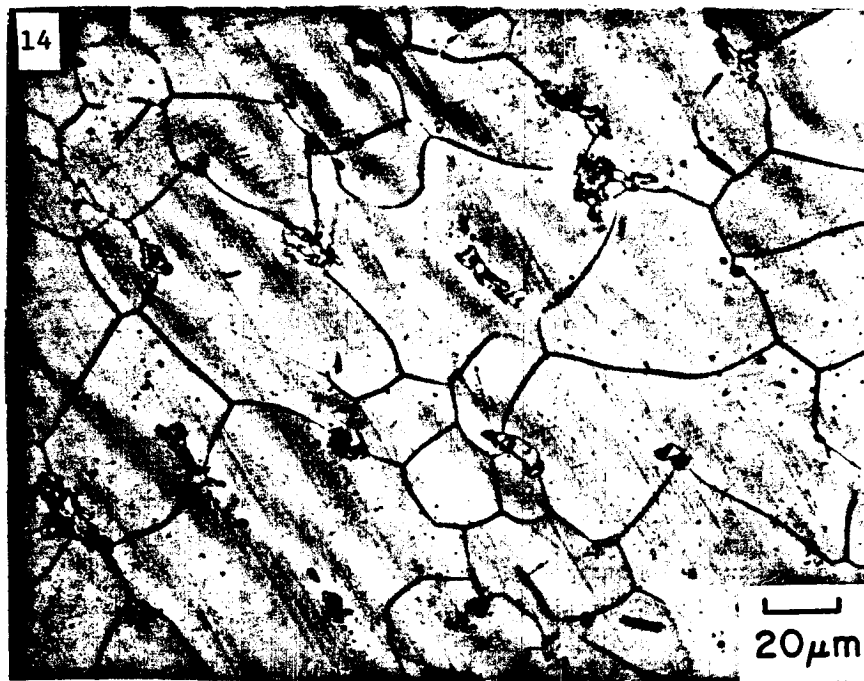
Top - Microstructure of Alloy 10 (CS) after 1100C homogenization.

Bottom - Microstructure of Alloy 11 (Si) after 1100C homogenization.



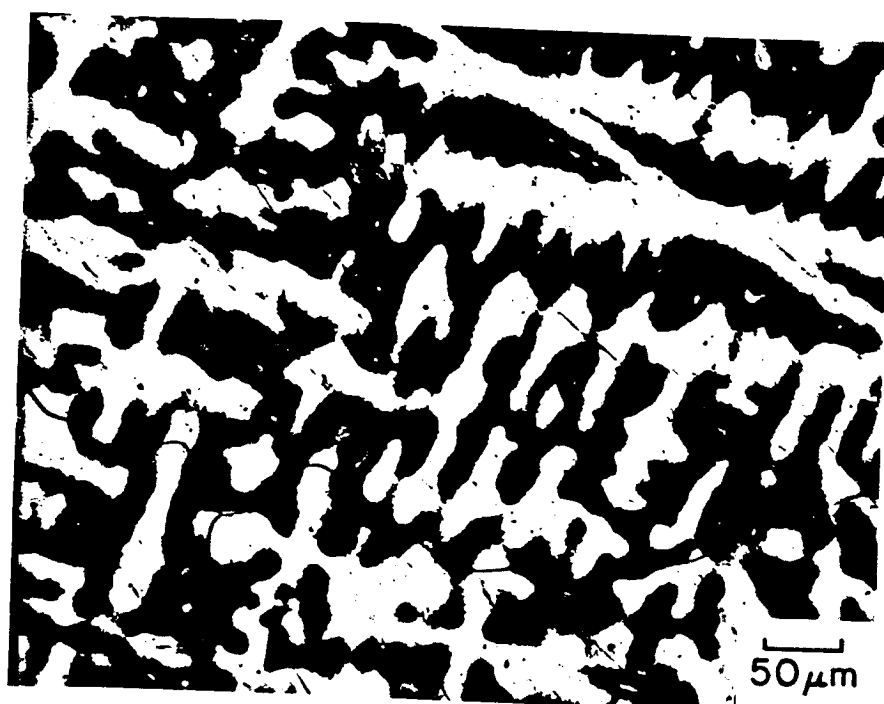
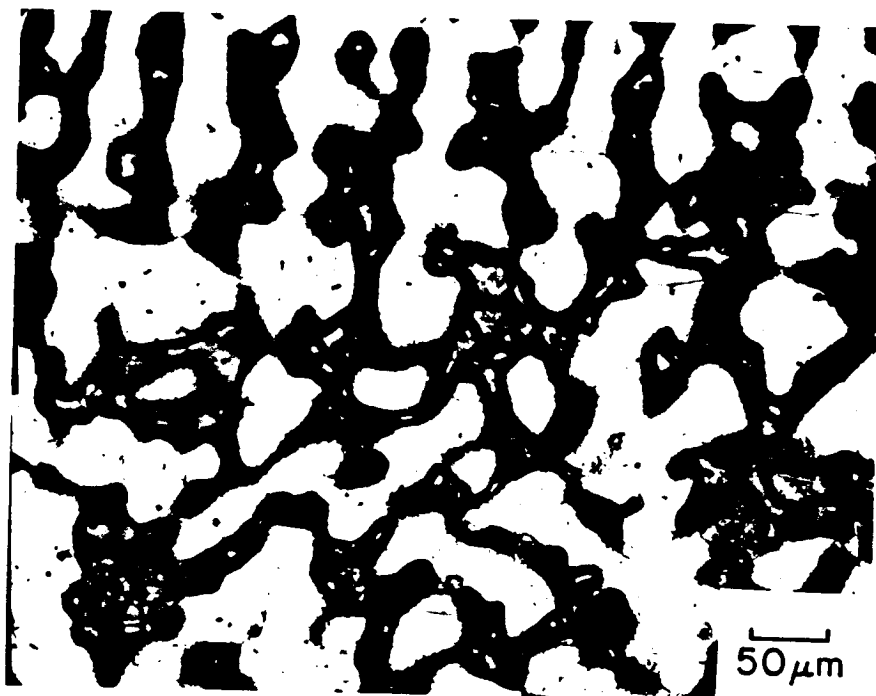
Top - Microstructure of Alloy 12 (BC) after 1100C homogenization.

Bottom - Microstructure of Alloy 13 (B) after 1100C homogenization.



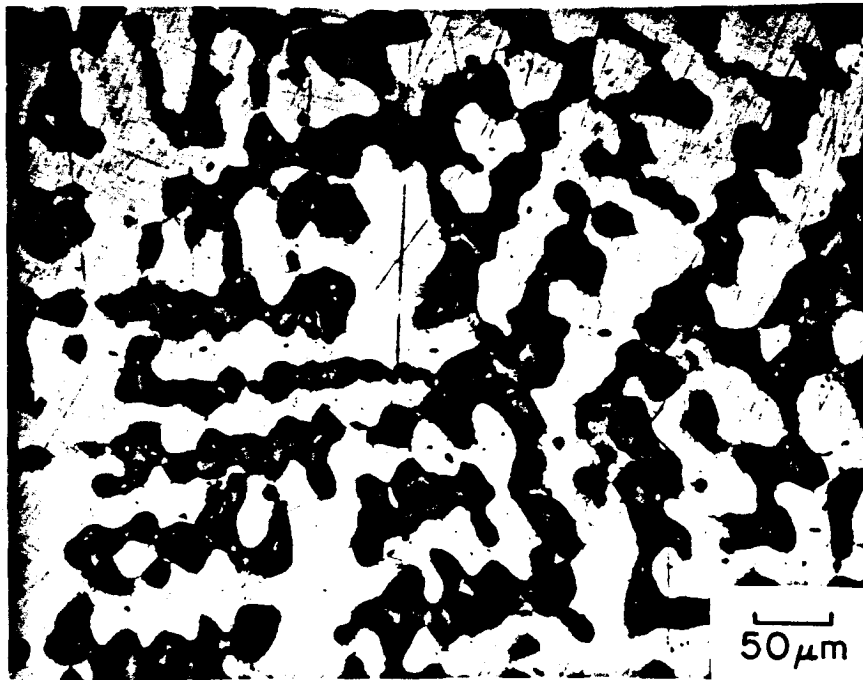
Top - Microstructure of Alloy 14 (P) after 1100C homogenization.

Bottom - Microstructure of Alloy 20 (none) after 1100C homogenization.



Top - Microstructure of Alloy 22 (C+) as cast.

Bottom - Microstructure of Alloy 25 (S+) as cast.



Microstructure of Alloy 27 (CS+) as cast.

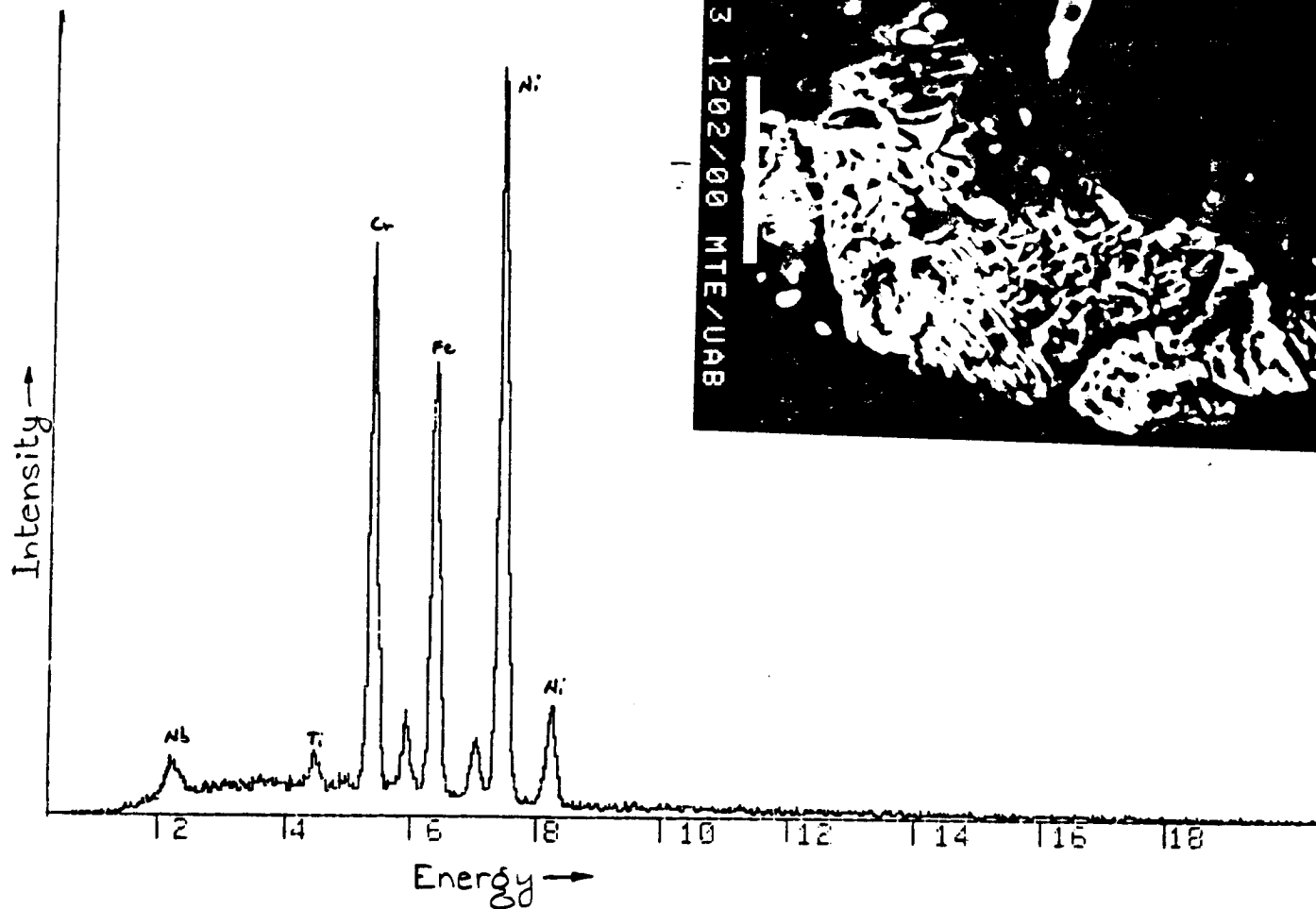
## **Appendix A2**

### **SEM - Energy Dispersive X-ray Analysis of Precipitates in Samples**

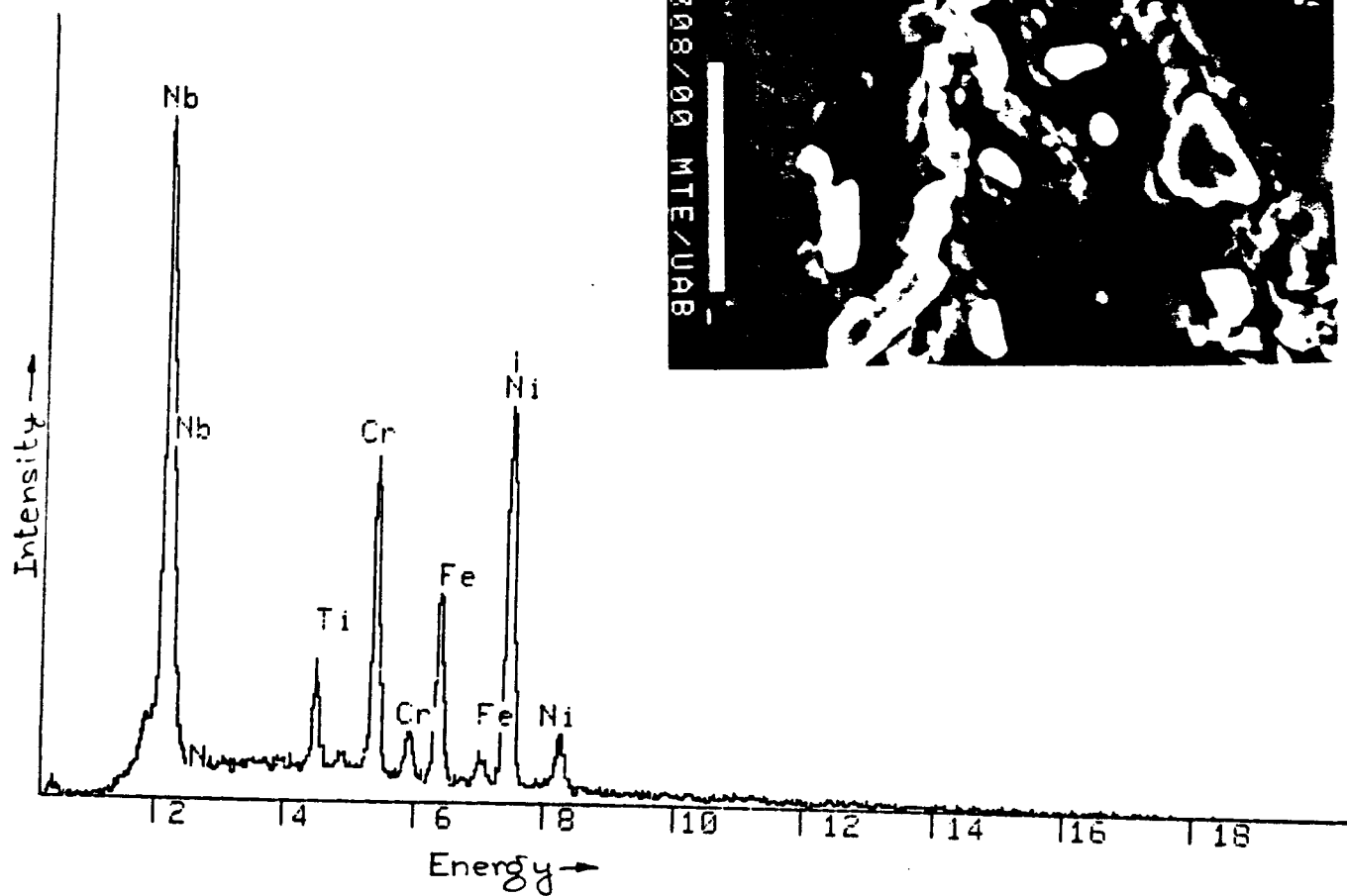
- Spectra that resemble matrix           A2.1
- Spectra that resemble Nb-carbide       A2.2
- Spectra that resemble Laves Phase     A2.3
- Spectra that resemble delta ( $\text{Ni}_3\text{Nb}$ )   A2.4

**(See SEM micrographs for location of spots)**



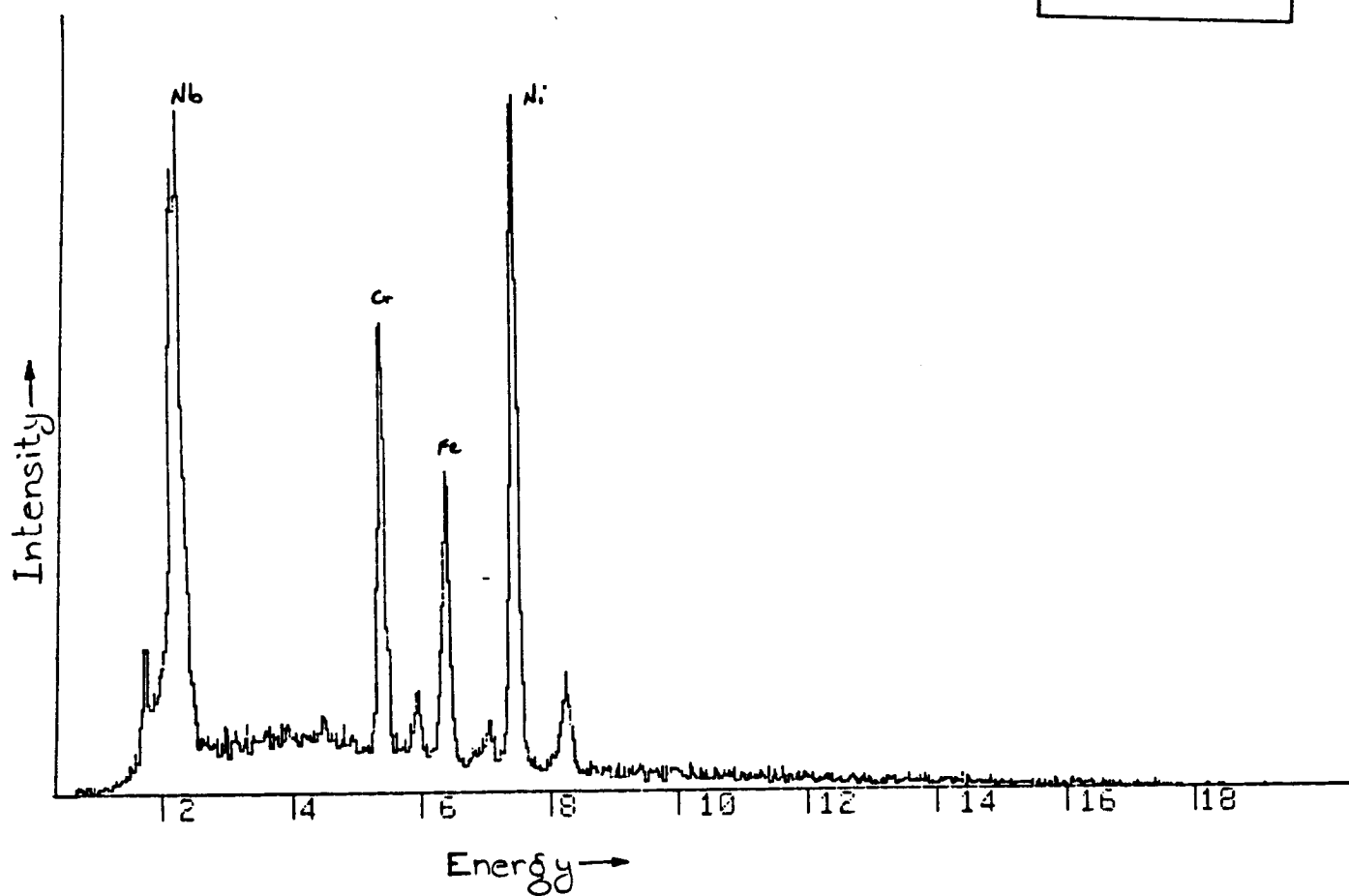


SEM-EDS of spot M from Specimen 12 which was typical matrix.

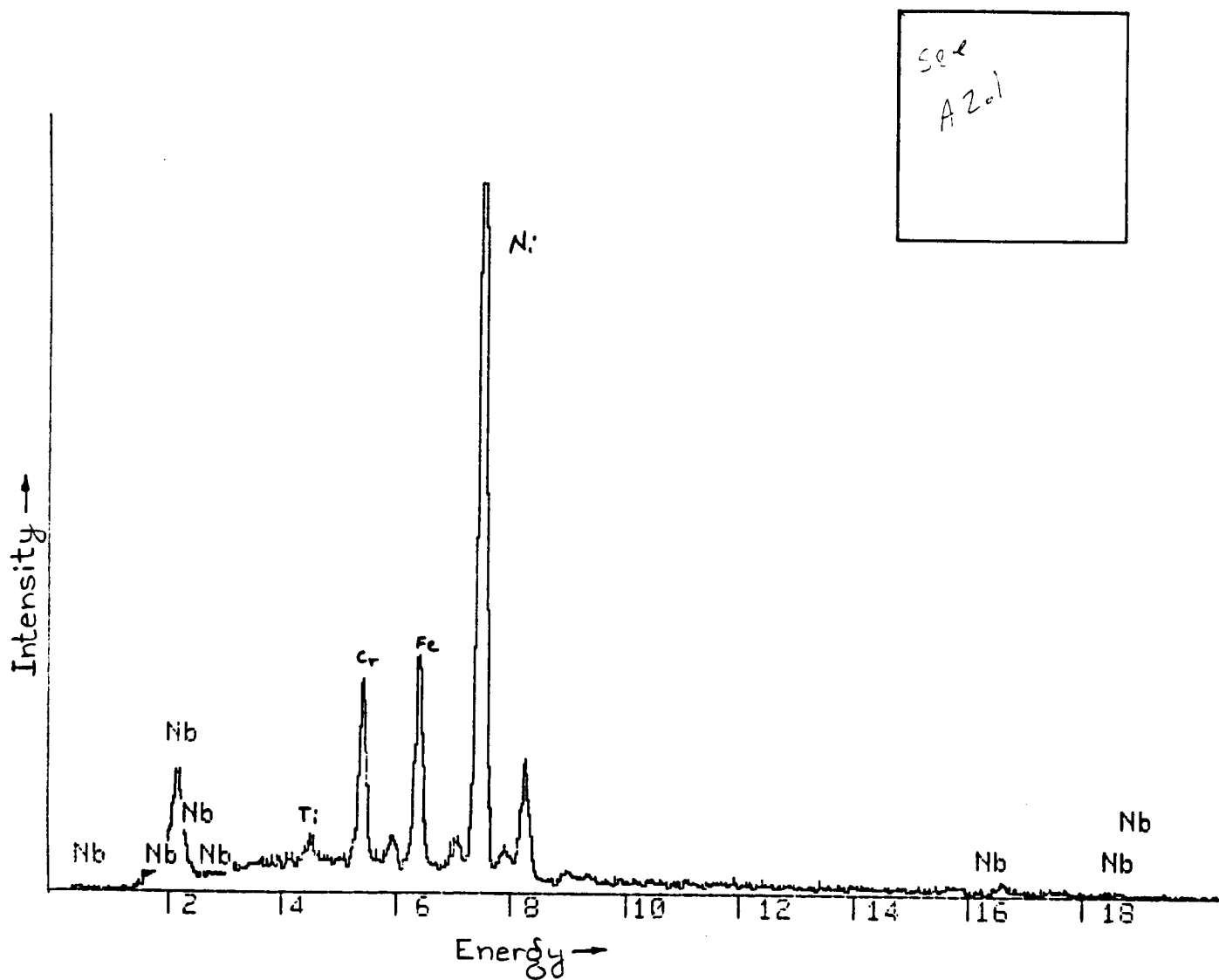


SEM-EDS of spot 2 in Specimen 5 typical of NbC particles.

see  
A2.2



SEM-EDS of spot 1 in Specimen 5 typical of Laves phase.

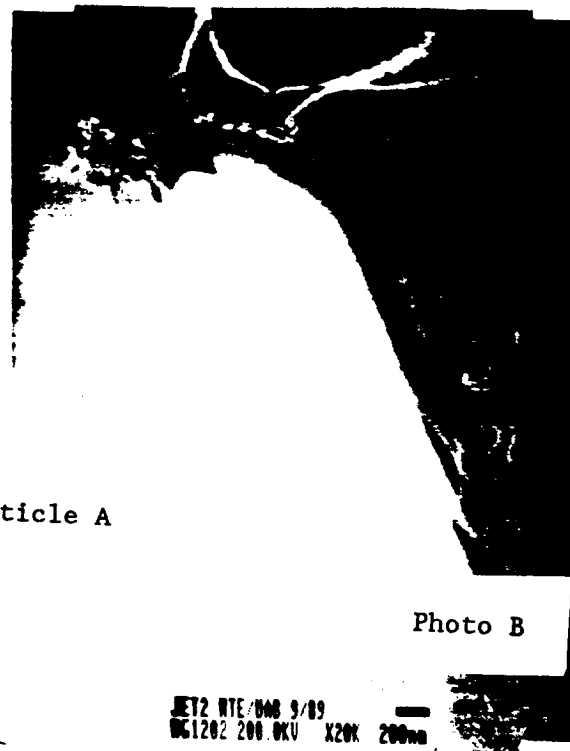
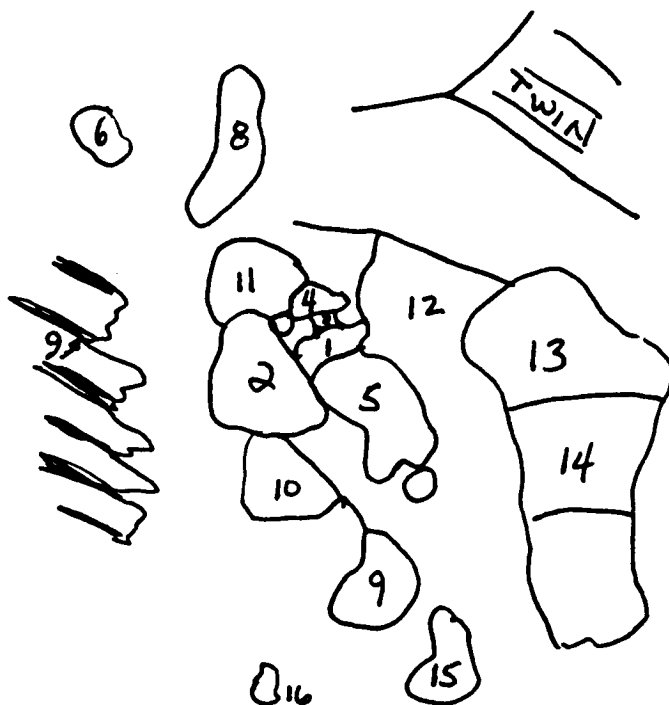


SEM-EDS of spot 3 in Specimen 12 typical of delta phase.

## **Appendix A3**

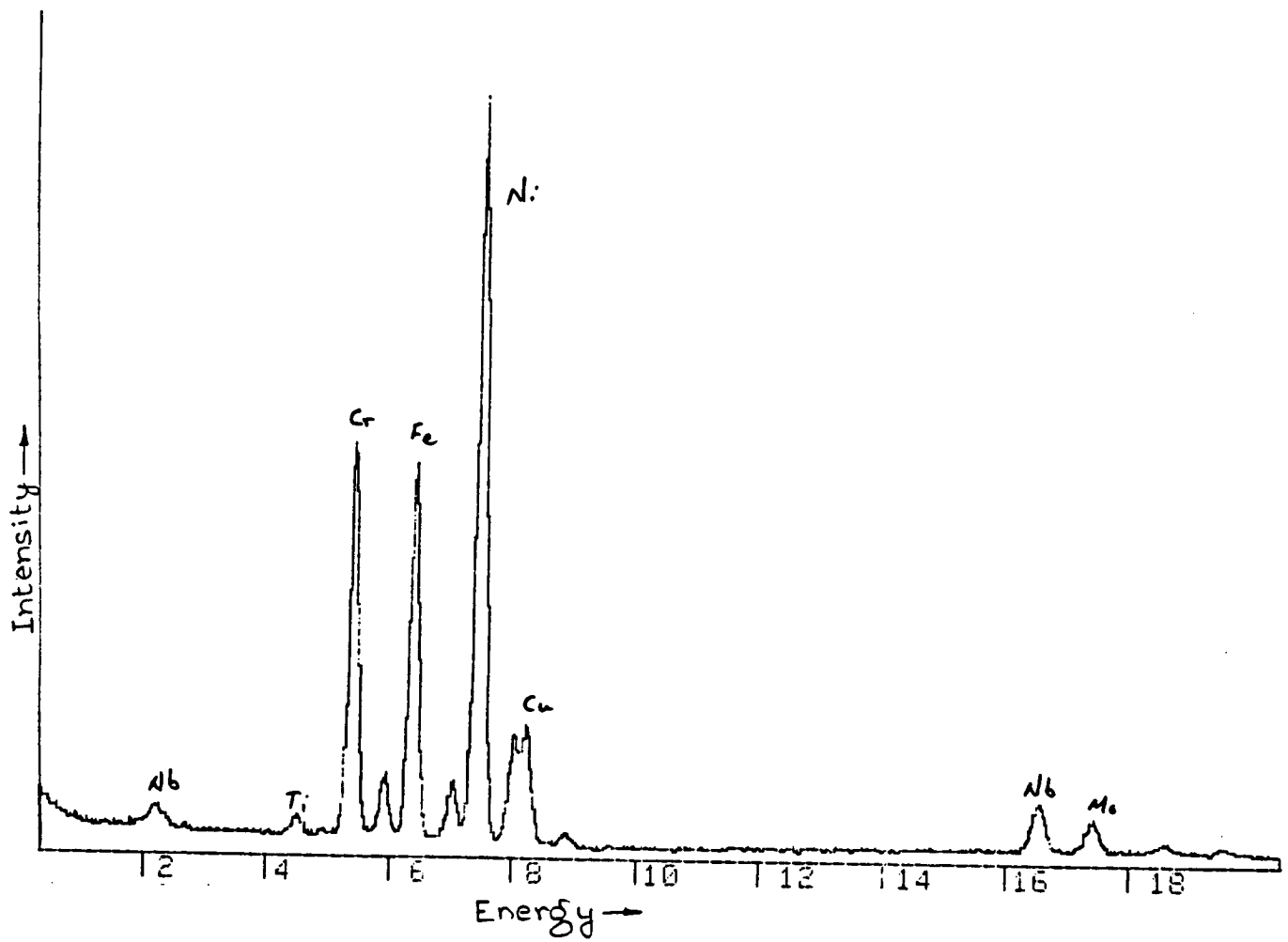
### **TEM - Energy Dispersive X-ray Analysis of Particles in Thin-Film**

- |                |  |      |
|----------------|--|------|
| - Specimen 12. | TEM micrograph and schematic EDS spectra of particles 1-16 | A3.1 |
| - Specimen 13. | Schematic of microstructure EDS spectra of particles 1-4   | A3.2 |
| - Specimen 20. | EDS Spectra of one small particle                          | A3.3 |

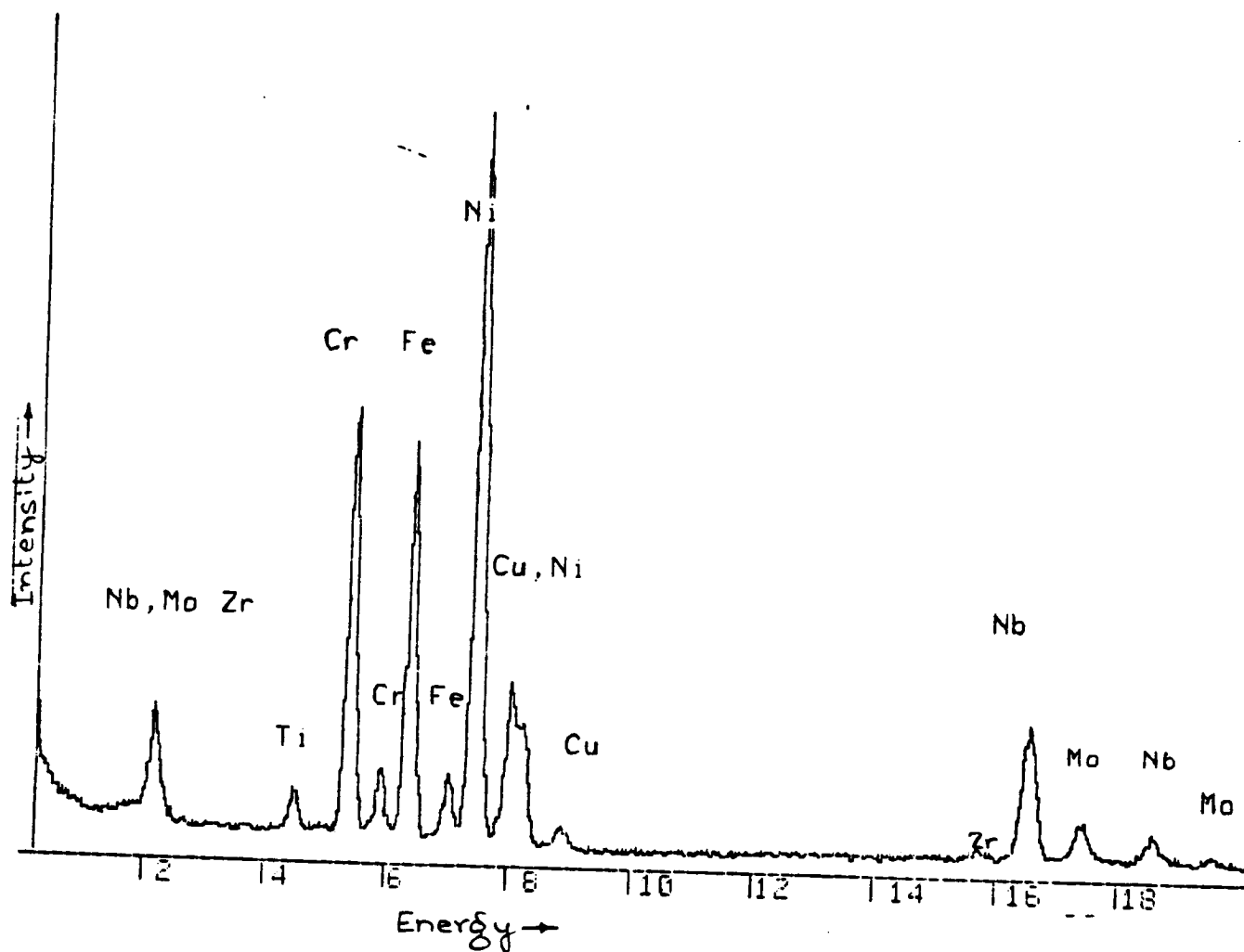


Particle A

### A3.1 Areas used for TEM-EDS Analysis of Specimen 12.

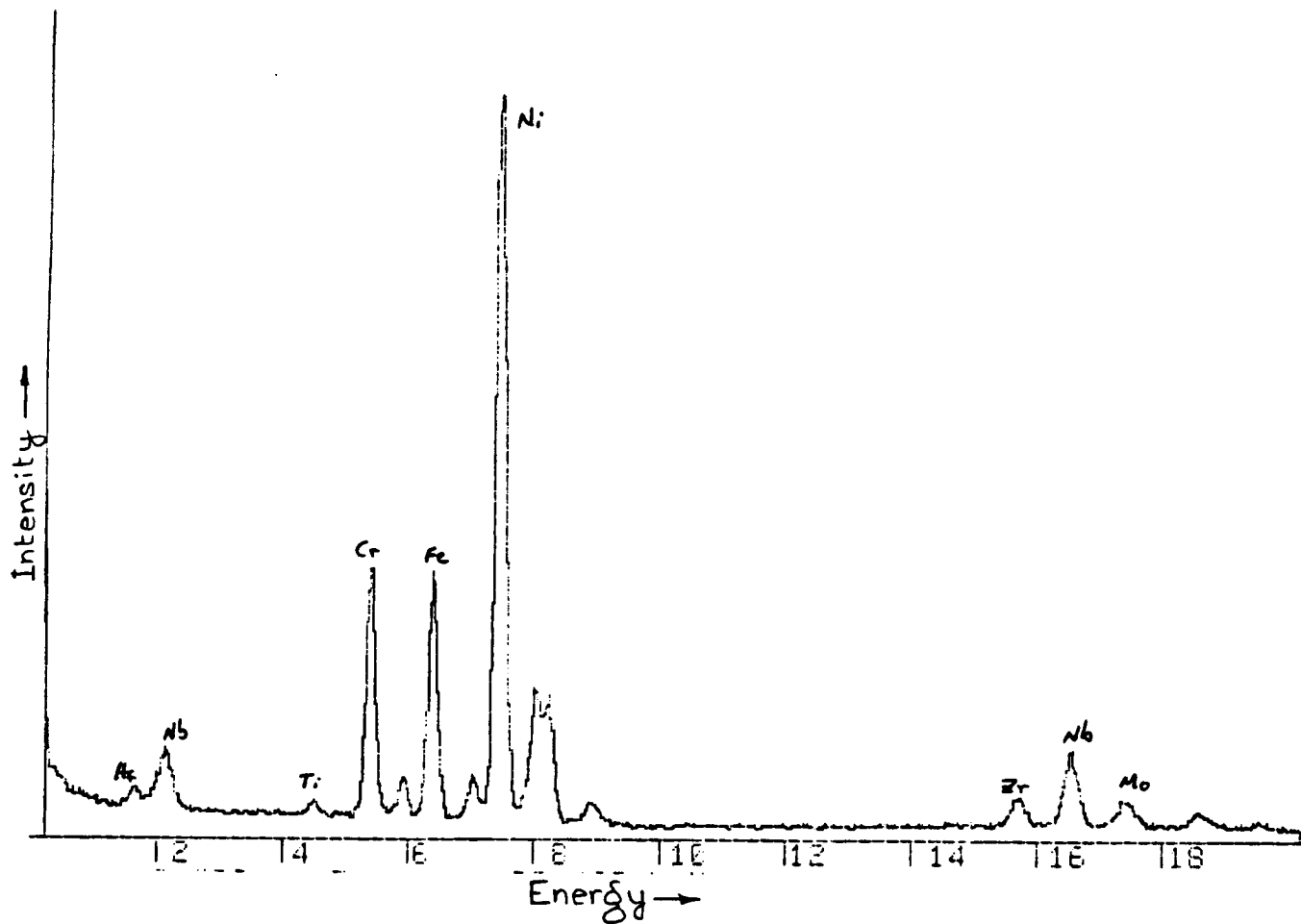


TEM-EDS spectra from area typical of matrix in Photo A, Specimen 12.

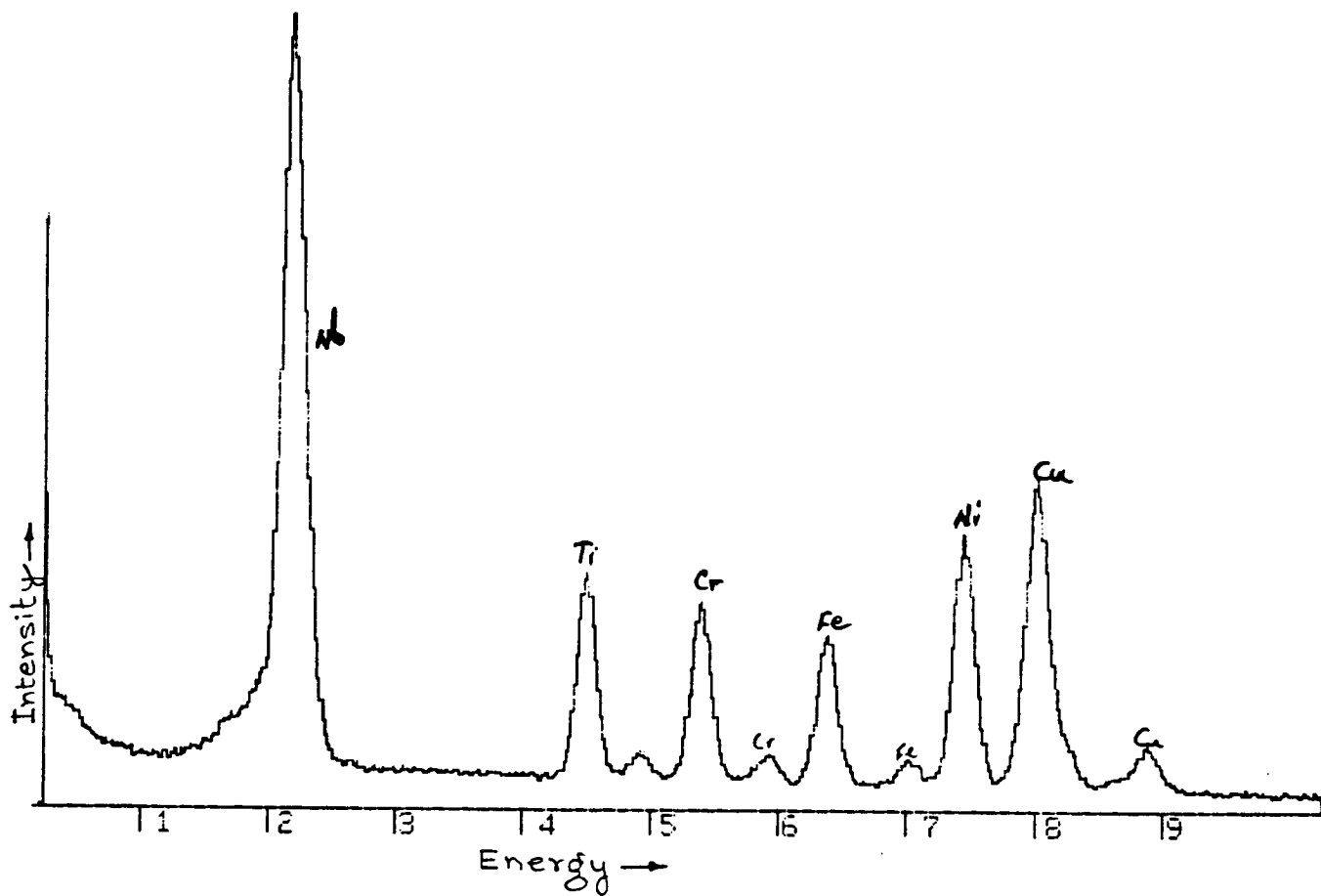


TEM-EDS spectra from area typical of particles 1, 3, 6, 8, 9, 12, and 16 in Photo A, Specimen 12.

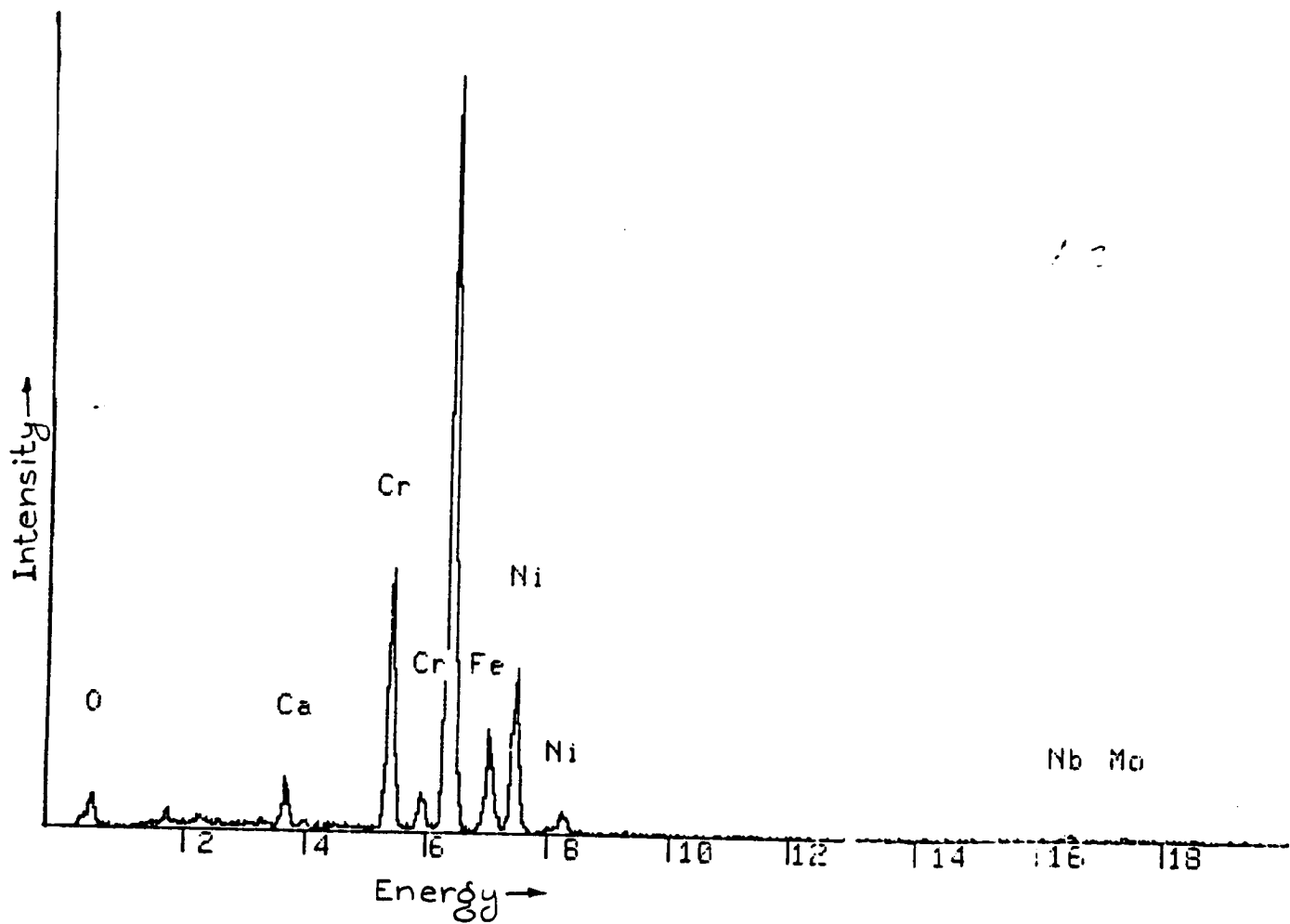




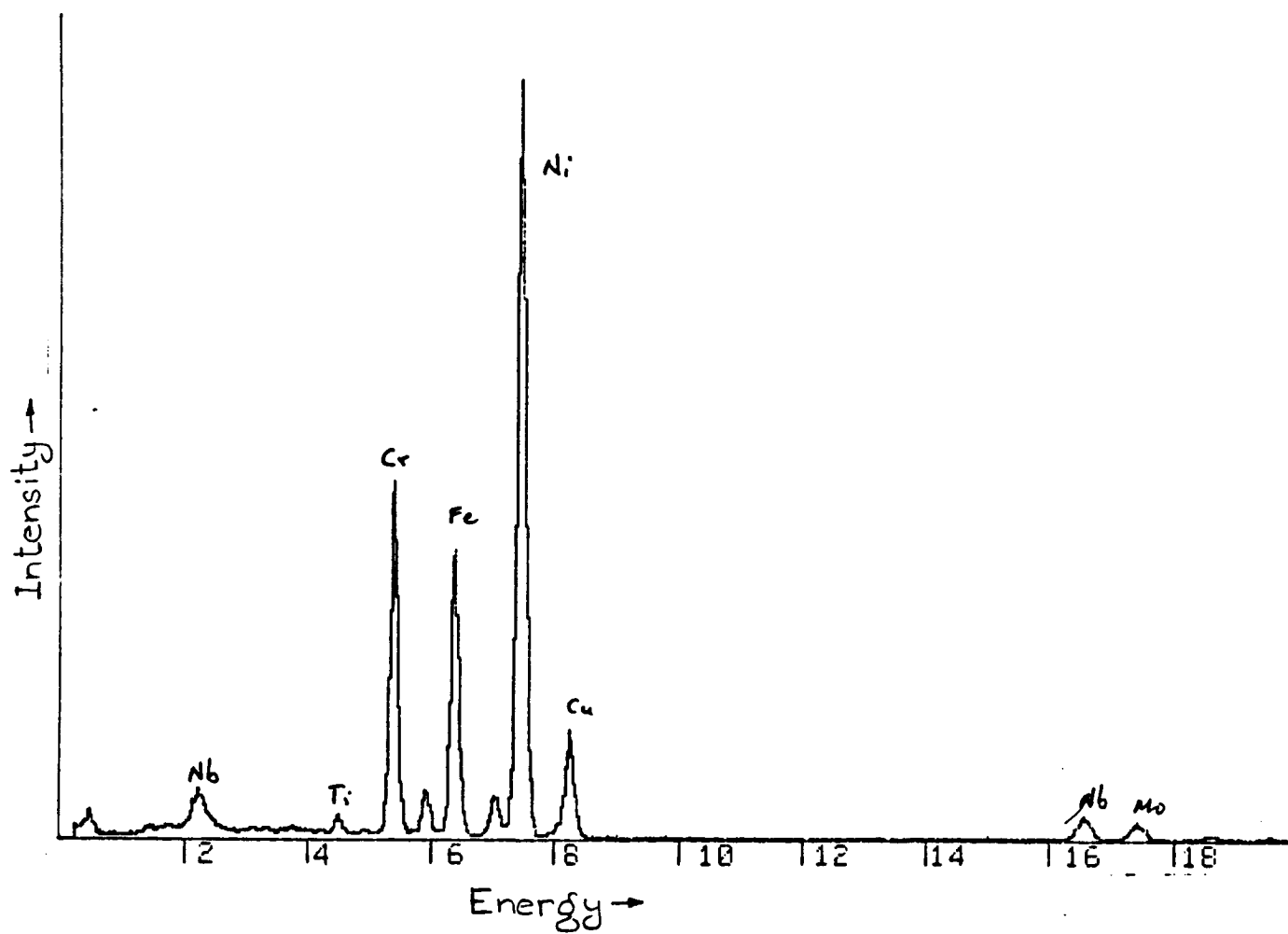
TEM-EDS spectra from area typical of particles 2, 5, 9, 10, 13, 14, and 15 in Photo A, Specimen 12.



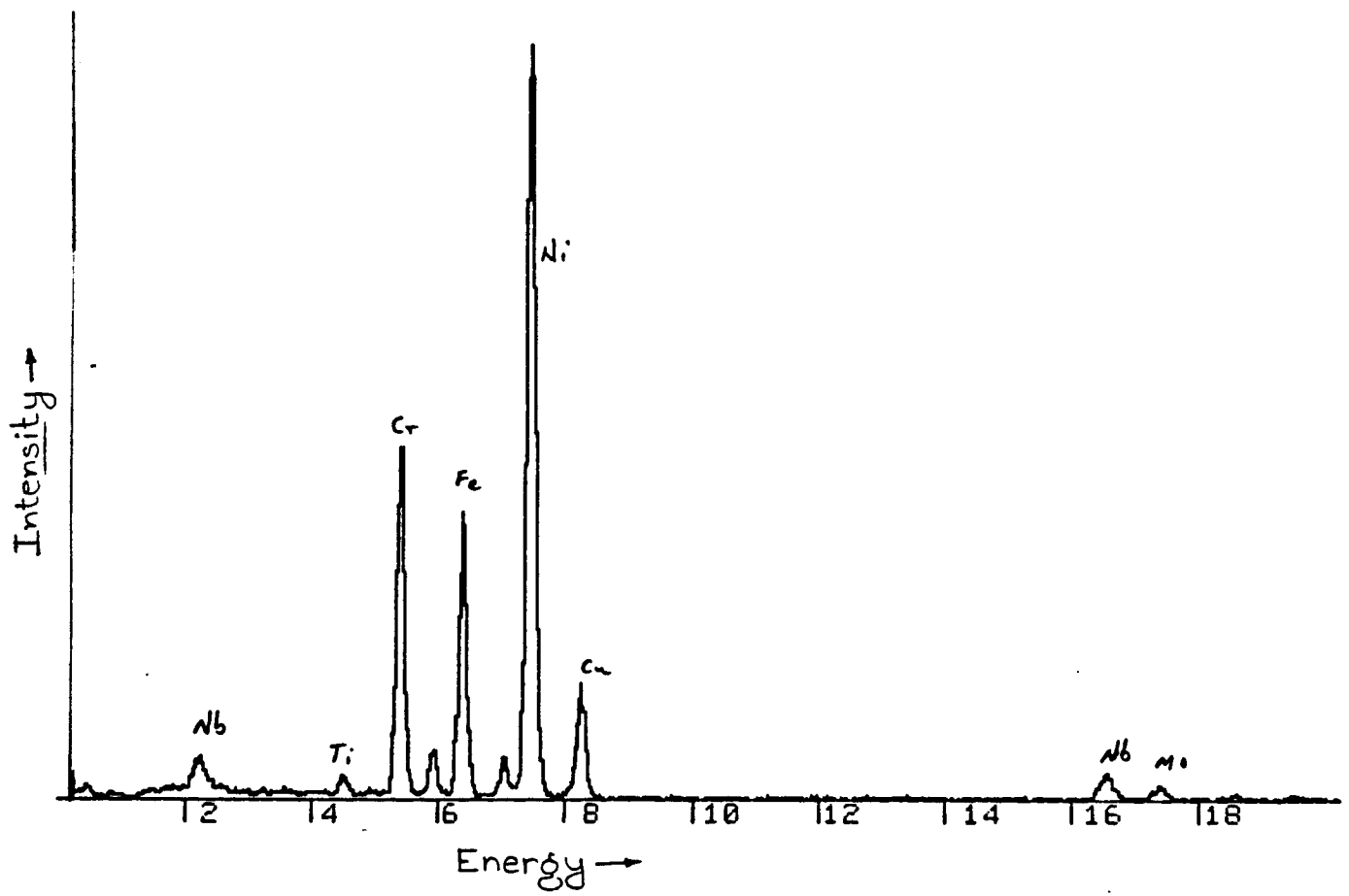
TEM-EDS spectra from particle A of Photo B, Specimen 12.



TEM-EDS typical of small particles found in Specimen 13.



TEM-EDS typical of matrix and contrast areas found in Specimen 13.



TEM-EDS typical of particles found in Specimen 20.

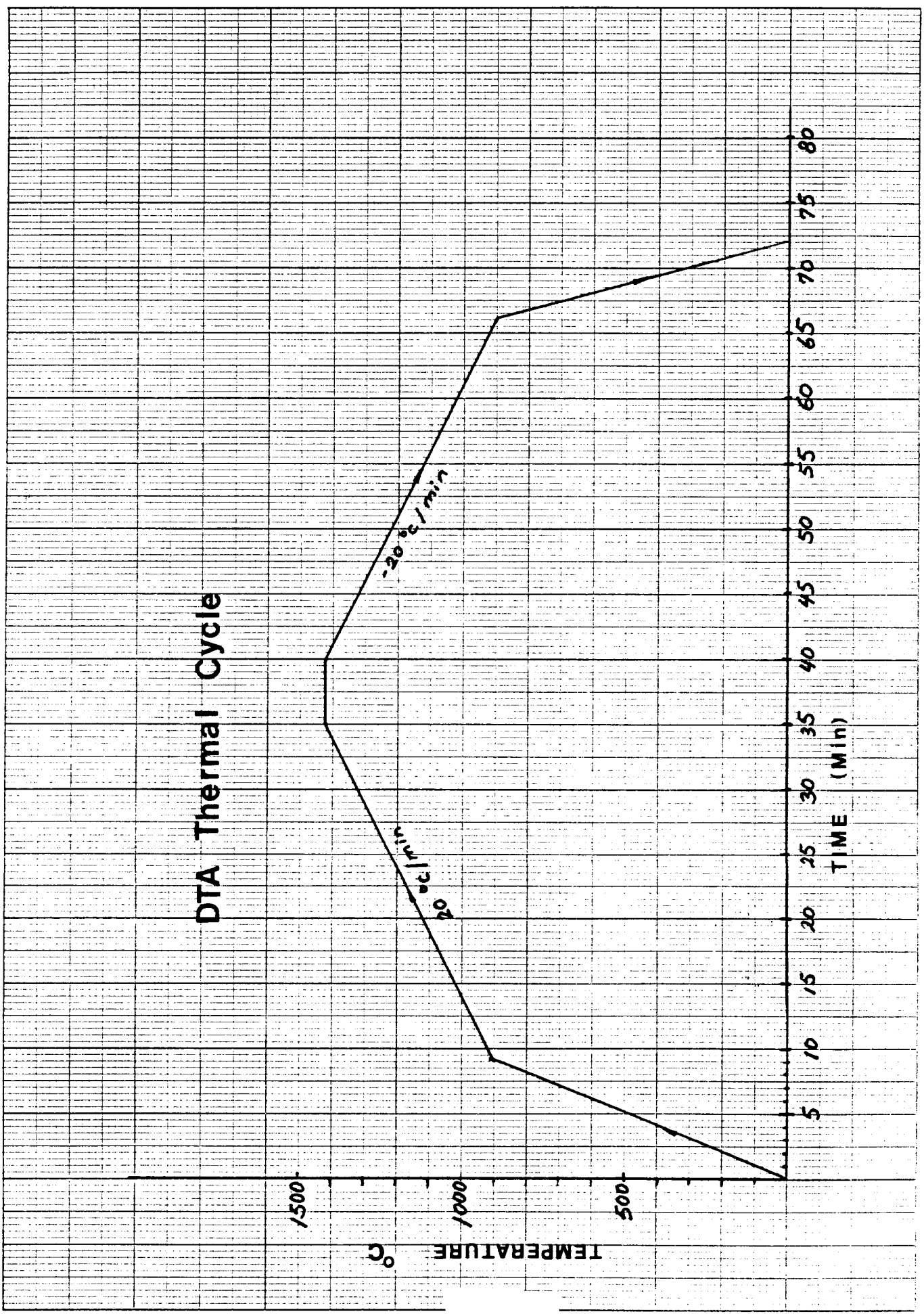
## **Appendix B**

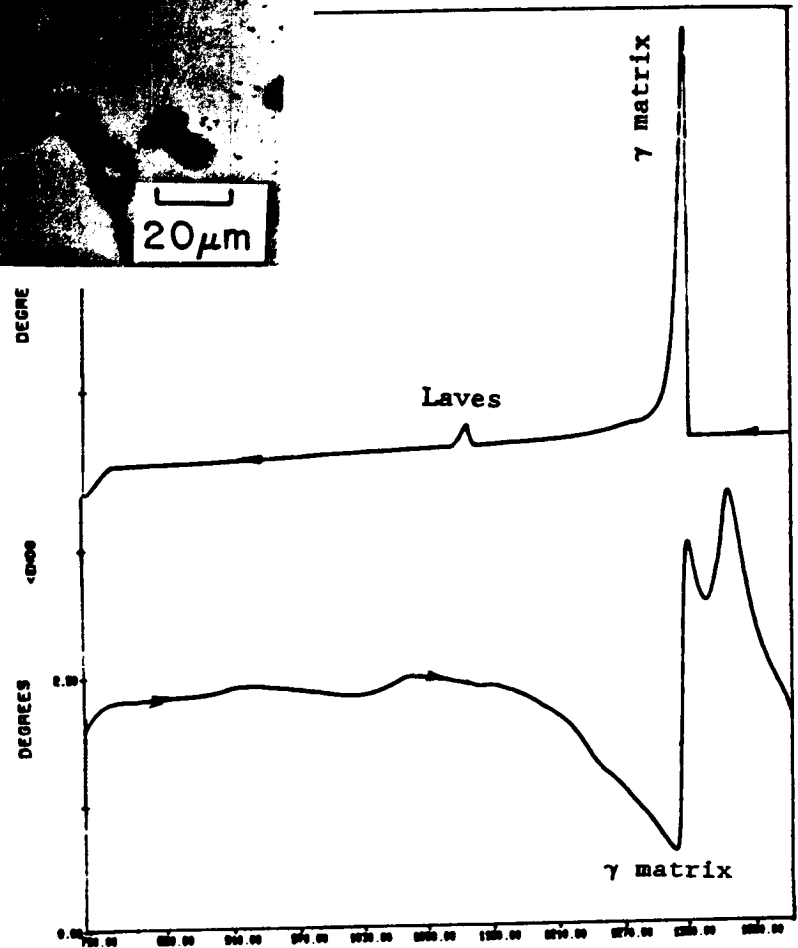
### **Differential Thermal Analysis (DTA) of Test Specimens with Micrographs of DTA - Solidified Microstructures**

<b>Appendix B1</b>	<b>DTA Curves and Micrographs</b>
B1.0	DTA Thermal Cycle
B1.1	Alloy 3 (BS)
B1.2	Alloy 5 (BSC+)
B1.3.1	Alloy 10 (SC)
B1.3.2	Alloy 27 (SC+)
B1.4	Alloy 12 (BC)
B1.5	Alloy 13 (B)
B1.6	Alloy 20 (none)
B1.7	Alloy 22 (C+)
B1.8	Alloy 25 (S+)
B1.9	Alloy 14 (P)
B1.10	Alloy 718 commercial wrought

### **Appendix B2 DTA Reproducibility; Alloy 718 Commercial Wrought**

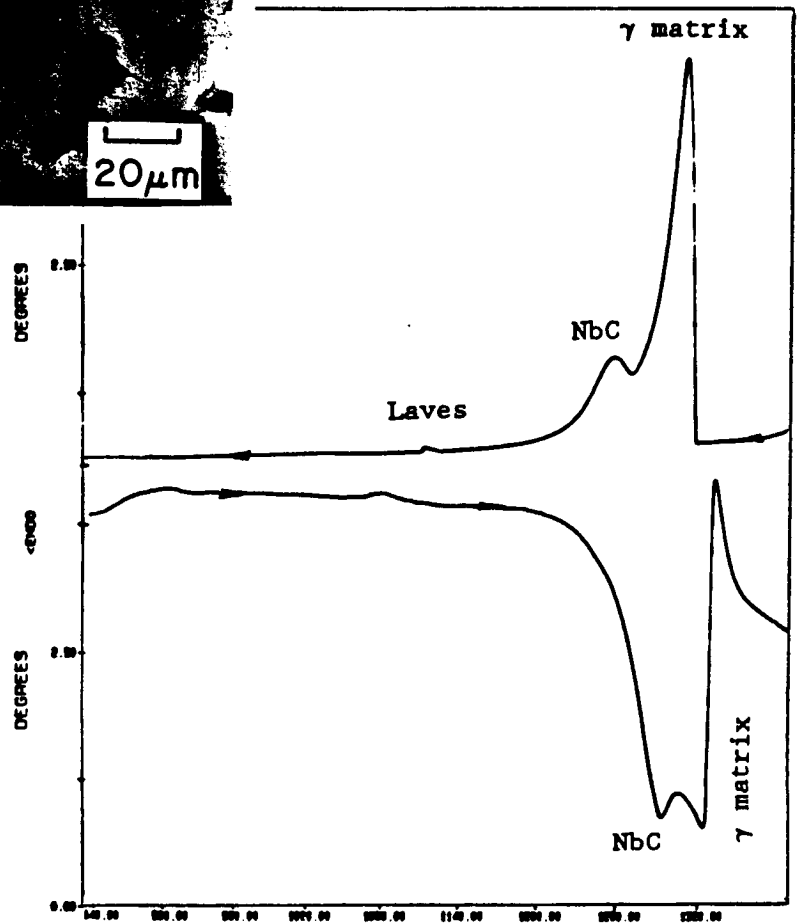
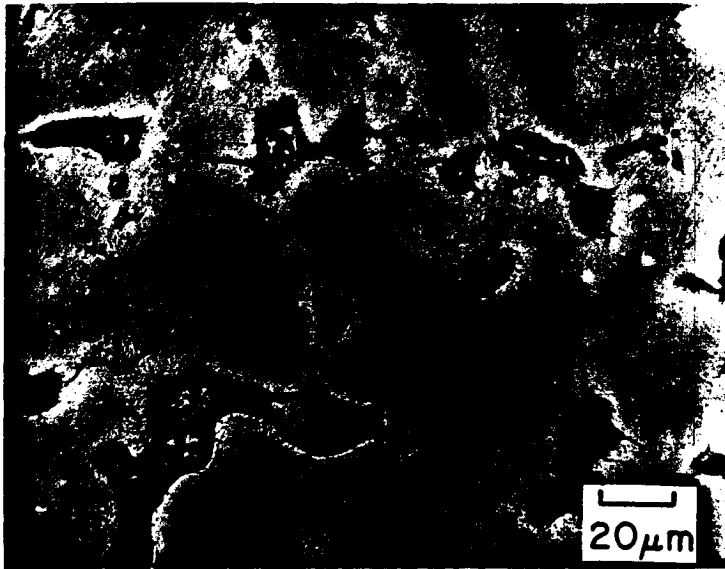
# DTA Thermal Cycle



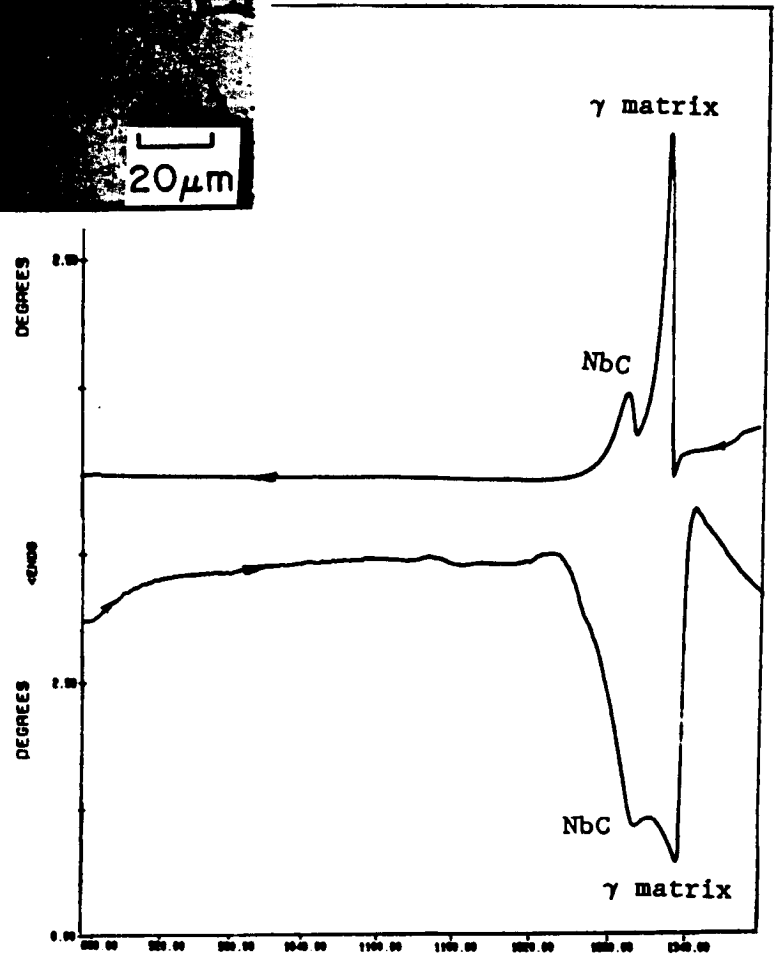
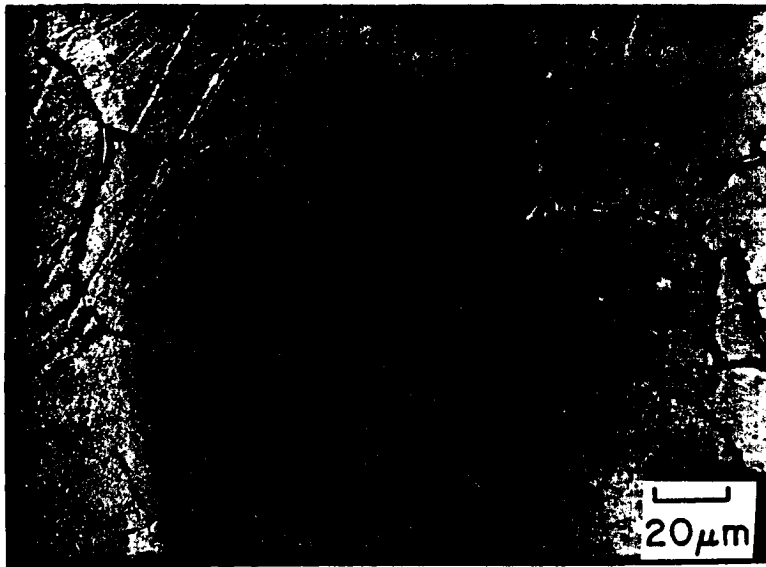


DTA of heating (melting) (see initial microstructure in Appendix A1) and cooling (solidification) of Specimen 3 (BS).





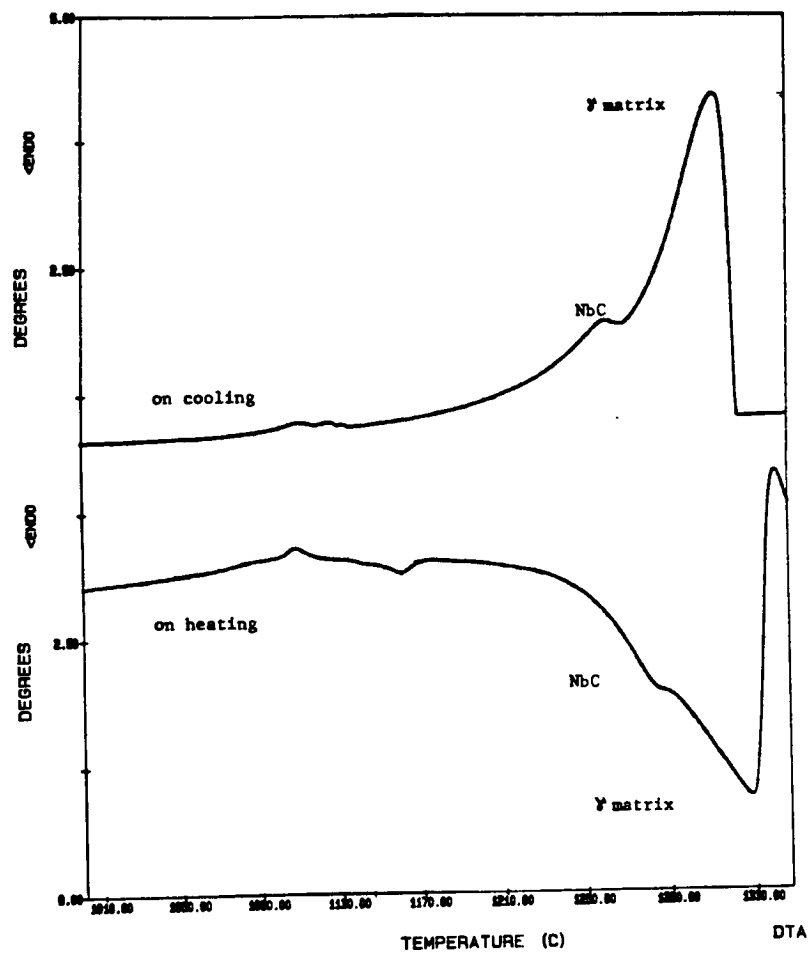
DTA of heating (melting) (see initial microstructure in Appendix A1) and cooling (solidification) of Specimen 5 (BCS).



DTA of heating (melting) (see initial microstructure in Appendix A1) and cooling (solidification) of Specimen 10 (CS).

B1.3.1

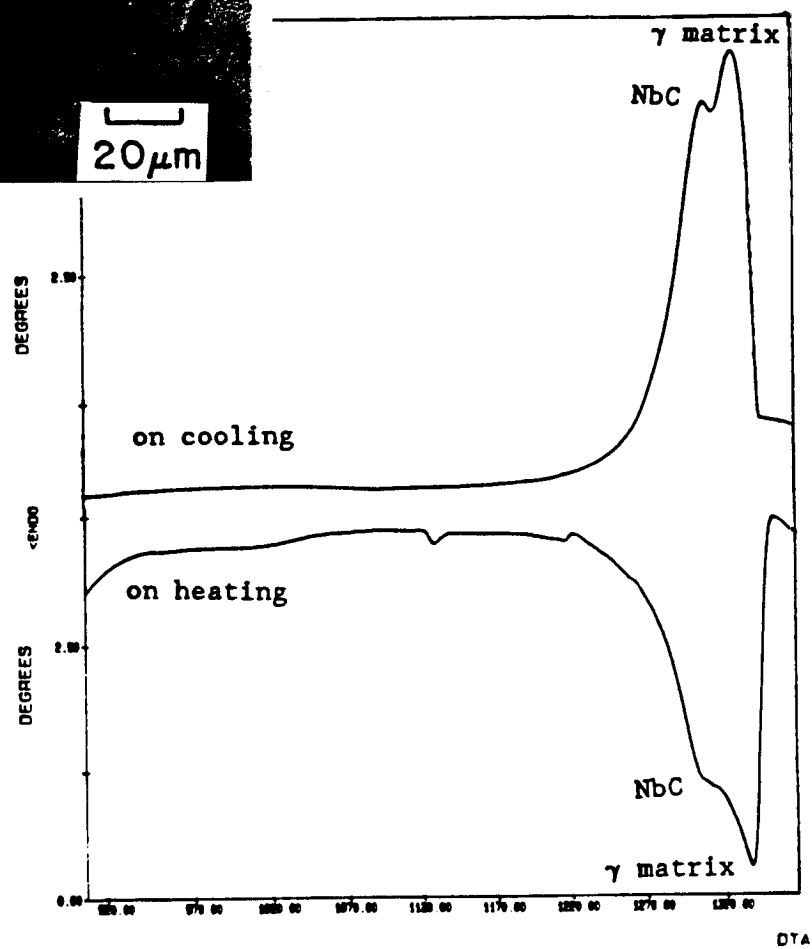
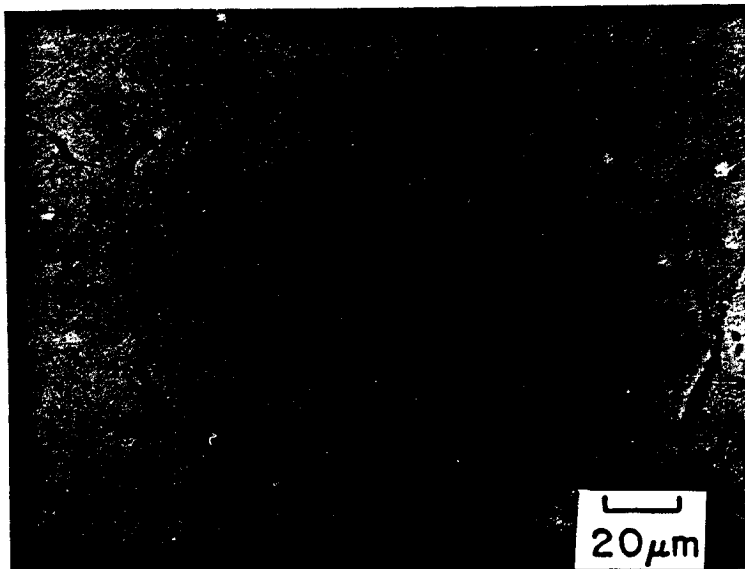
ORIGINAL PAGE IS  
OF POOR QUALITY



DTA of heating (melting) (see initial microstructure in Appendix A1) and cooling (solidification) of Specimen 27 (CS+).

B1.3.2

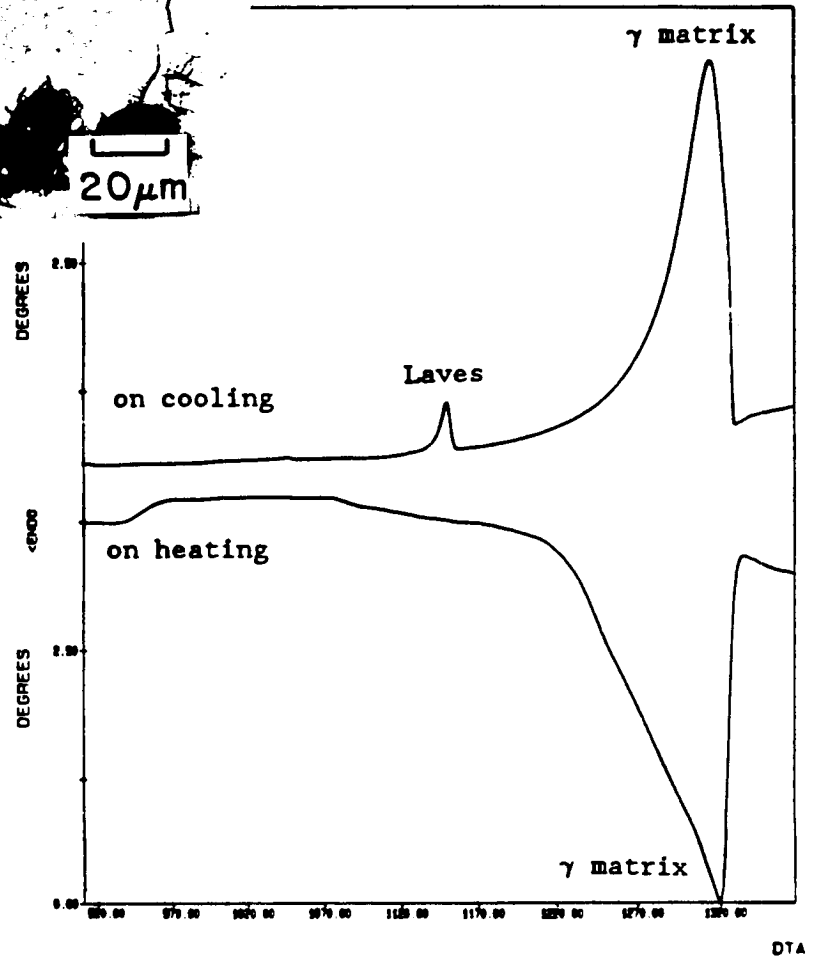
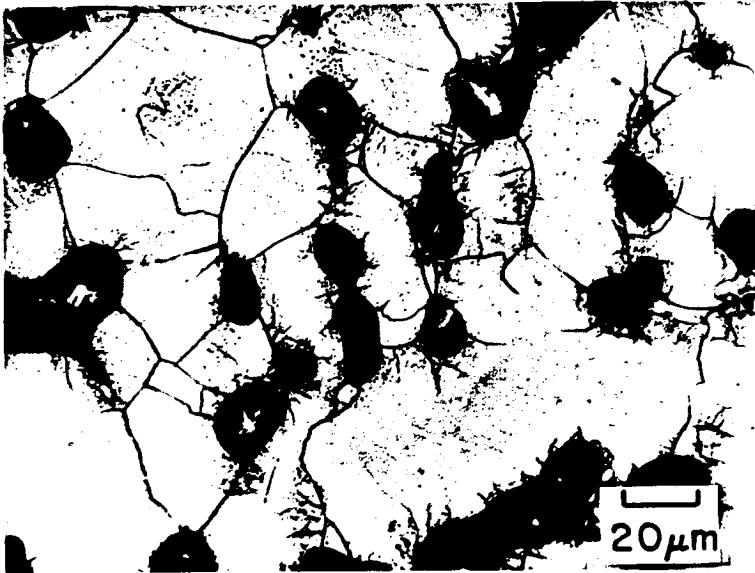
ORIGINAL PAGE IS  
OF POOR QUALITY



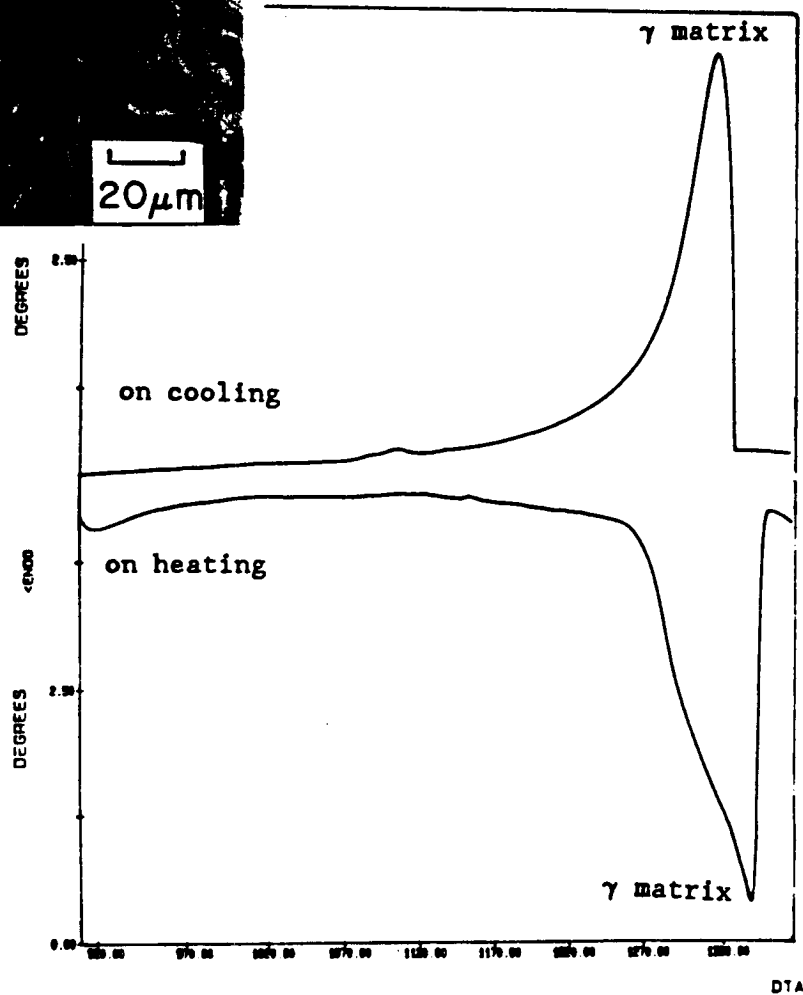
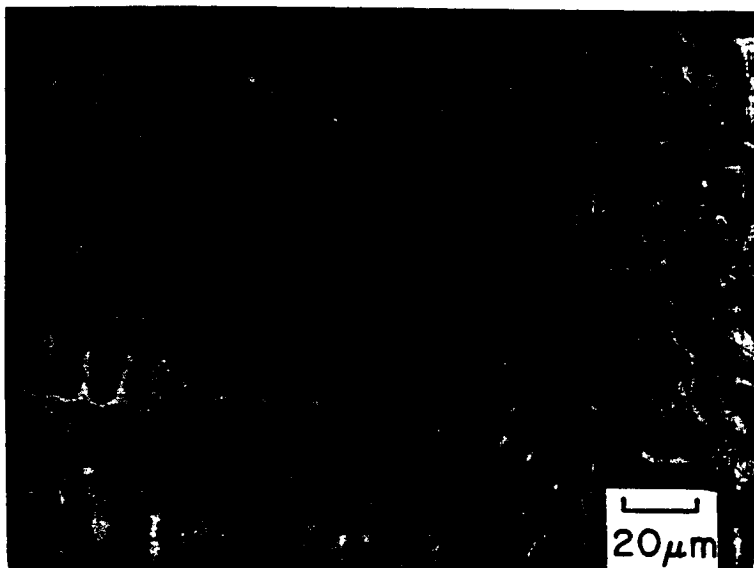
DTA of heating (melting) (see initial microstructure in Appendix A1) and cooling (solidification) of Specimen 12 (BC).

B1.4

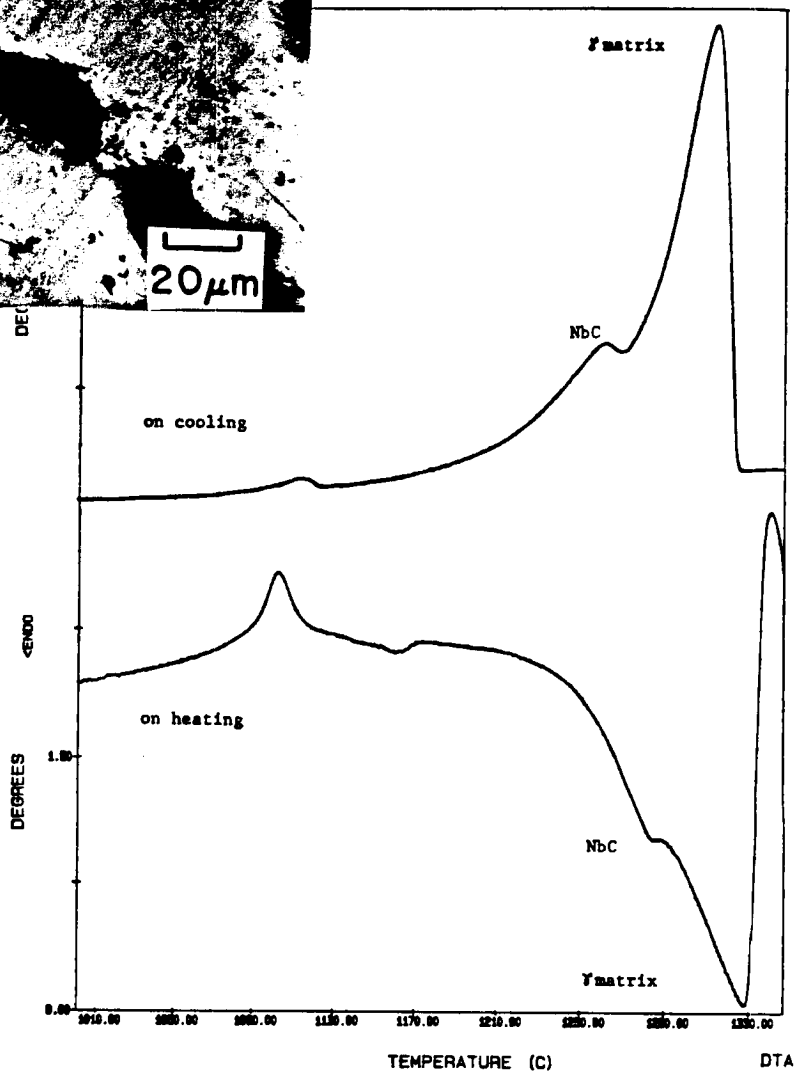
ORIGINAL PAGE IS  
OF POOR QUALITY



DTA of heating (melting) (see initial microstructure in Appendix A1) and cooling (solidification) of Specimen 13 (B).



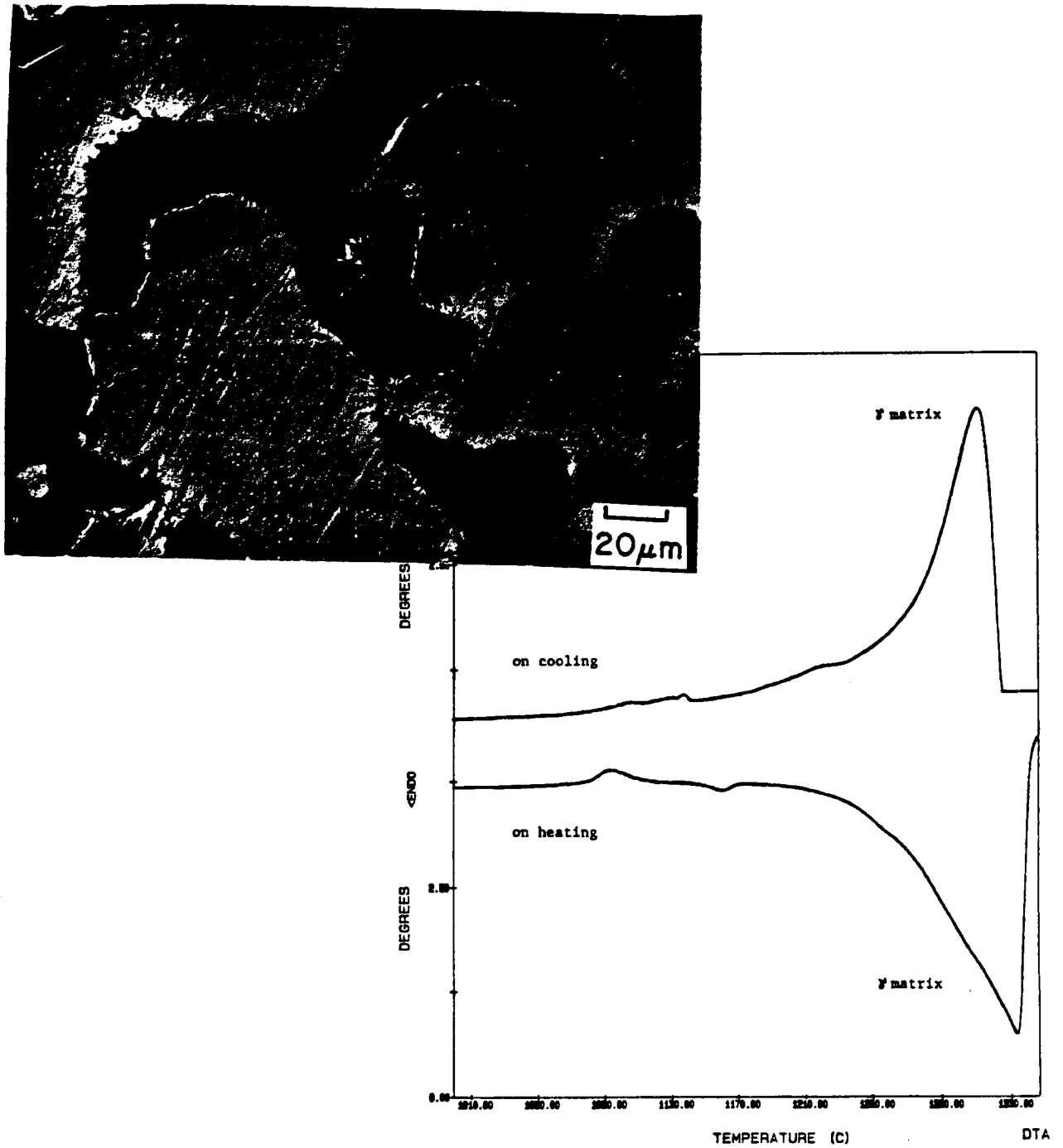
DTA of heating (melting) (see initial microstructure in Appendix A1) and cooling (solidification) of Specimen 20 (interstitial free).



DTA of heating (melting) (see initial microstructure in Appendix A1) and cooling (solidification) of Specimen 22 (C+).

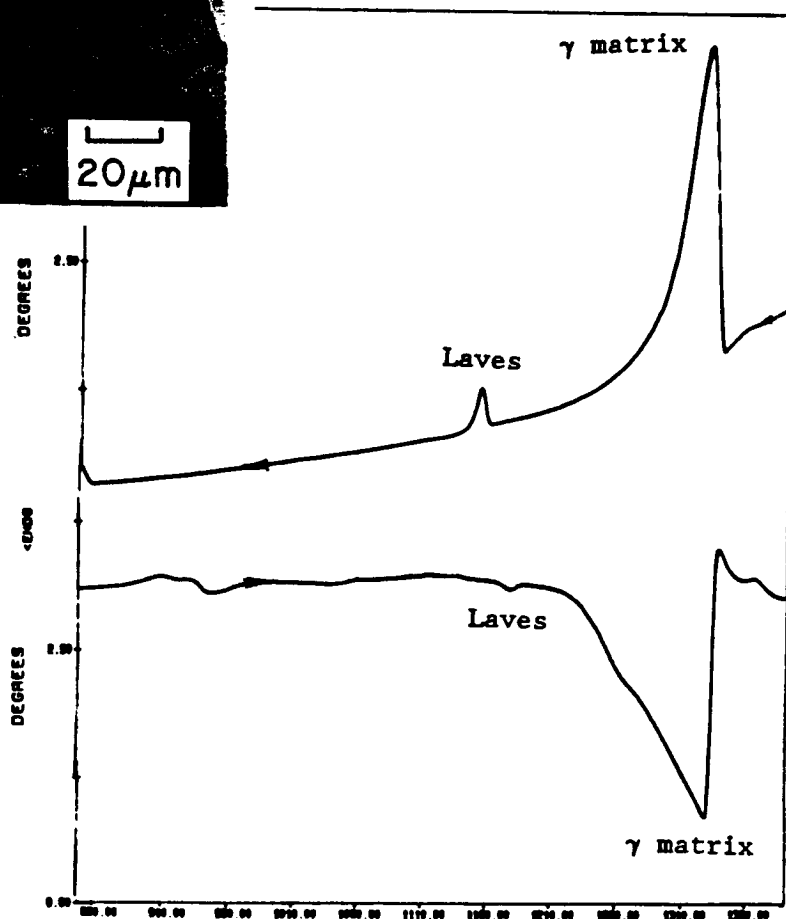
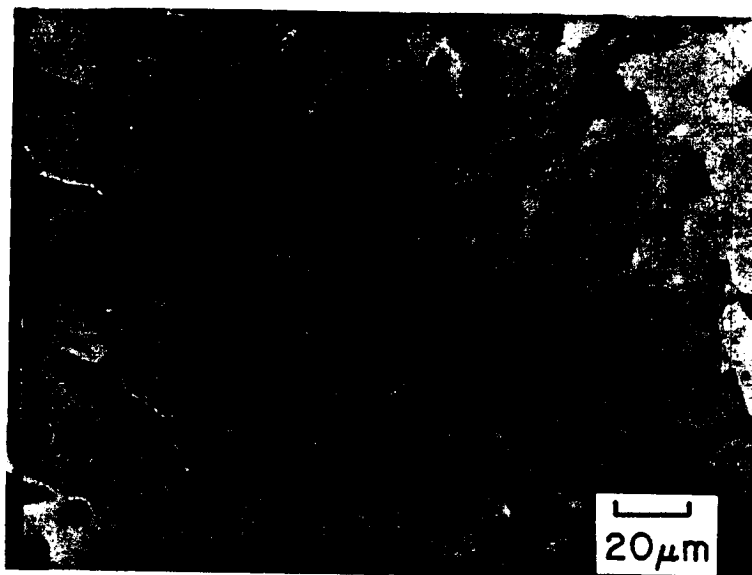
B1.7

ORIGINAL PAGE IS  
OF POOR QUALITY



DTA of heating (melting) (see initial microstructure in Appendix A1) and cooling (solidification) of Specimen 25 (S+).

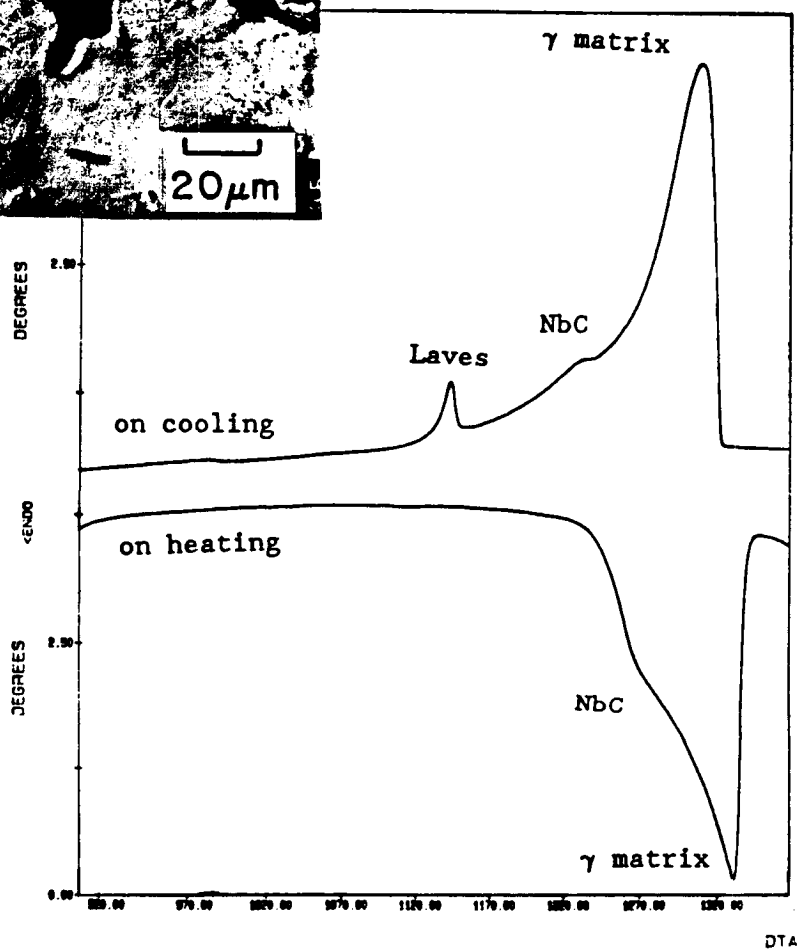




DTA of heating (melting) (see initial microstructure in Appendix A1) and cooling (solidification) of Specimen 14 (P).

B1.9

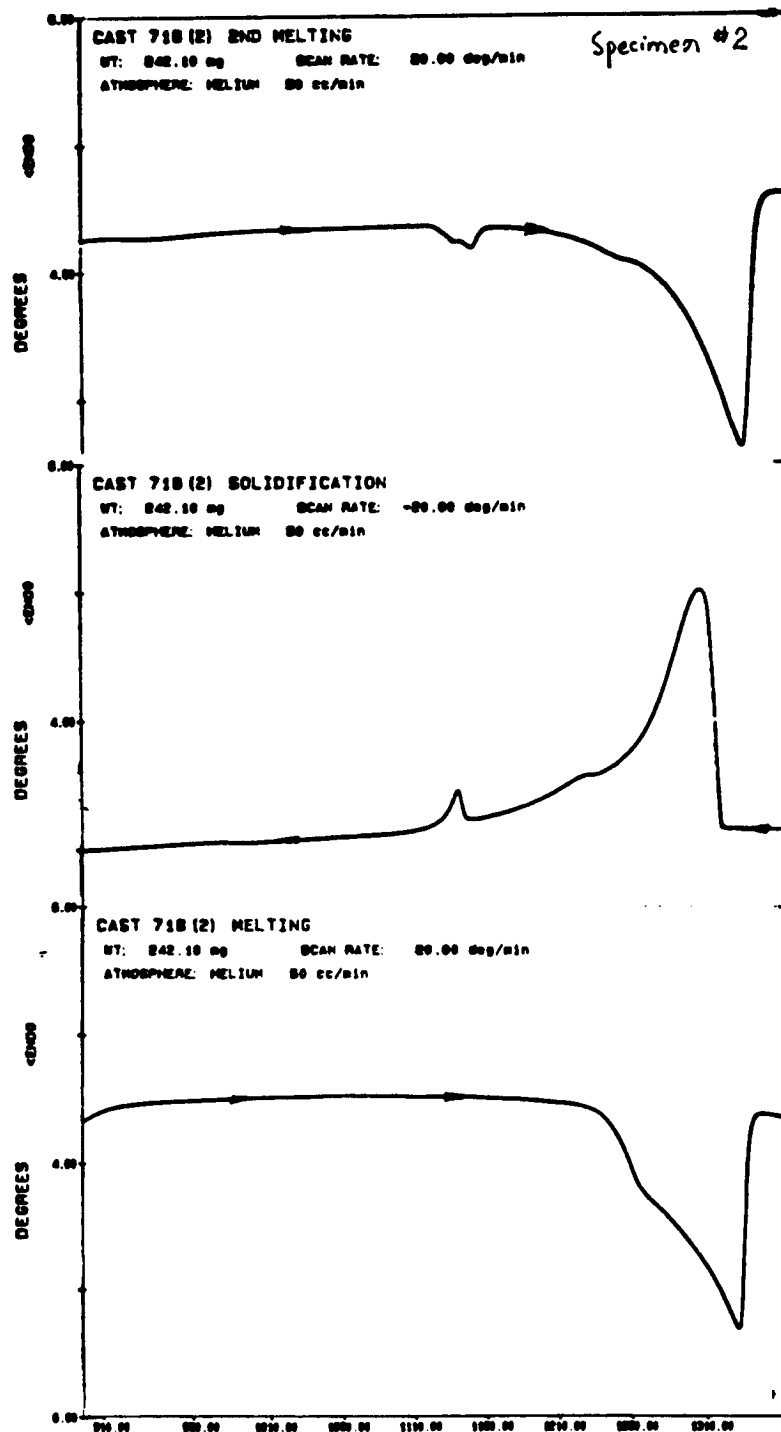
ORIGINAL PAGE IS  
OF POOR QUALITY



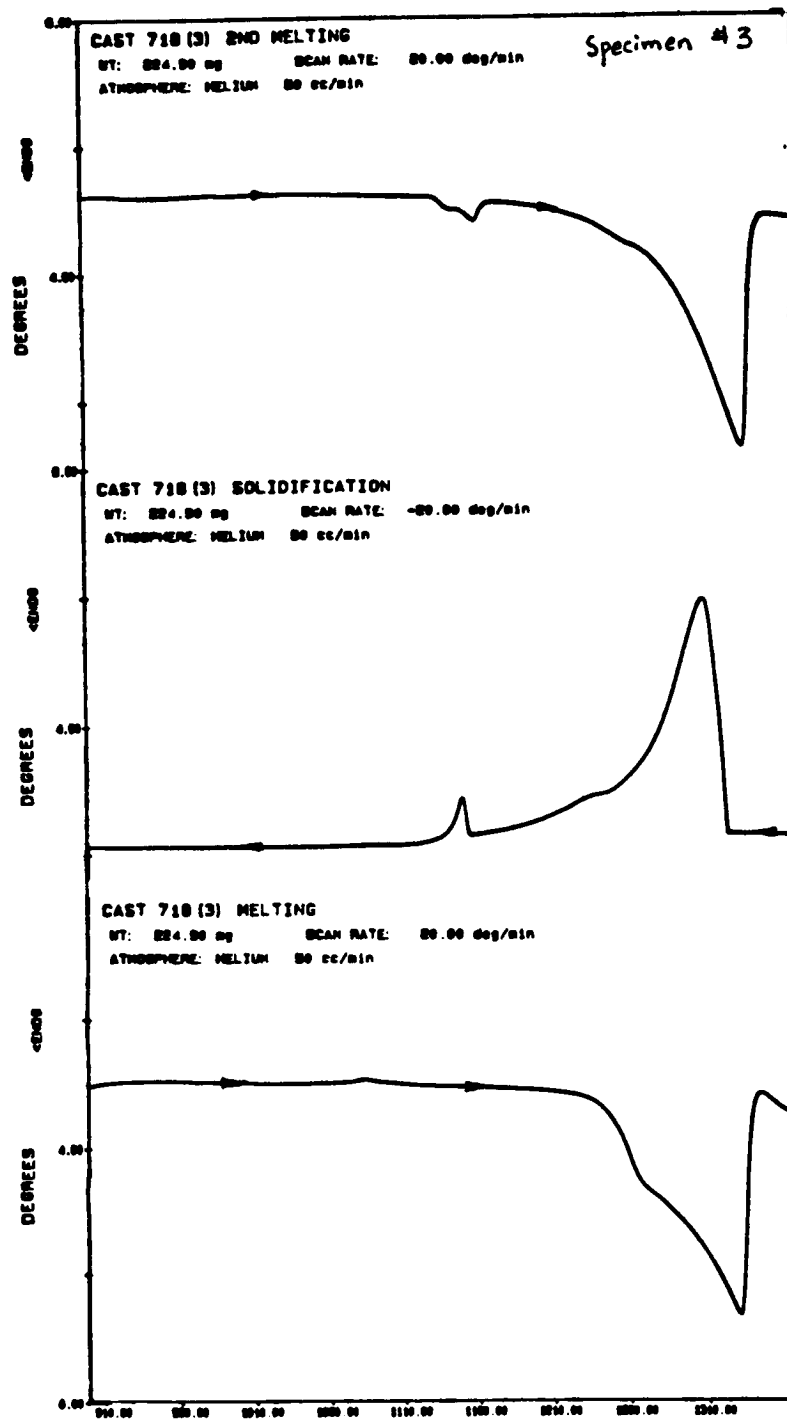
DTA of heating (melting) (see initial microstructure in Appendix A1) and cooling (solidification) of Specimen 718.



B2 Reproducibility of DTA test data is excellent ( $\pm 5^\circ\text{C}$ ) as shown in 3 runs of commercial alloy 718.



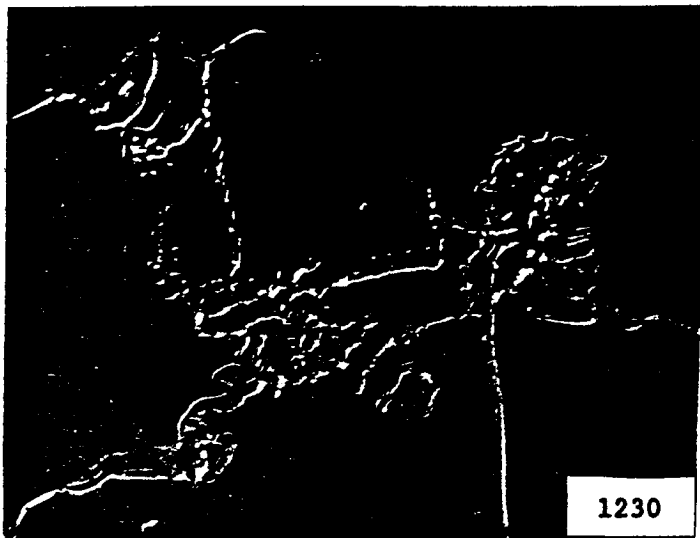
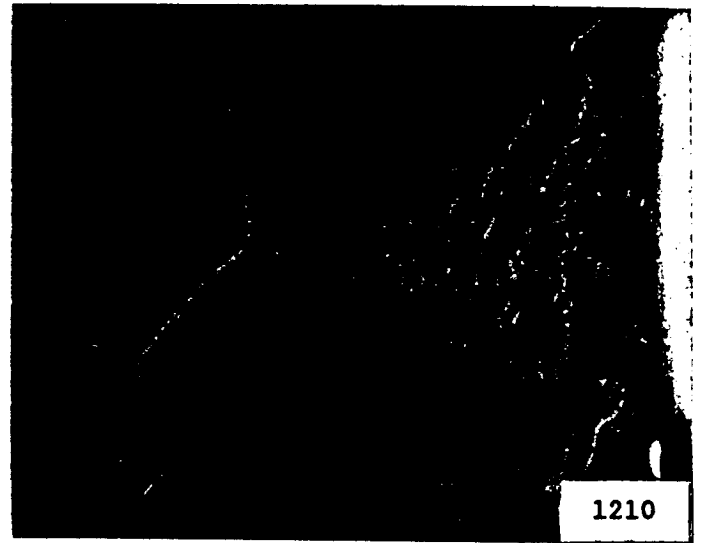
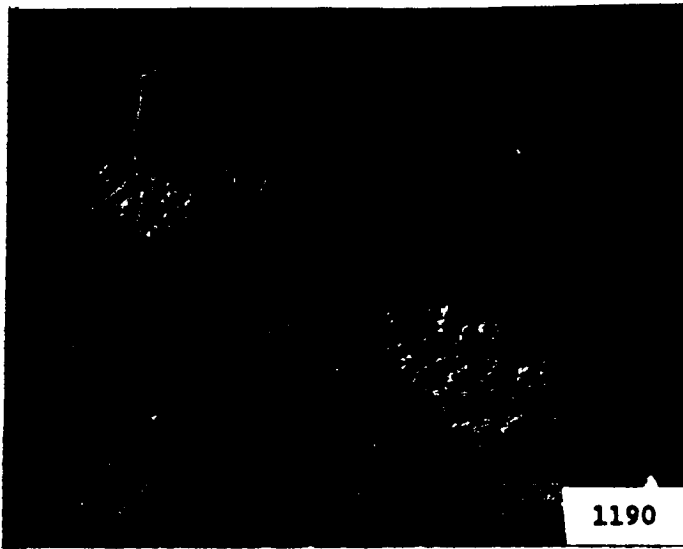
Commercial 718 alloy run number 2.



Commercial 718 alloy run number 3.

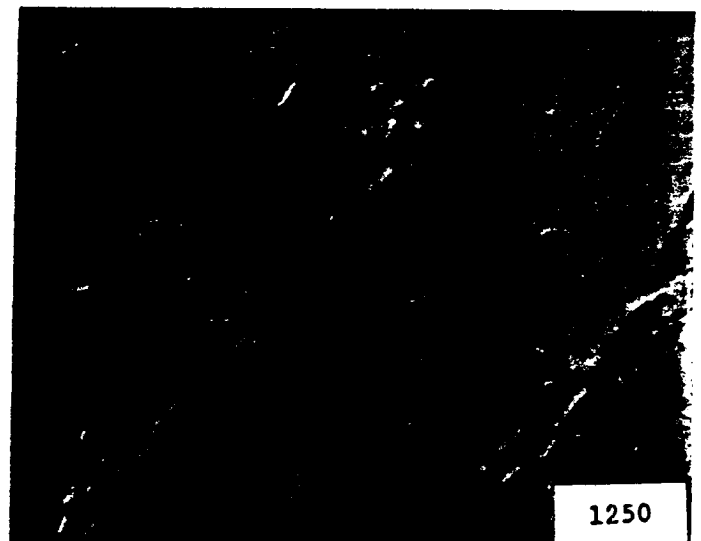
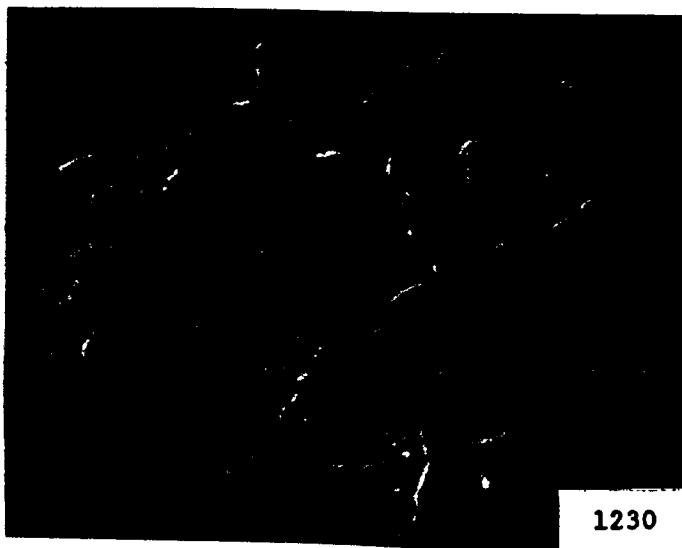
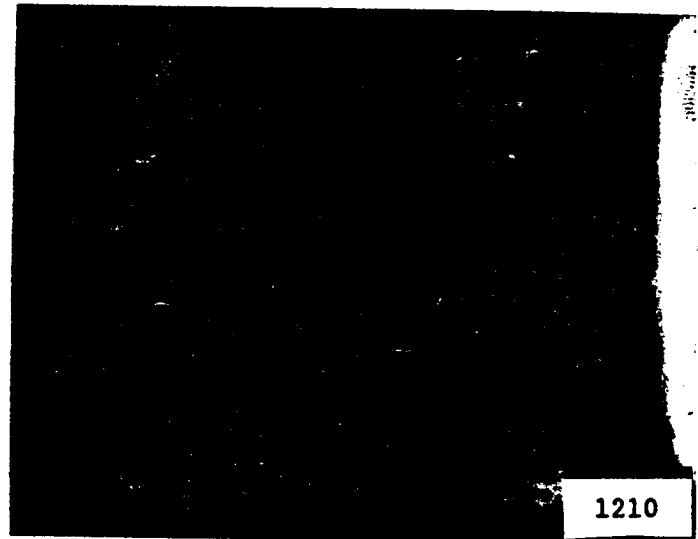
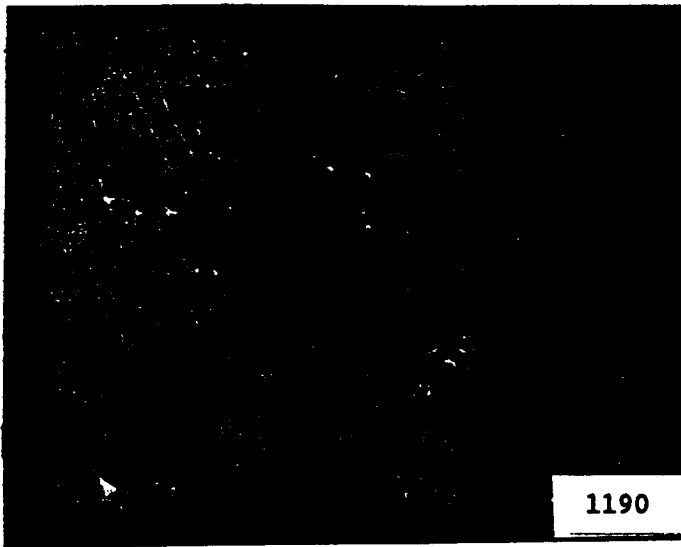
## **Appendix C**

### **Microstructures from Gleeble Weld Simulation**



Alloy 3: S. B. (P)

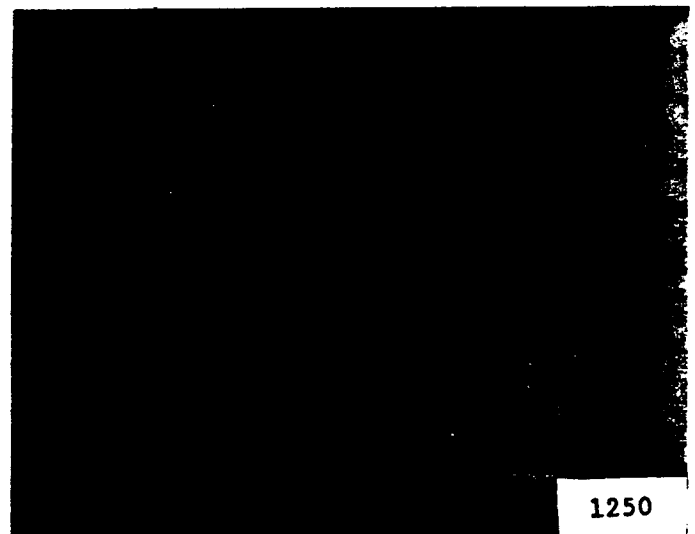
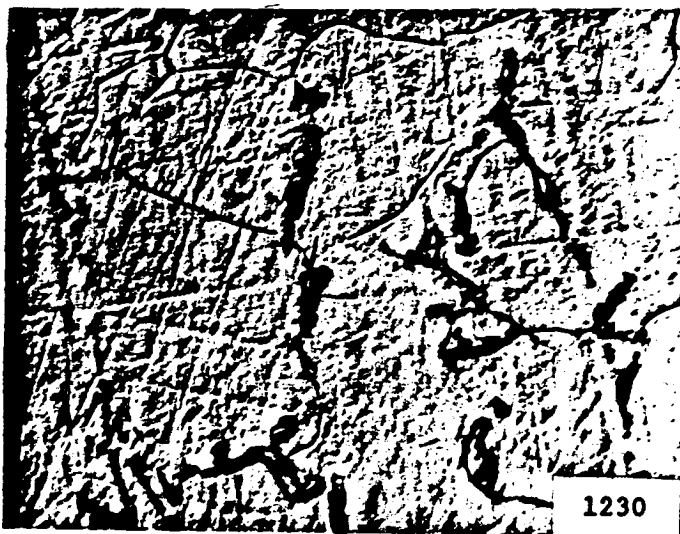
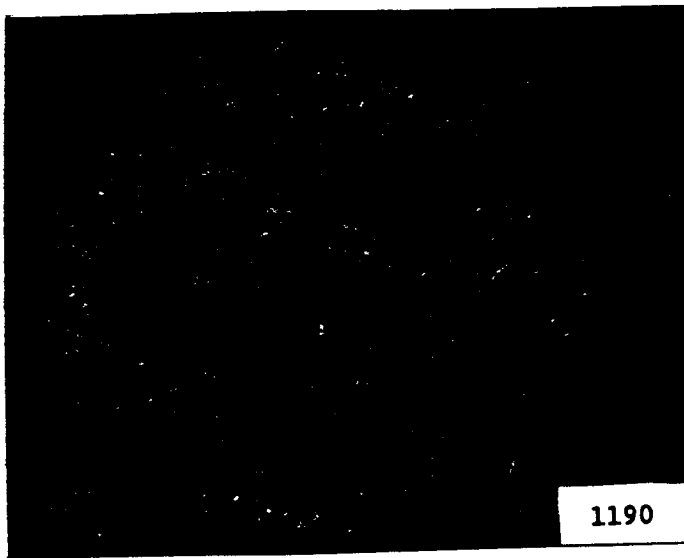
Microstructures after quenching from 1190C, 1210C, 1230C, and 1250C using the Gleeble cycle of Figure 1.



Alloy 5: C. S. B. (+)

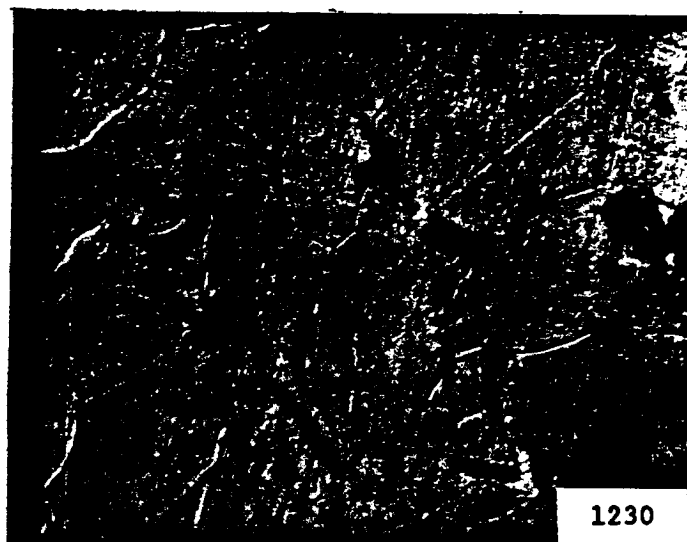
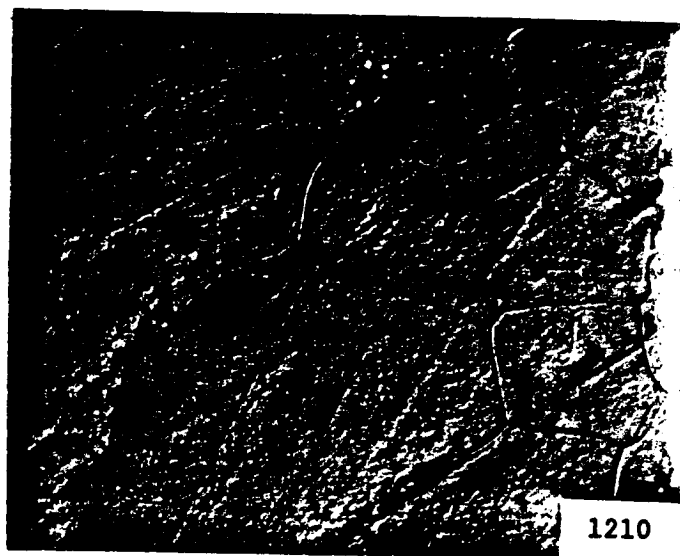
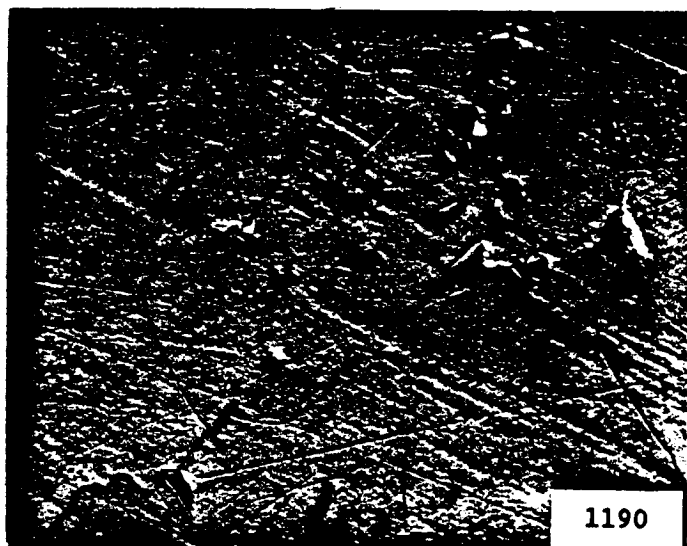
Microstructures after quenching from 1190C, 1210C, 1230C, and 1250C using the Gleeble cycle of Figure 1.





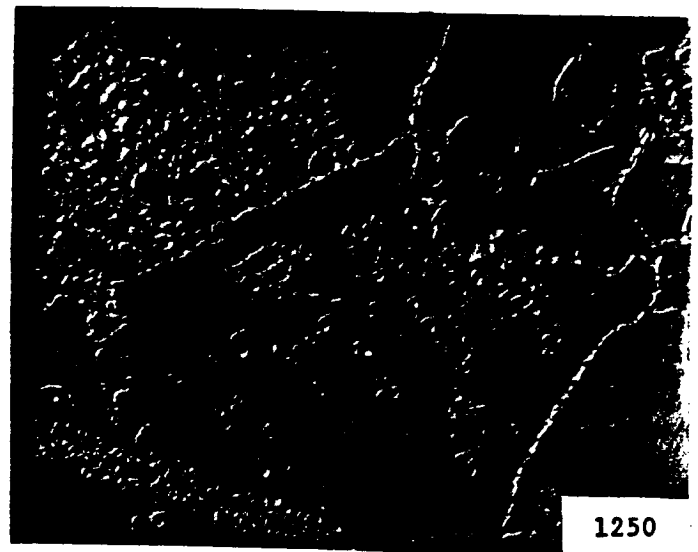
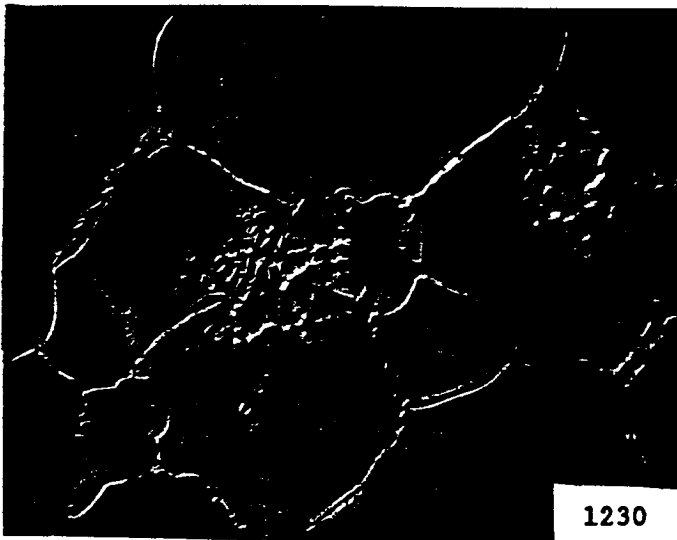
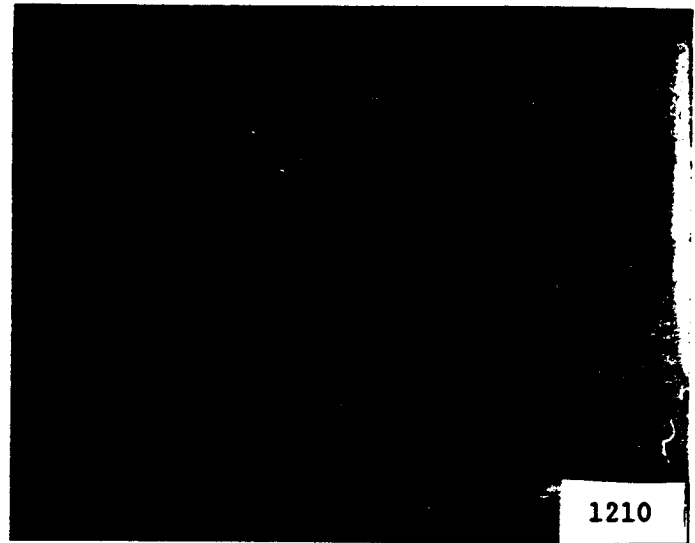
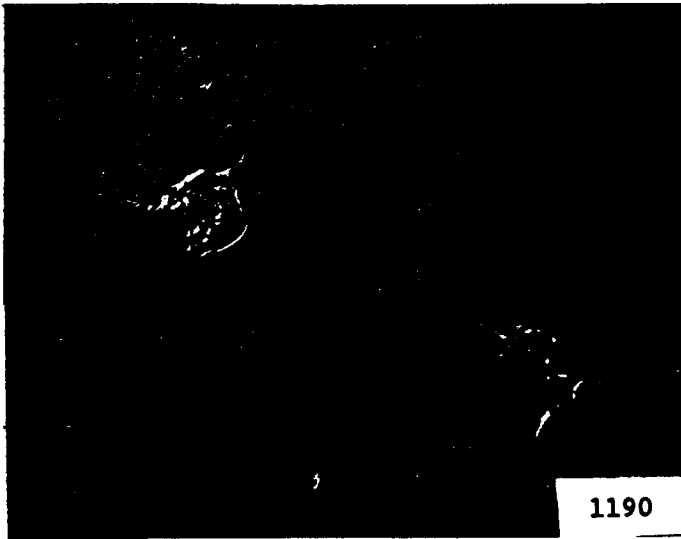
Alloy 10: S. C

Microstructures after quenching from 1190C, 1210C, 1230C, and 1250C using the Gleeble cycle of Figure 1.



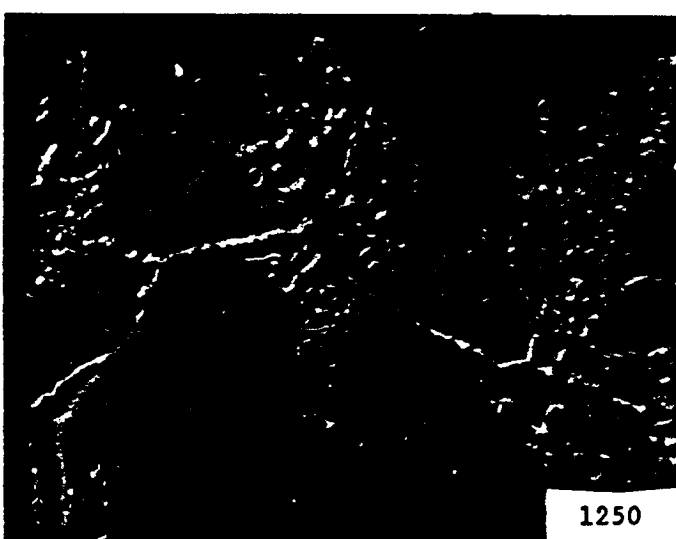
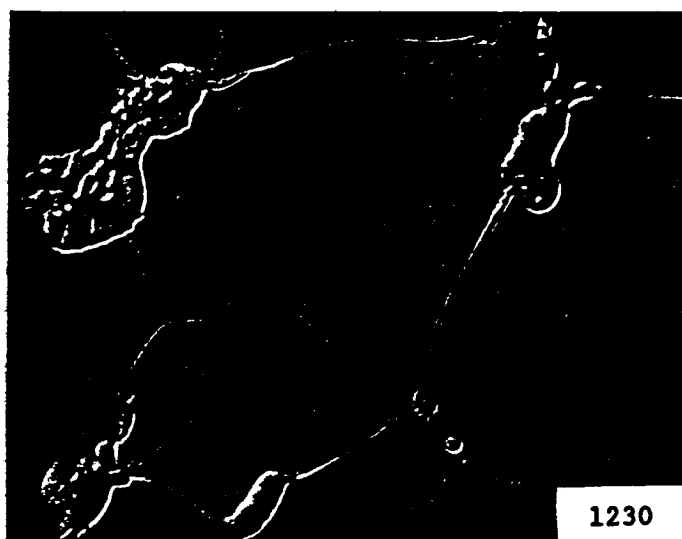
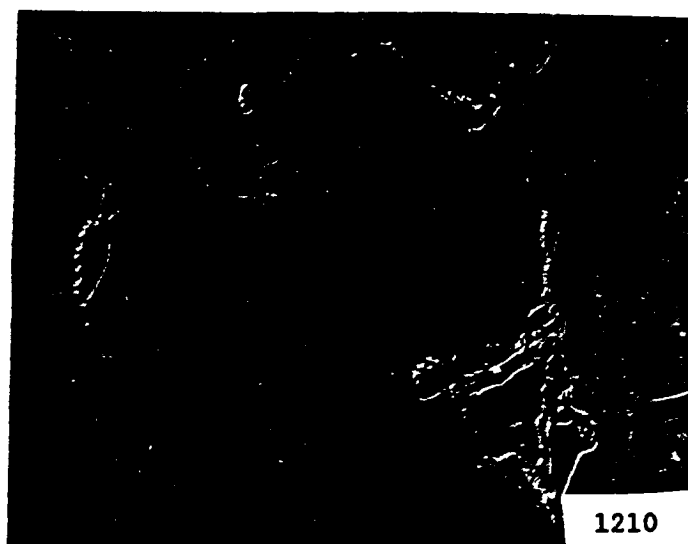
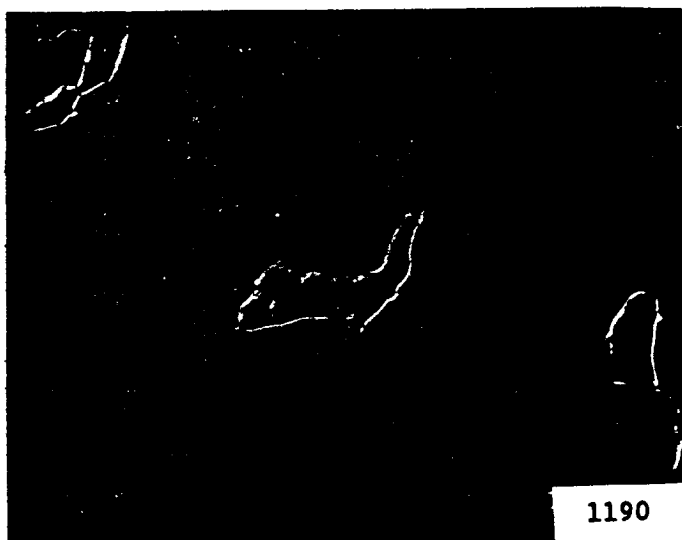
Alloy 12: B. C

Microstructures after quenching from 1190C, 1210C, 1230C, and 1250C using the Gleeble cycle of Figure 1.



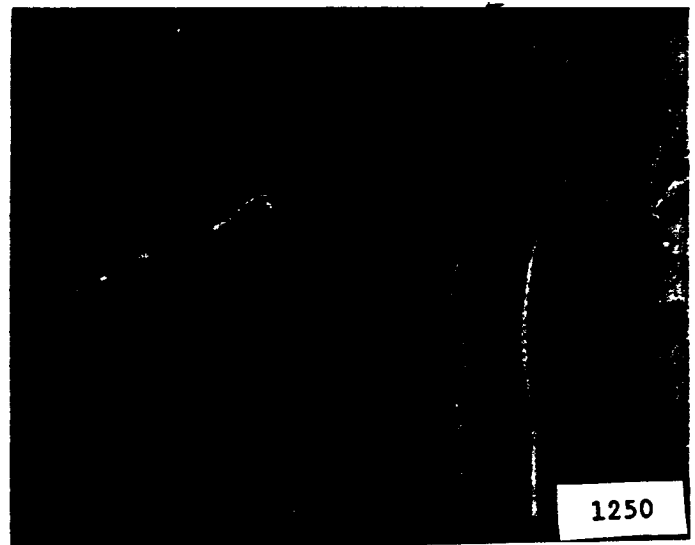
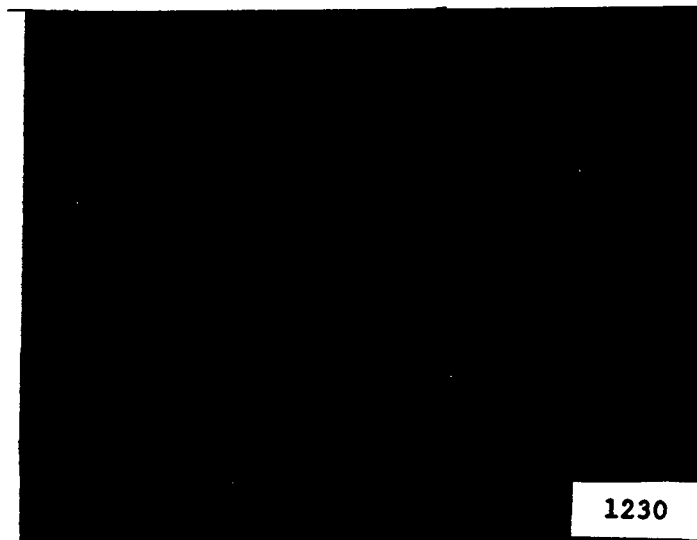
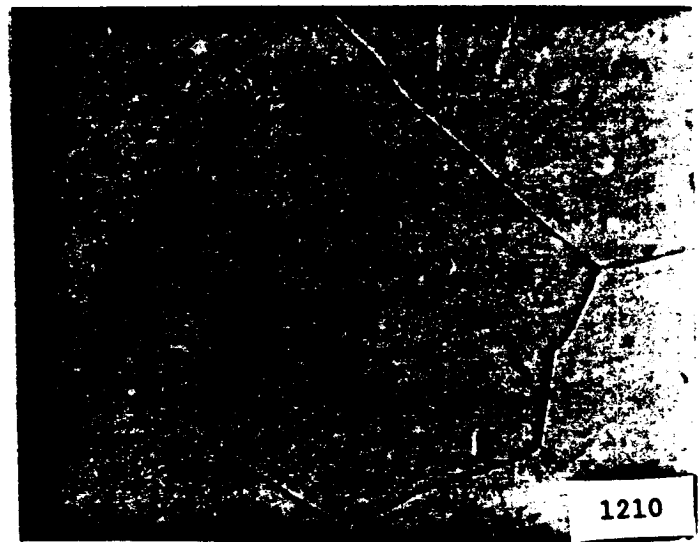
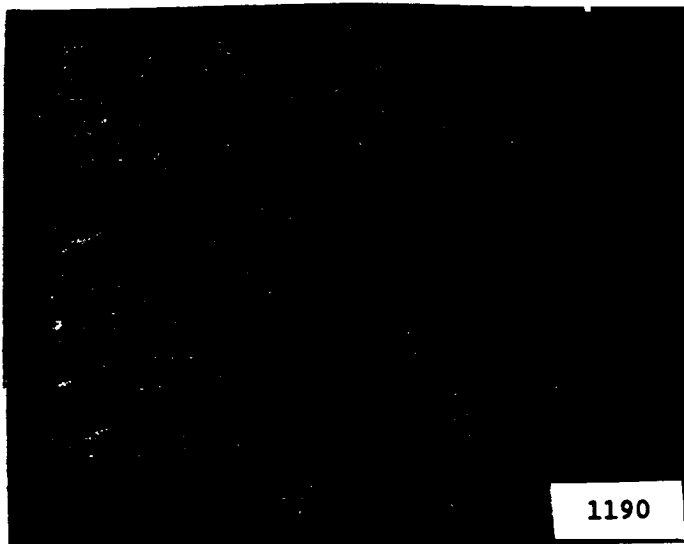
**Alloy 13: B**

Microstructures after quenching from 1190C, 1210C, 1230C, and 1250C using the Gleeble cycle of Figure 1.



Alloy 14: P

Microstructures after quenching from 1190C, 1210C, 1230C, and 1250C using the Gleeble cycle of Figure 1.



Alloy 20: Interstitial Free

Microstructures after quenching from 1190C, 1210C, 1230C, and 1250C using the Gleeble cycle of Figure 1.



Alloy 21: S (+)

Microstructures after quenching from 1235C using the Gleeble cycle of Figure 1.



Alloy 22: C (+)

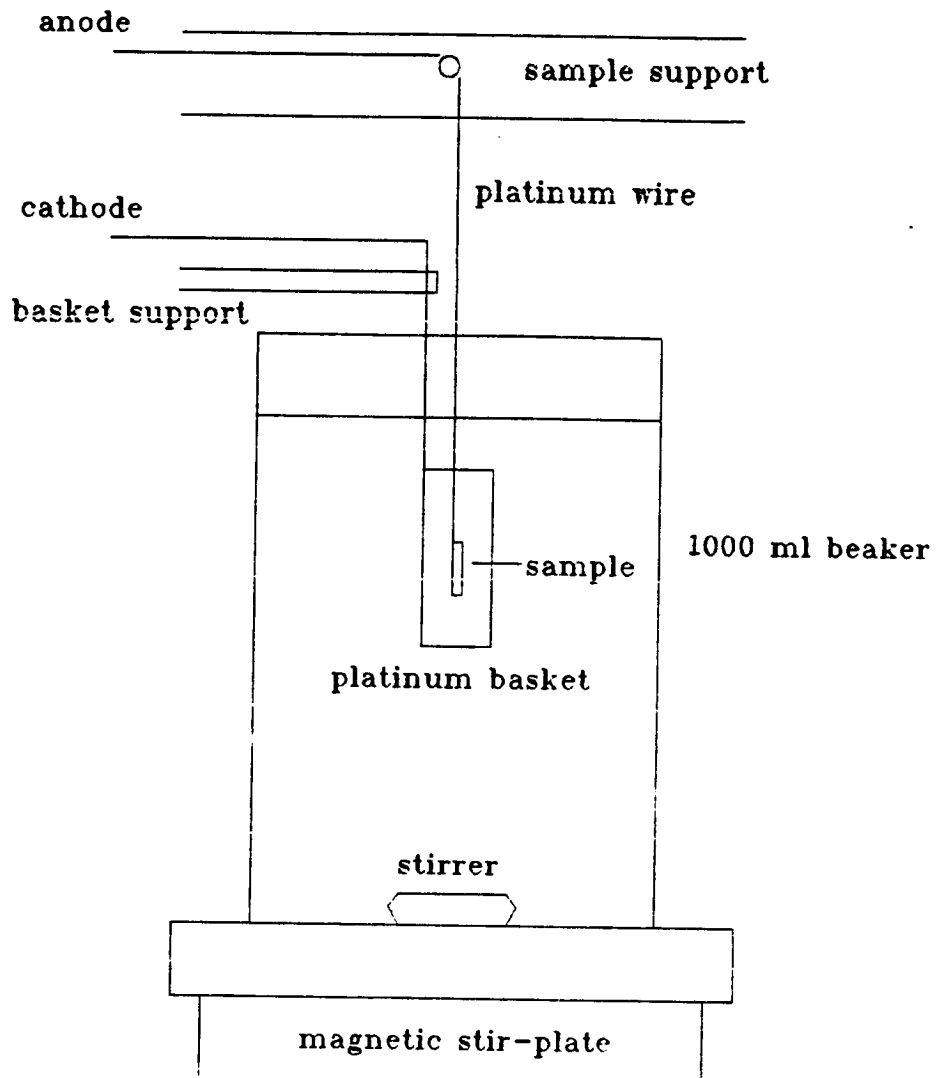
Microstructures after quenching from 1215C and 1235C using the Gleeble cycle of Figure 1.

## **Appendix D**

### **Scanning Auger Microscopy (SAM)**

- D1. Hydrogen Embrittlement Apparatus**
- D2. Selected SAM Microanalysis Spectra and Associated Micrographs**
  - D2.1 Alloy 3 (BSP)**
  - D2.2 Alloy 5 (BSC+)**
  - D2.3 Alloy 10 (CS)**
  - D2.3A (1093C) Alloy 27 (CS+) Homogenized 1 hour at 1093C**
  - D2.3B (927C) Alloy 27 (CS+) Homogenized 1 hour at 927C**
  - D2.4 Alloy 12 (BC)**
  - D2.5 Alloy 13 (B)**
  - D2.6 Alloy 20 (Clean)**
  - D2.7 Alloy 22 (C+)**
  - D2.8 Alloy 25 (S+)**



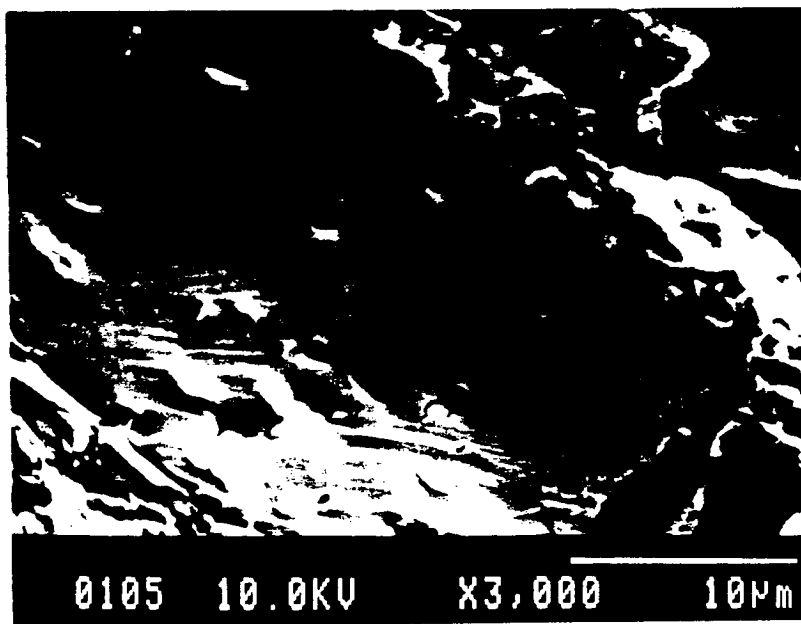
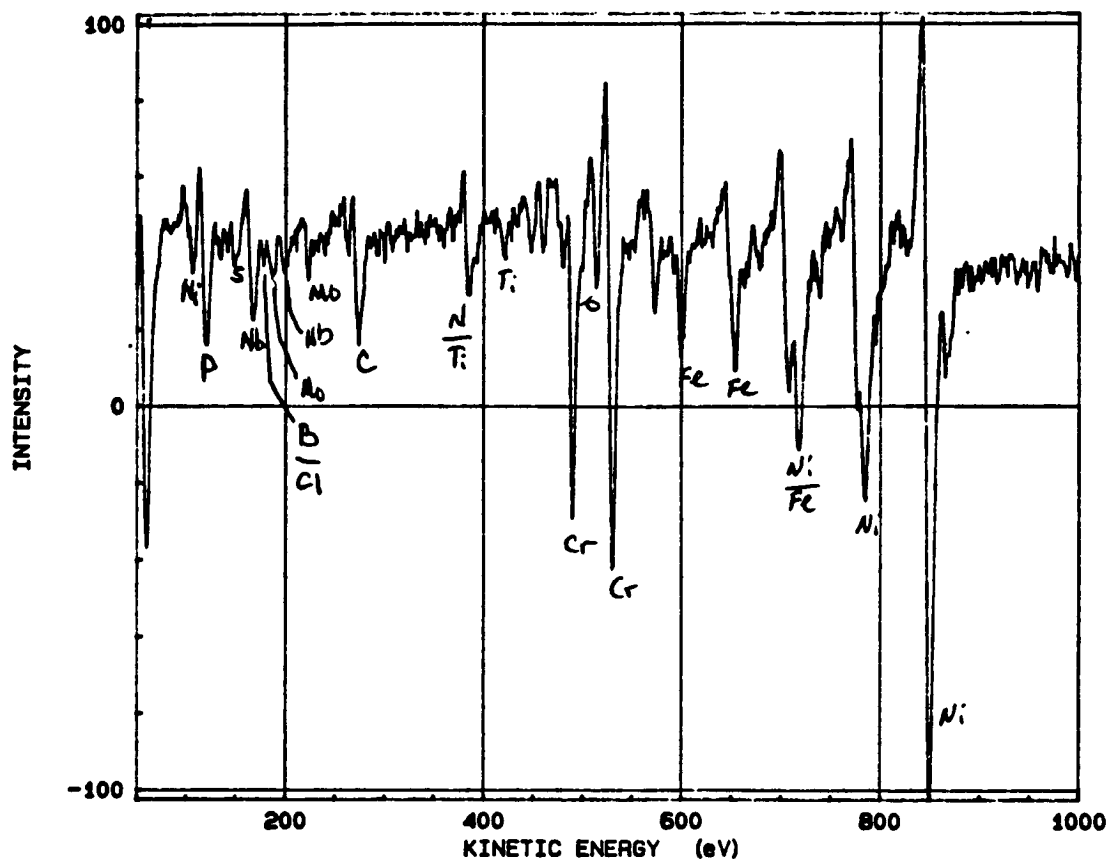


#### Charging Conditions

=====

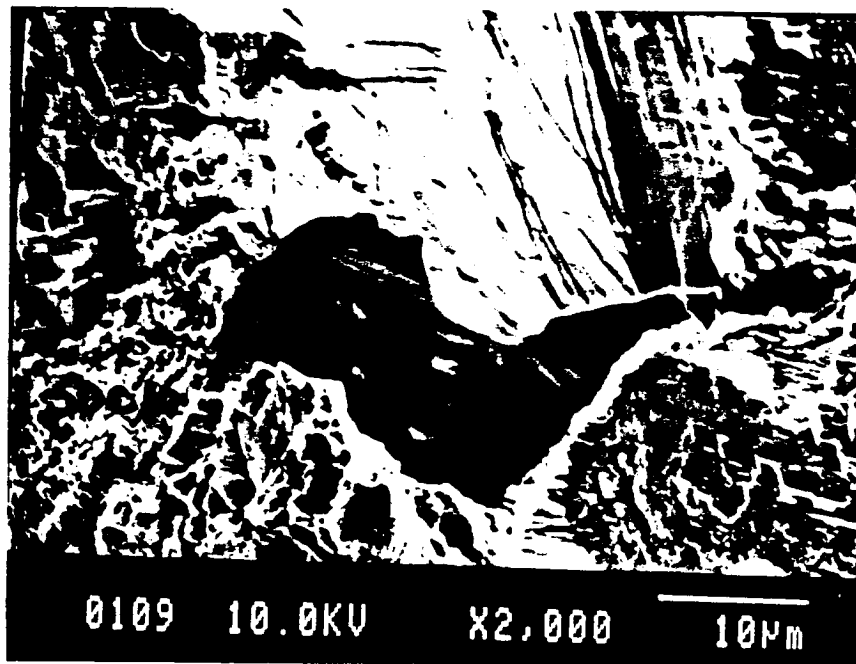
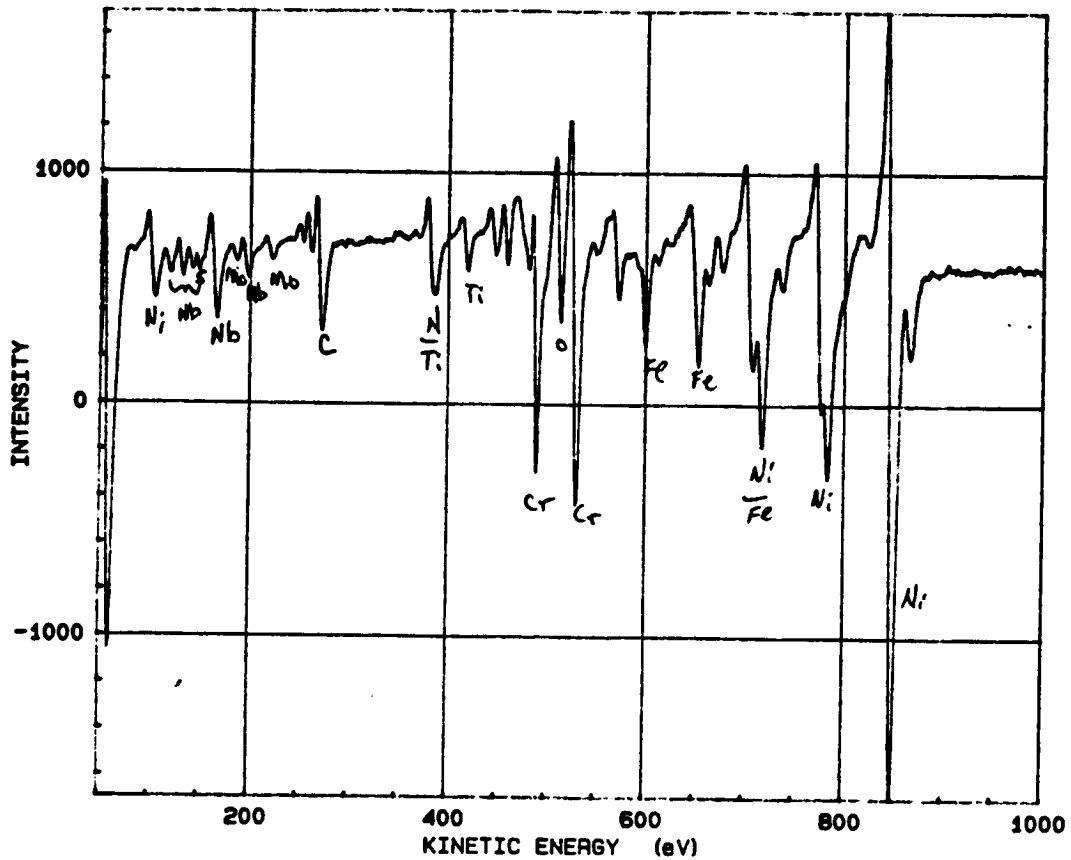
current density	$\approx 400 \text{ ma/cm}^2$
sample surface area	$0.5 - 1.0 \text{ cm}^2$
electrolyte	$0.5 \text{ m H}_2\text{SO}_4 + 50 \text{ mg NaAsO}_2 \text{ per l}$
electrolyte temperature	ambient
stir rate	slow
charging time	13 - 21 days

Hydrogen charging cell used to embrittle grain boundaries for exposure in the scanning Auger microscope.



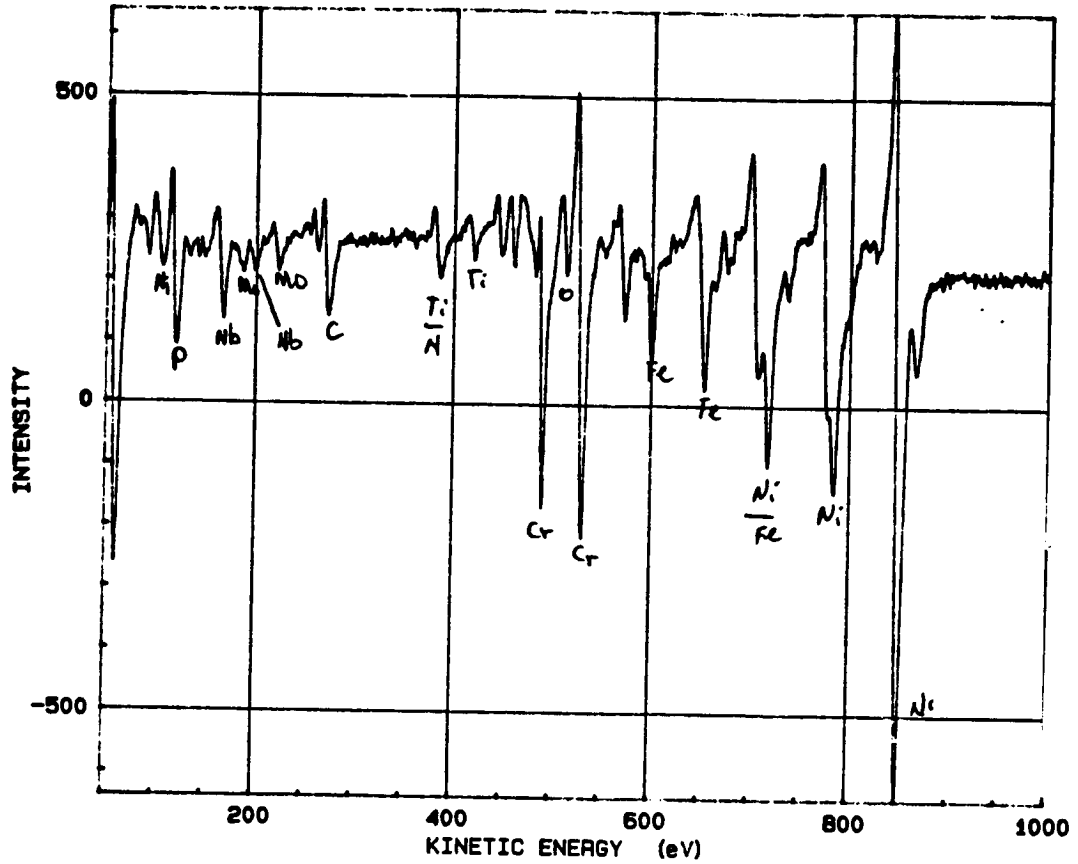
Alloy 3 (BS+P) Spot #50b8

SAM chemical spectra of a freshly fractured grain boundary surface. Significant levels of B, S, and P are present. Note that C and O are typical system contaminants.

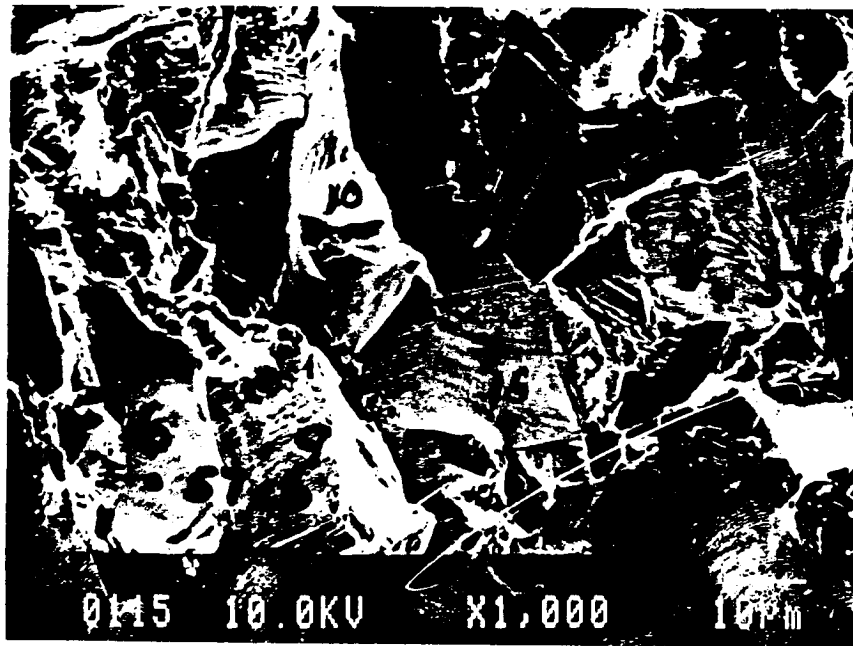


Alloy 3 (BS+P) Spot #50c10

SAM chemical spectra of a freshly fractured matrix surface. Significant levels of only S are present. Note that C and O are typical contaminants.



Ops

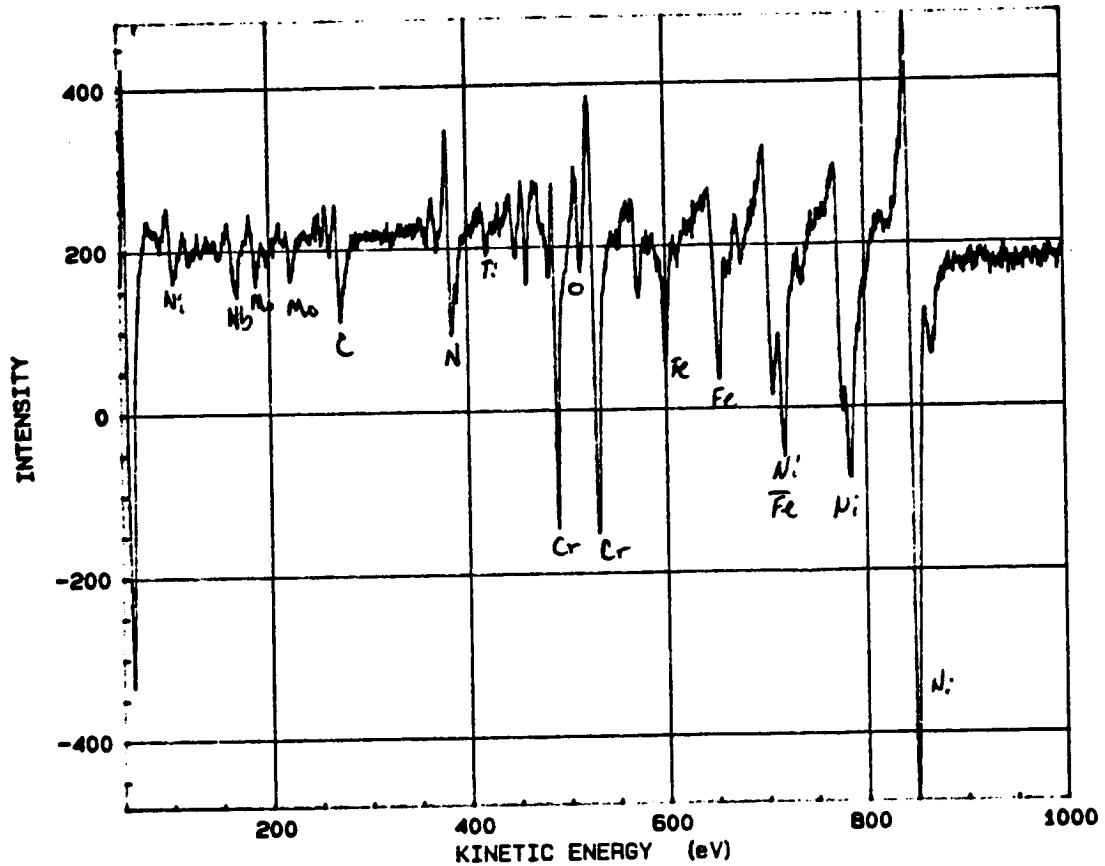


Alloy 5 (BSC+) Spot #57c8

SAM chemical spectra of a freshly fractured grain boundary surface. Significant levels of only P are present. Note that C and O are typical system contaminants.

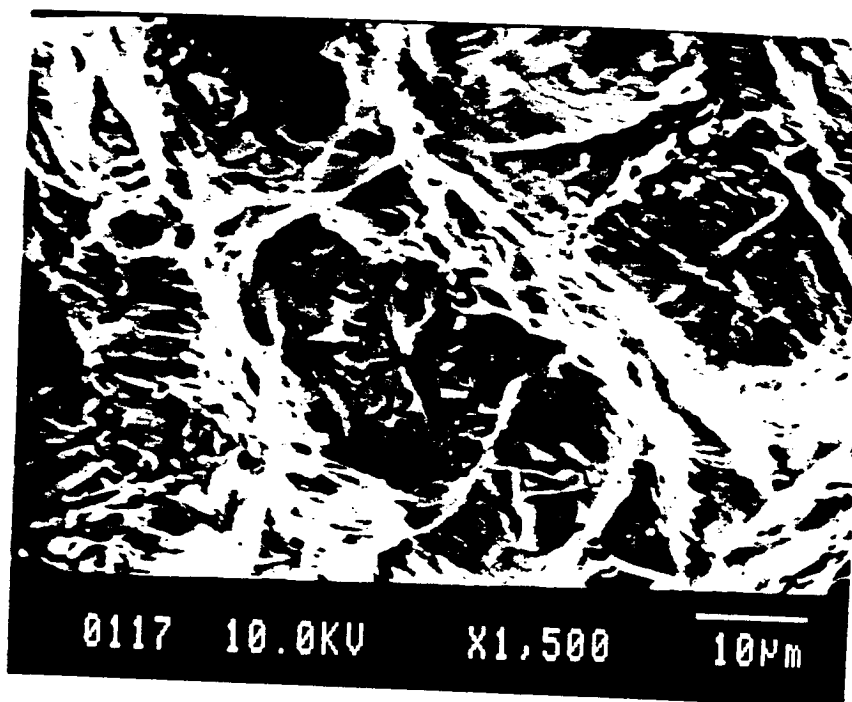
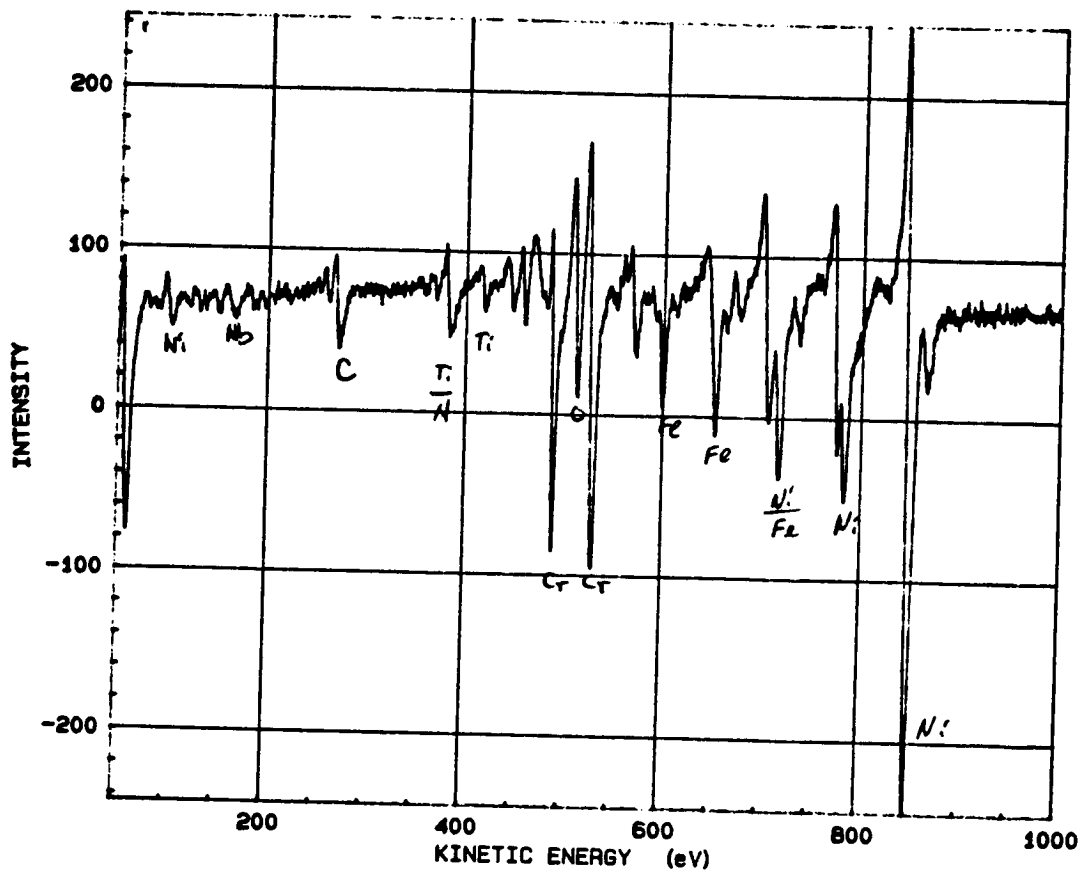
ORIGINAL PAGE IS  
OF POOR QUALITY

File : 9005701BD.SSP



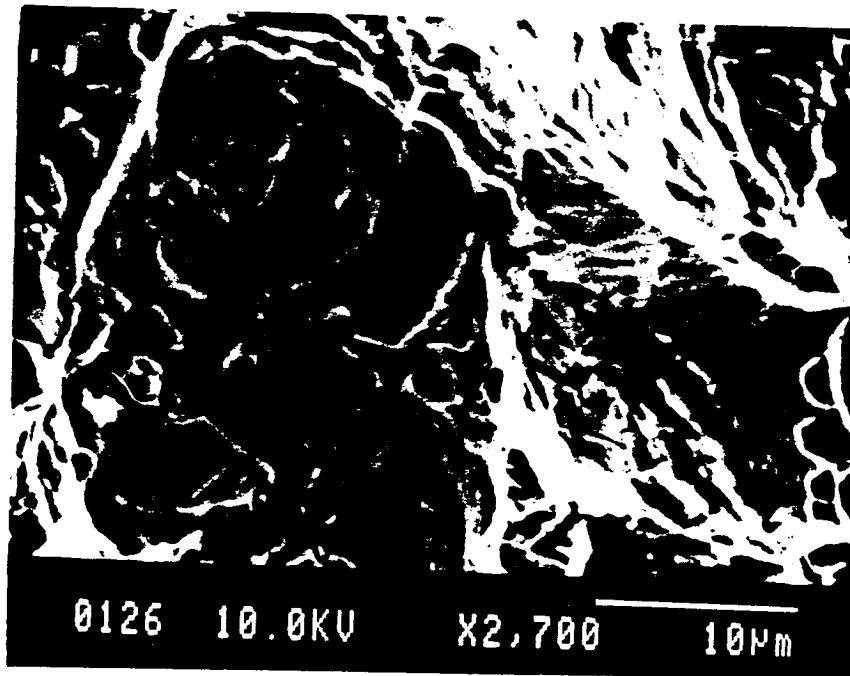
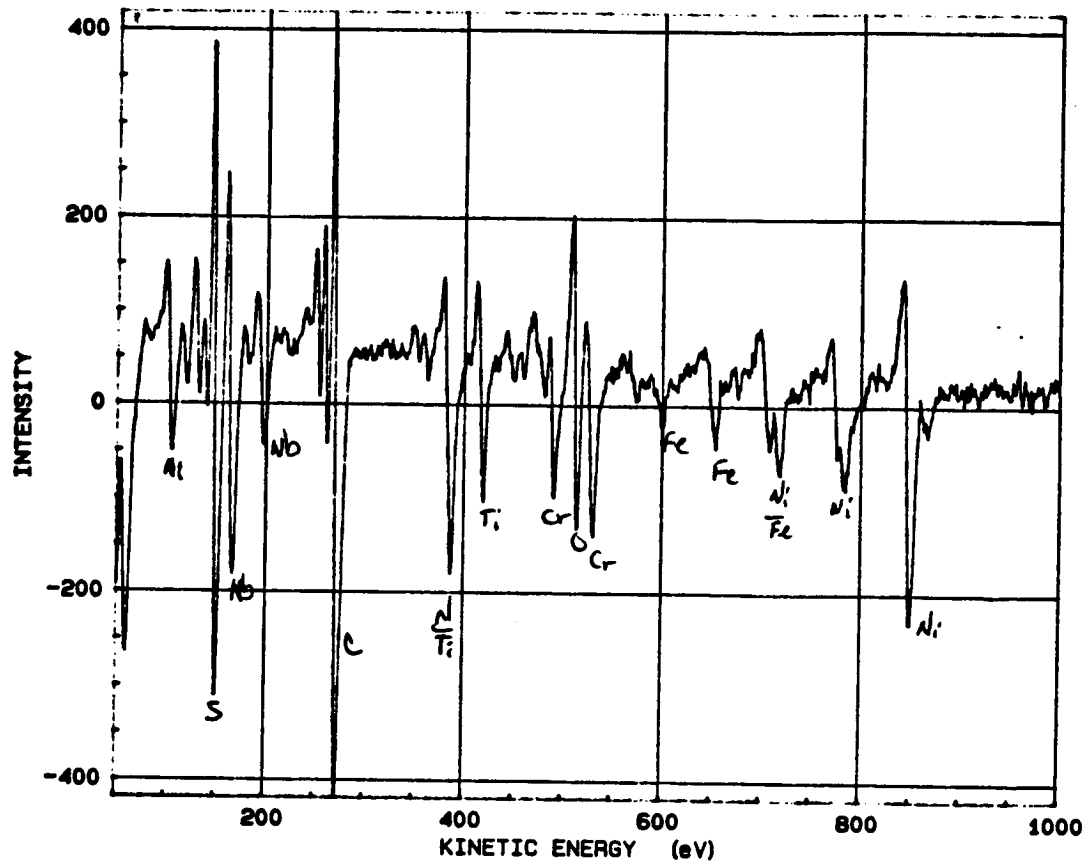
Alloy 5 (BSC+) Spot #57c8

SAM chemical spectra of the grain boundary surface of D2.2.1 after sputter cleaning. Significant levels of none of the dopants are present. Note that C and O are typical system contaminants.



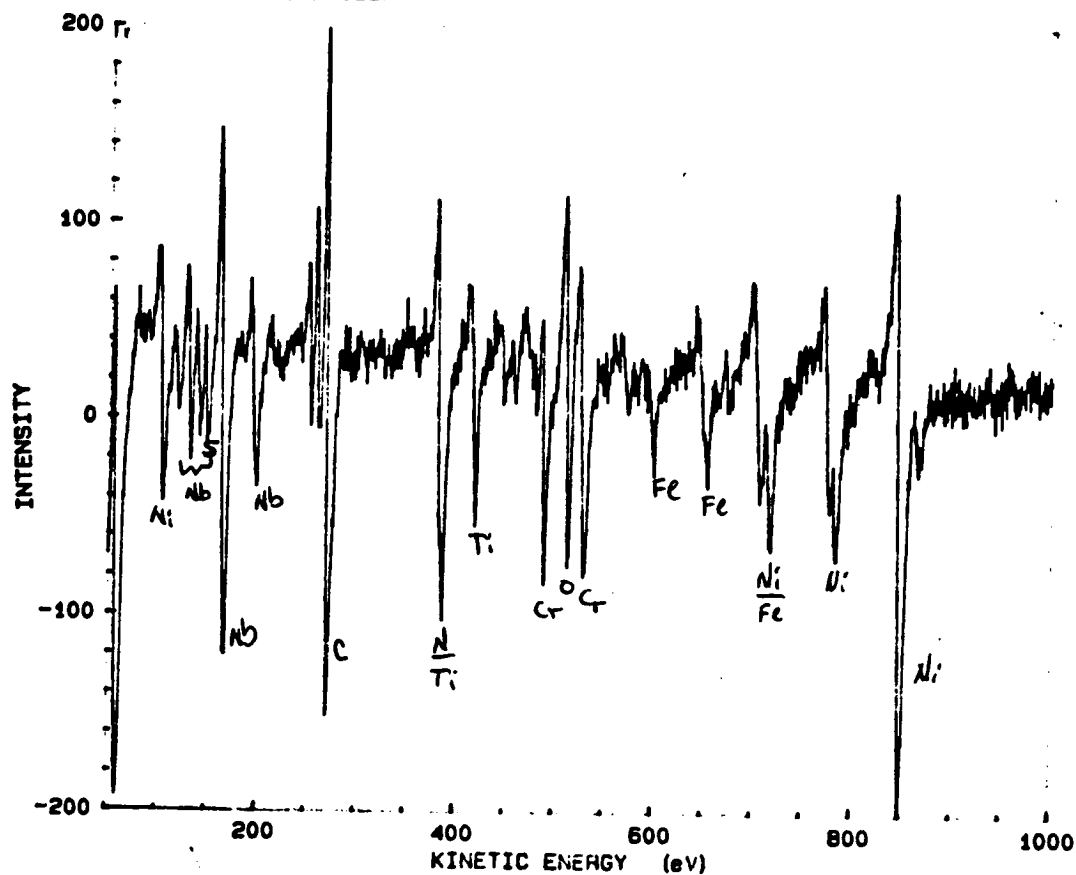
Alloy 5 (BSC+) Spot #57d15

SAM chemical spectra of a freshly fractured matrix surface. Significant levels of none of the dopants are present. Note that C and O are typical system contaminants.



Alloy 5 (BSC+) Spot #57e21

SAM chemical spectra of a freshly fractured carbide surface. Significant levels of only S are present. Note that O is a typical system contaminate.

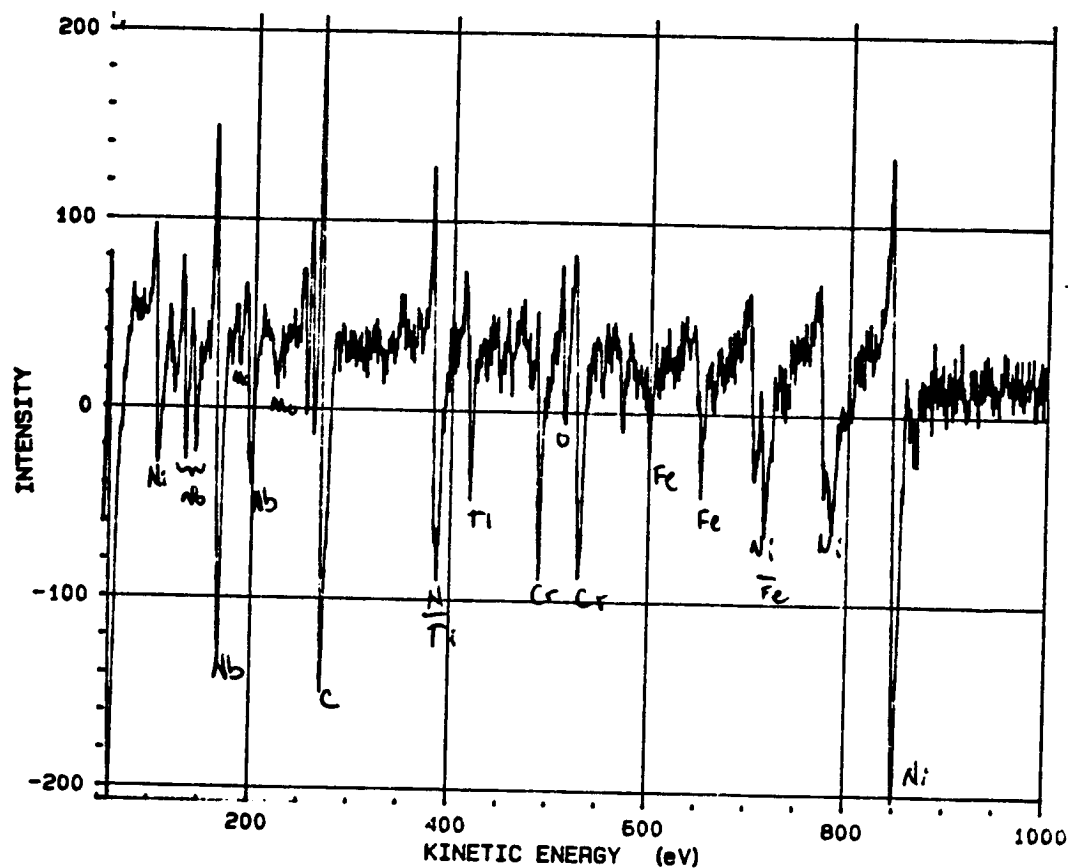


Alloy 5 (BSC+) Spot #57e21

SAM chemical spectra of the carbide surface of D2.2.3 sputter cleaned for 1 minute. Significant levels of only S are present. Note that O is a typical system contaminate.



File : 9005701BJ.SSP

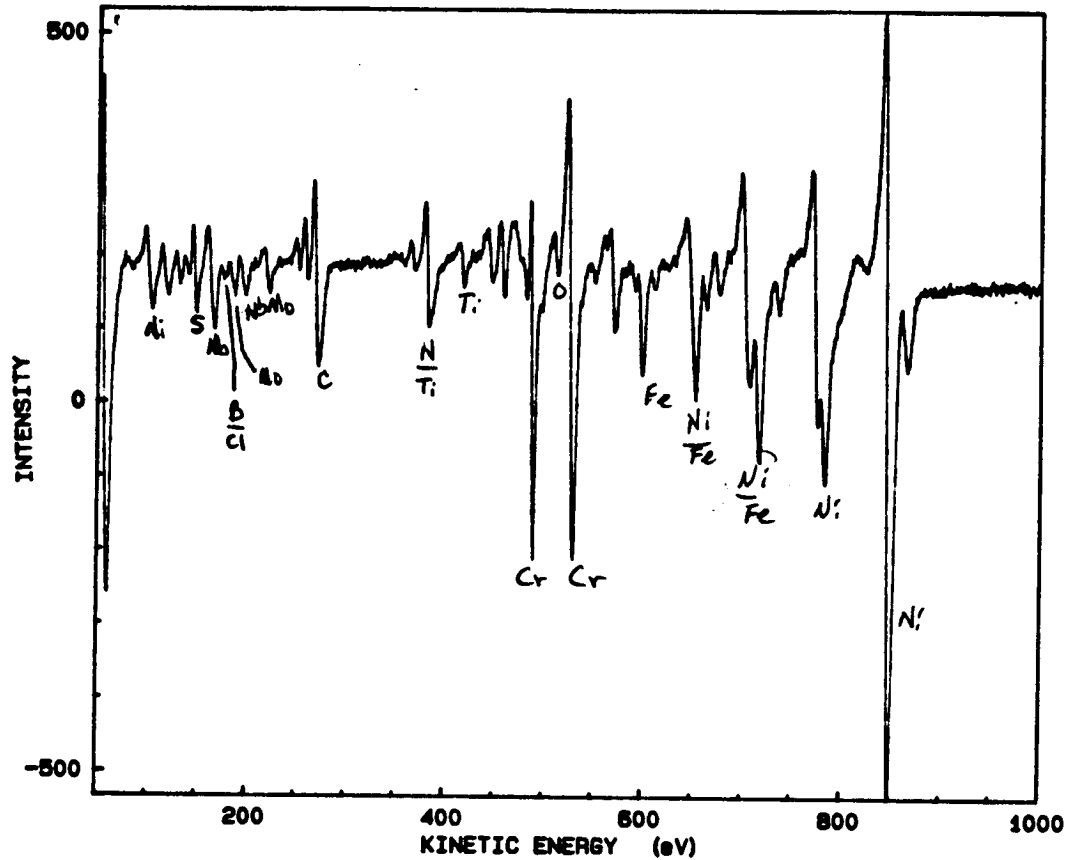


Alloy 5 (BSC+) Spot #57e21

SAM chemical spectra of the carbide surface of D2.2.3 sputtered cleaned for 3 minutes. Significant levels of none of the dopants are present. Note that O is a typical system contaminate.

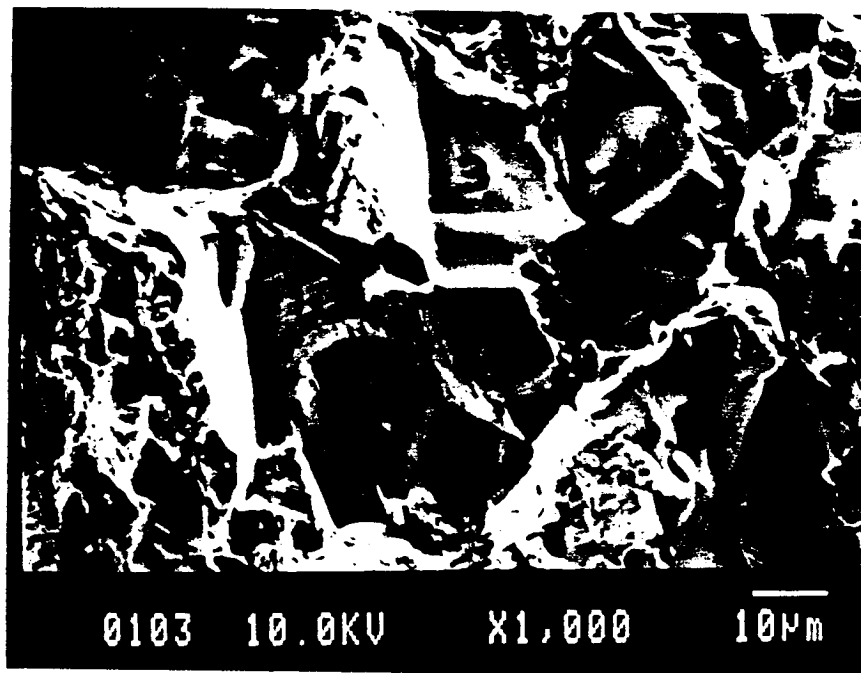
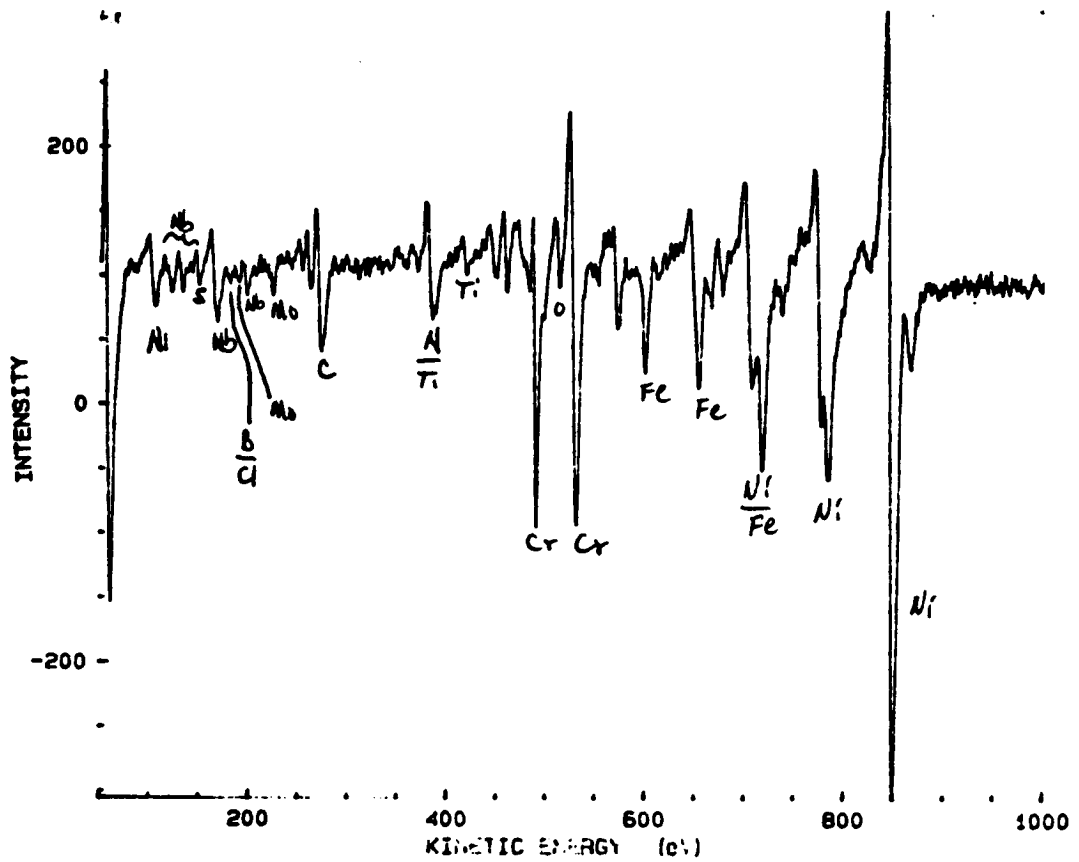
ORIGINAL PAGE IS  
OF POOR QUALITY

D2.2.3C



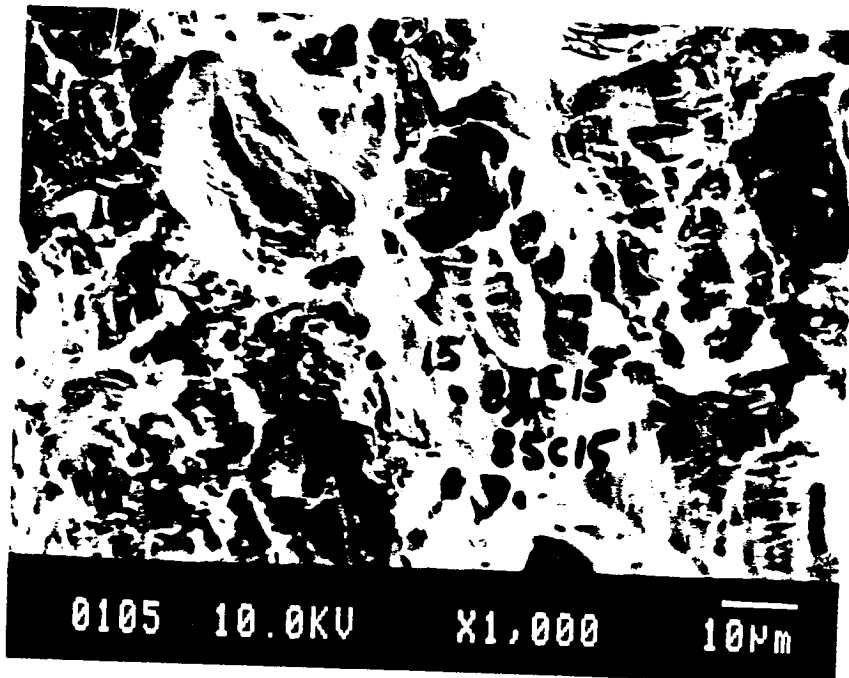
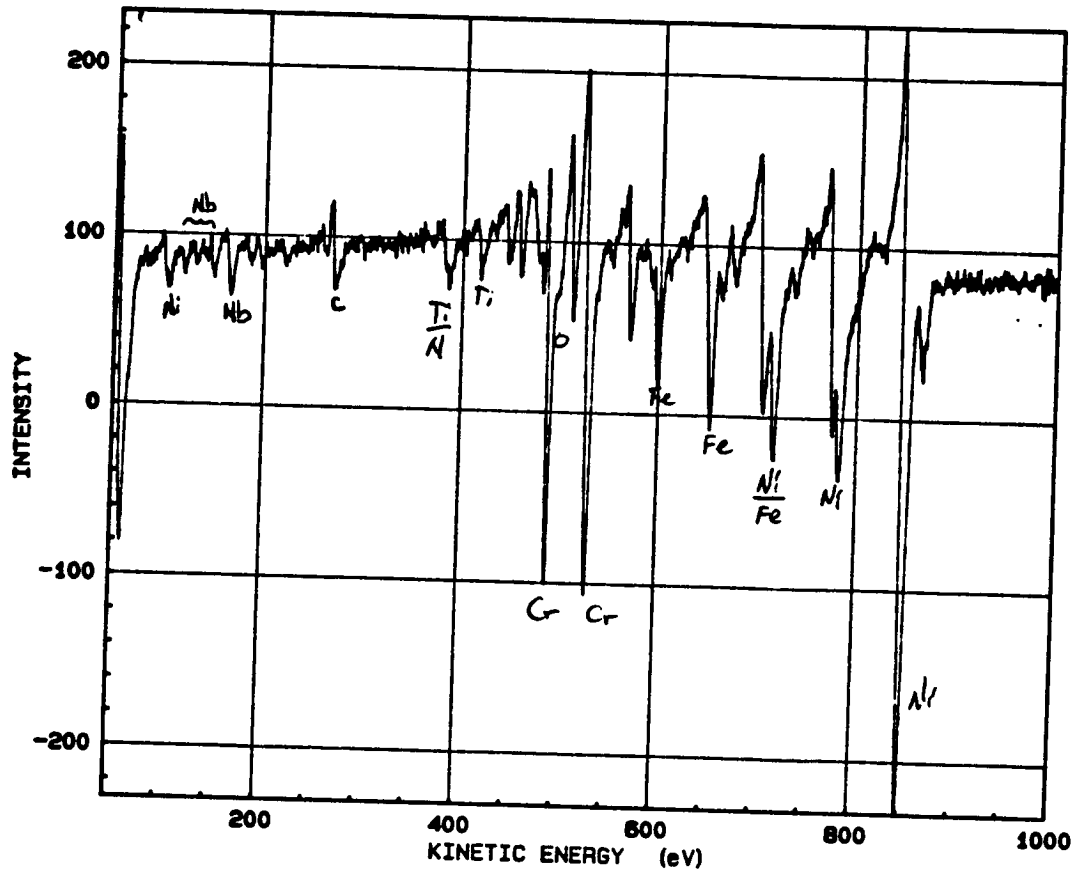
Alloy 10 (CS) Spot #85a7

SAM chemical spectra of a freshly fractured grain boundary surface. Significant levels of S and B are present. Note that C and O are typical system contaminants.



Alloy 10 (CS) Spot #85a1

SAM chemical spectra of freshly fractured grain boundary surface. Significant levels of S and B are present. Note that C and O are typical system contaminants.

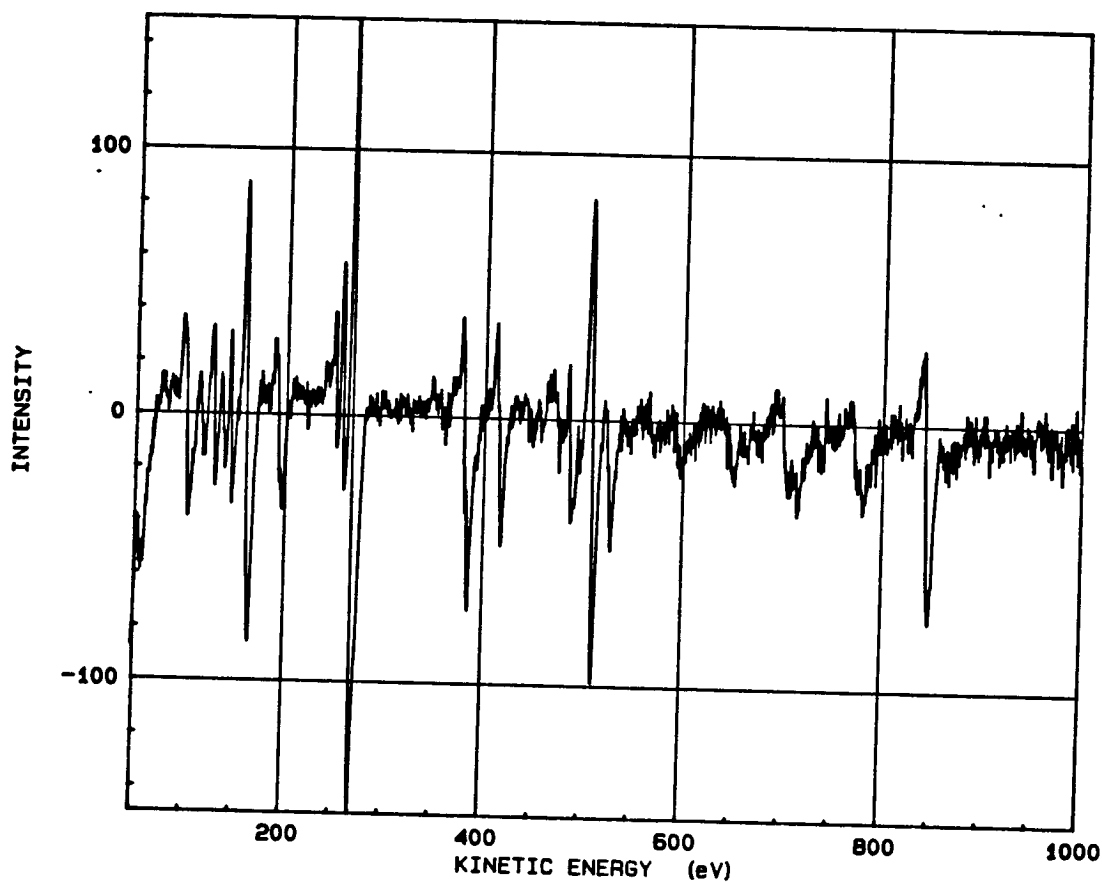


Alloy 10 (CS) Spot #85c15

SAM chemical spectra of freshly fractured matrix surface. Significant levels of only S are present. Note that C and O are typical system contaminants.

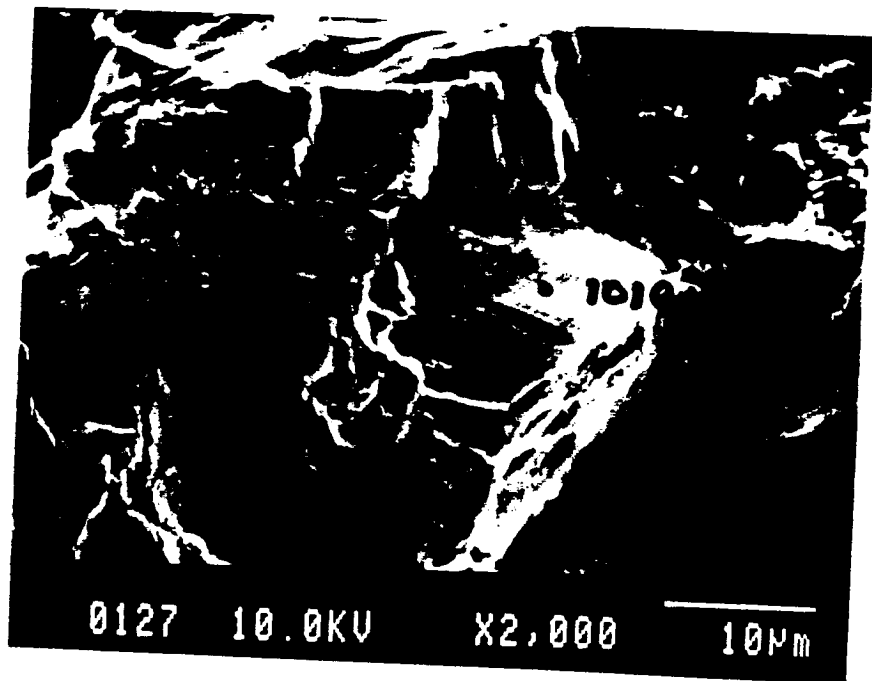
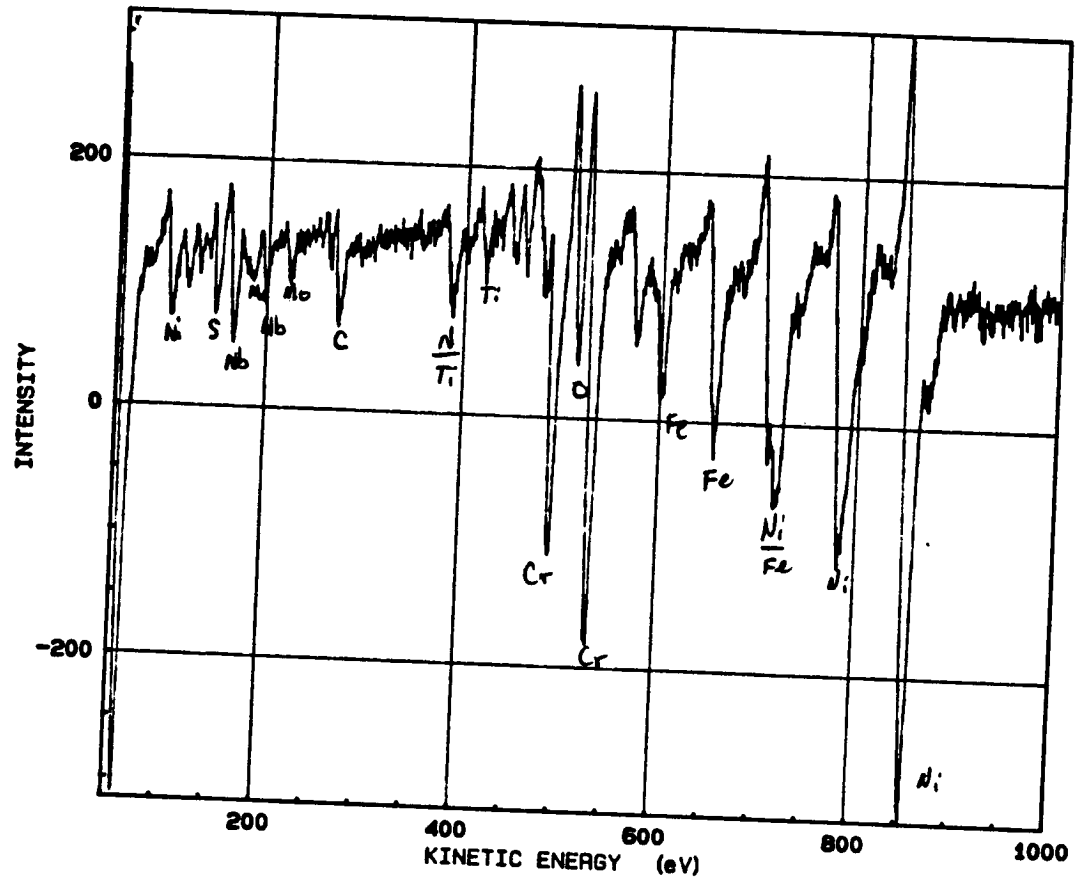
ORIGINAL PAGE IS  
OF POOR QUALITY

File : 9008501AT.SSP



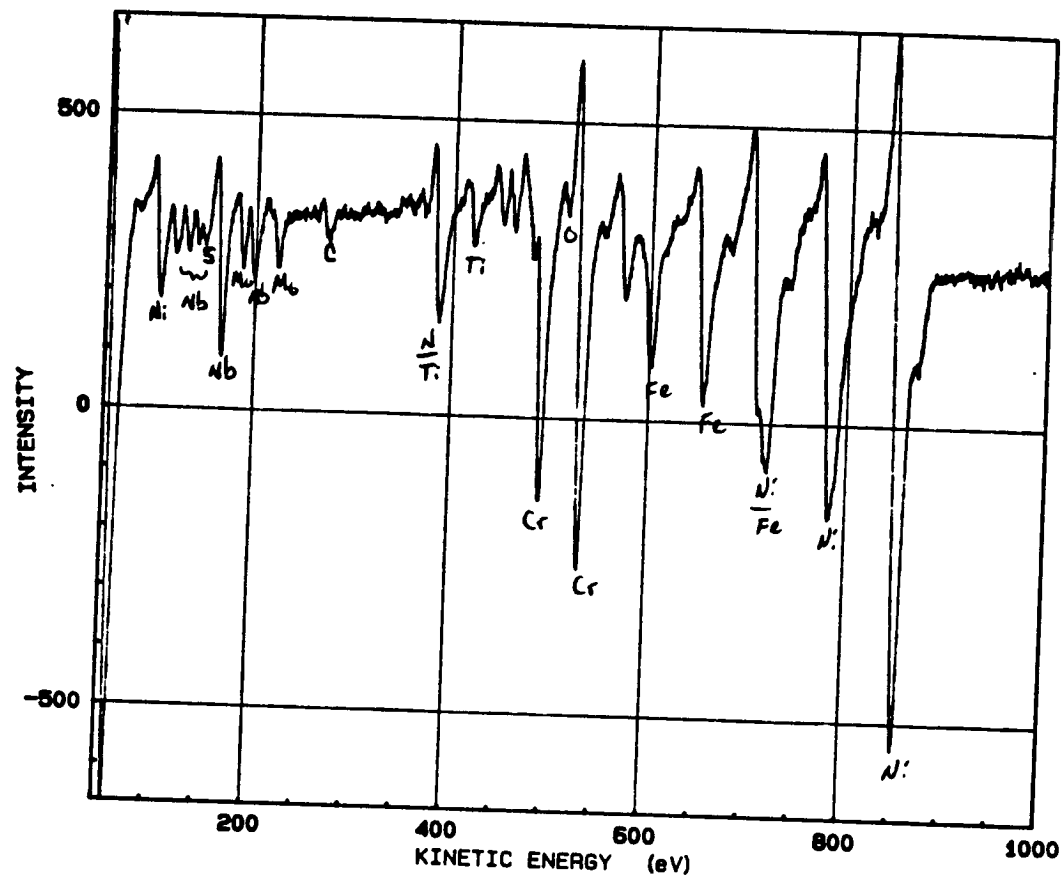
Alloy 10(SC) Spot #85c16

SAM chemical spectra of a freshly fractured carbide interface surface. Significant levels of only S are present. Note that C and O are typical system contaminants.



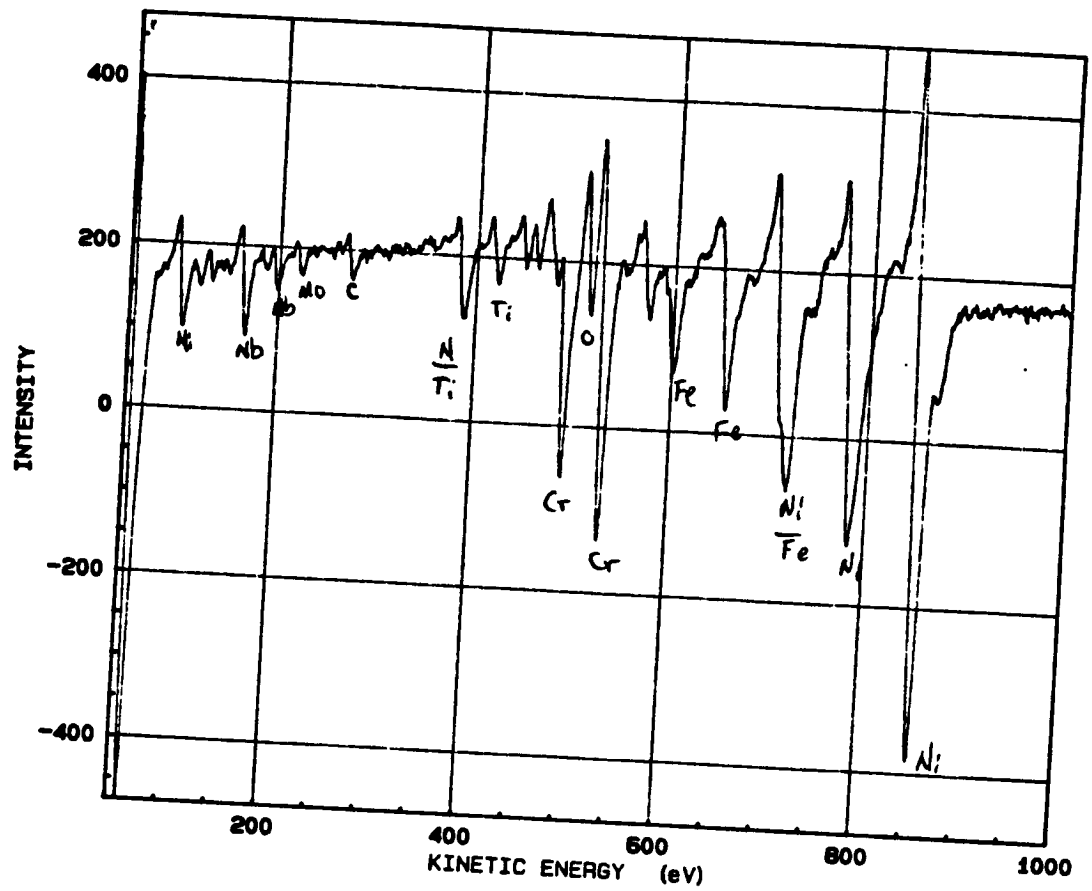
Alloy 27 (CS+) as cast Spot #101e10

SAM chemical spectra of a freshly fractured grain boundary surface. Significant levels of only S are present. Note that C and O are typical system contaminants.



Alloy 27 (CS+) as cast Spot #101e10

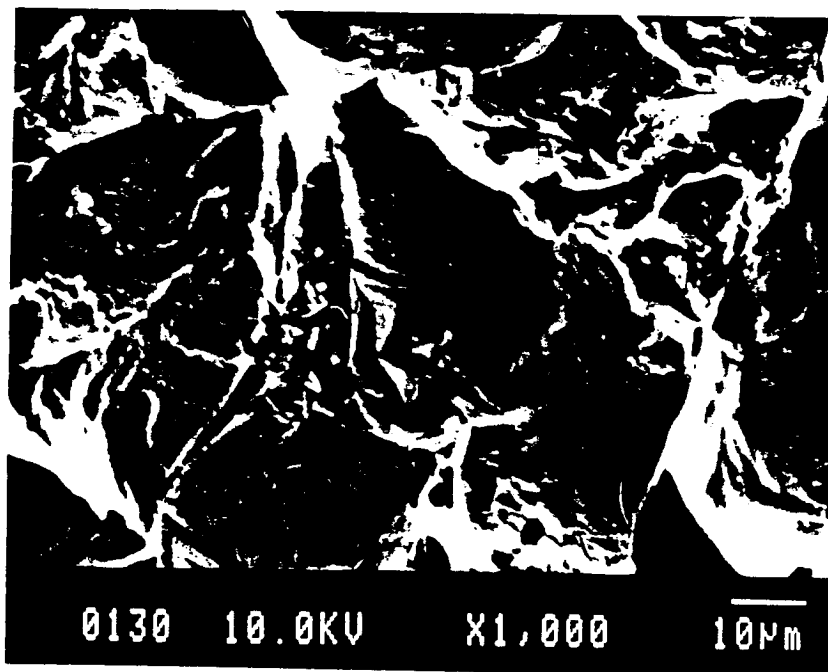
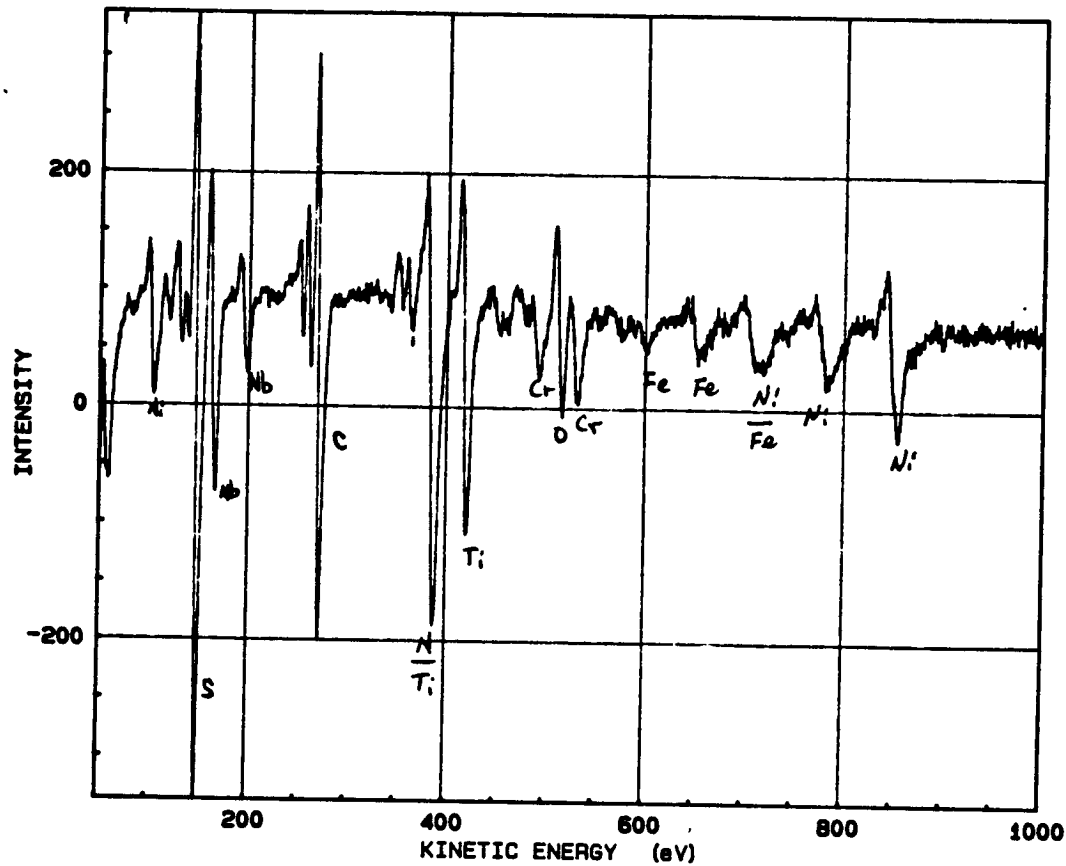
SAM chemical spectra of the grain boundary surface after sputter cleaning. Significant levels of only S (very small) are present. Note that C and O are typical system contaminants.



Alloy 27 (CS+) as cast Spot #101c7

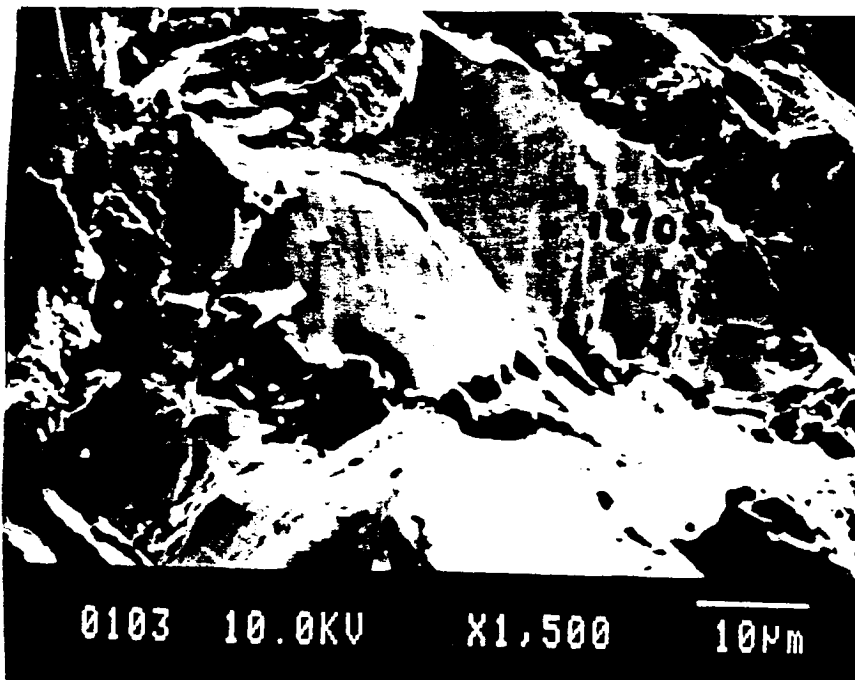
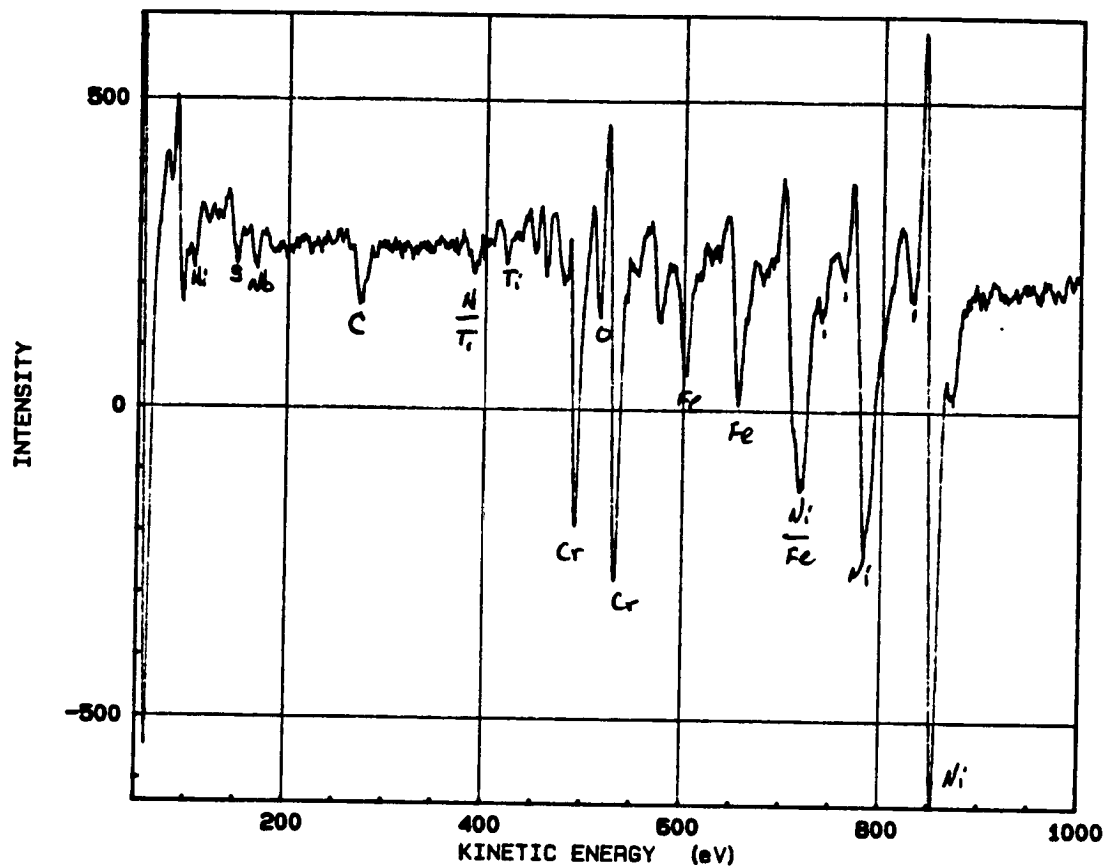
SAM chemical spectra of a freshly fractured matrix surface. Significant levels of none of the dopants are present. Note that C and O are typical system contaminants.





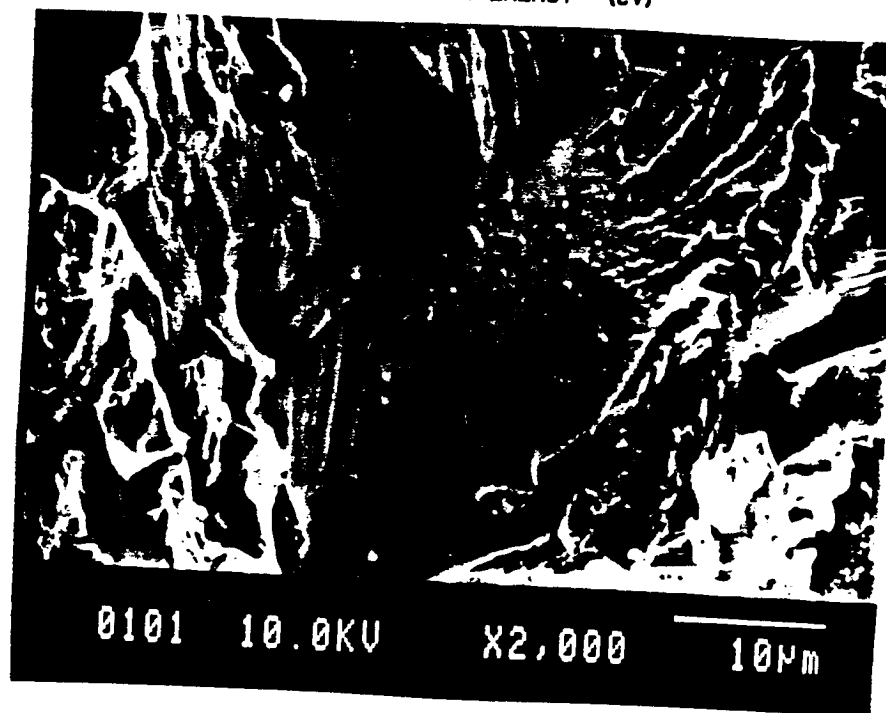
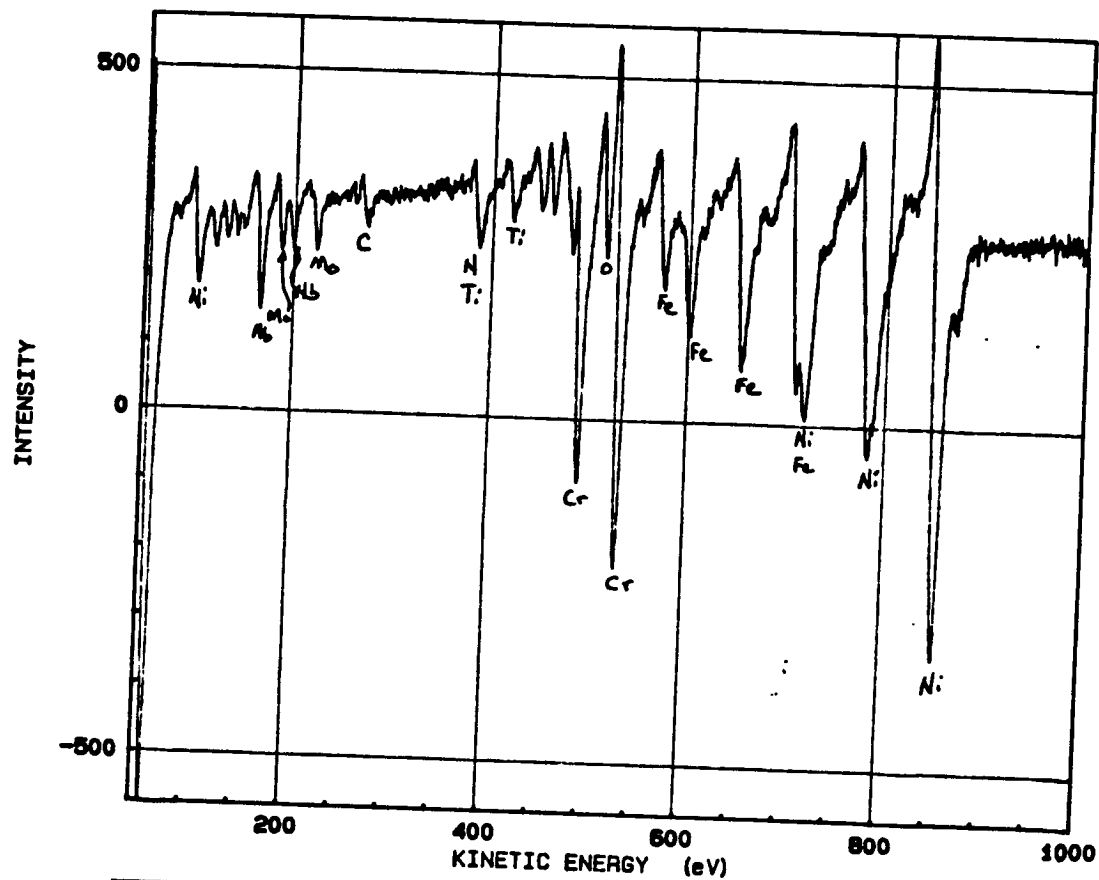
Alloy 27 (CS+) as cast Spot #101d9

SAM chemical spectra of a freshly fractured carbide surface. Significant levels of only S are present. Note that C and O are typical system contaminants.



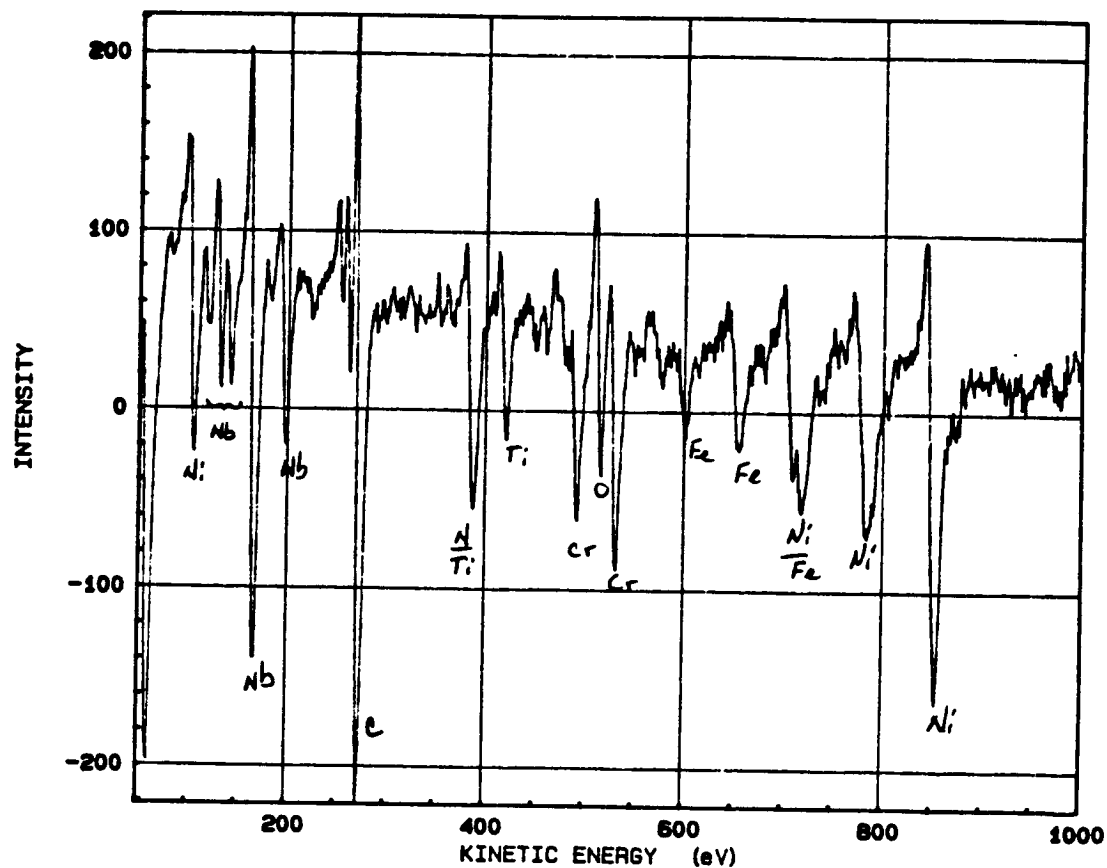
Alloy 27(CS+) Homogenized 1 hour at 1093C Spot #127c5

SAM chemical spectra of a freshly fractured ground boundary surface. Significant levels of only S are present. Note that C and O are typical system contaminants.



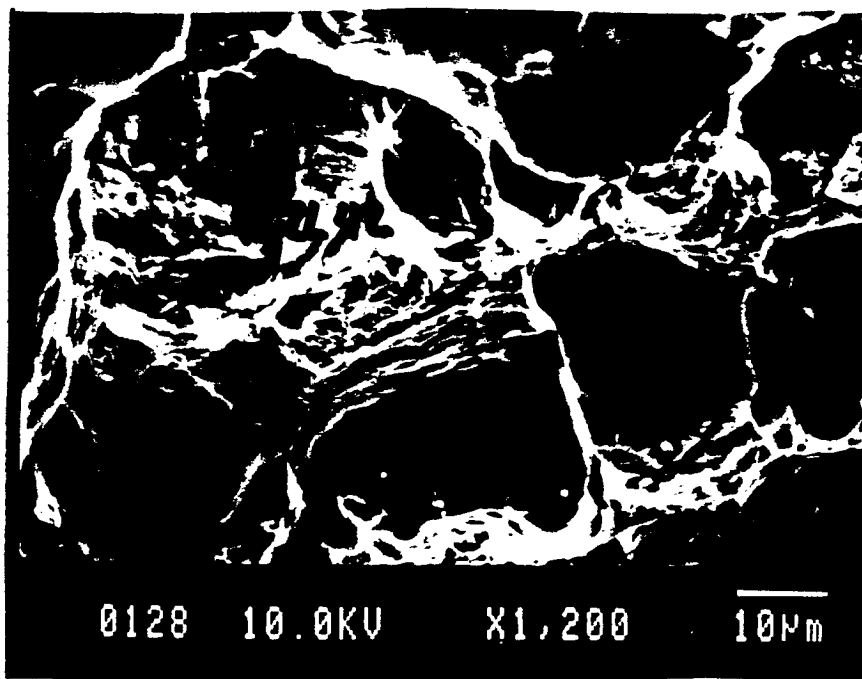
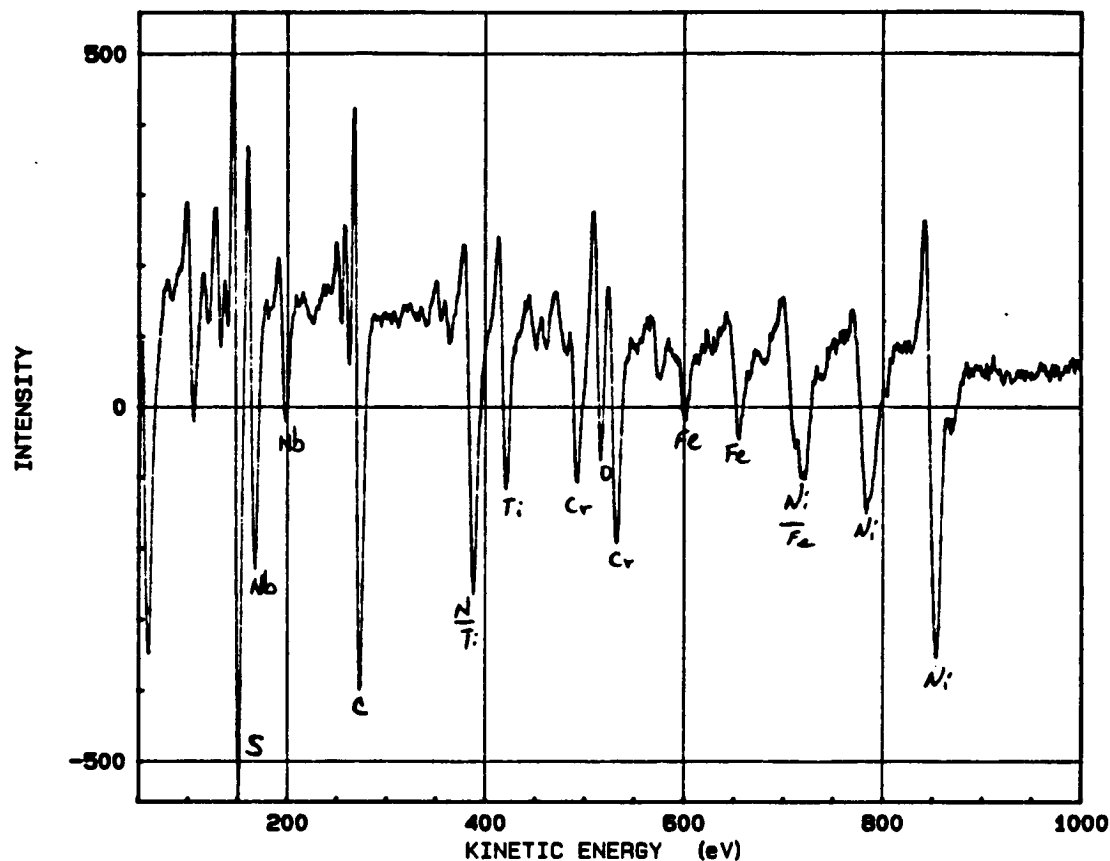
Alloy 27(CS+) Homogenized 1 hour at 1093C Spot #127b3

SAM chemical spectra of a sputtered grain boundary surface. Significant levels of none of the dopants are present. Note that C and O are typical system contaminants.



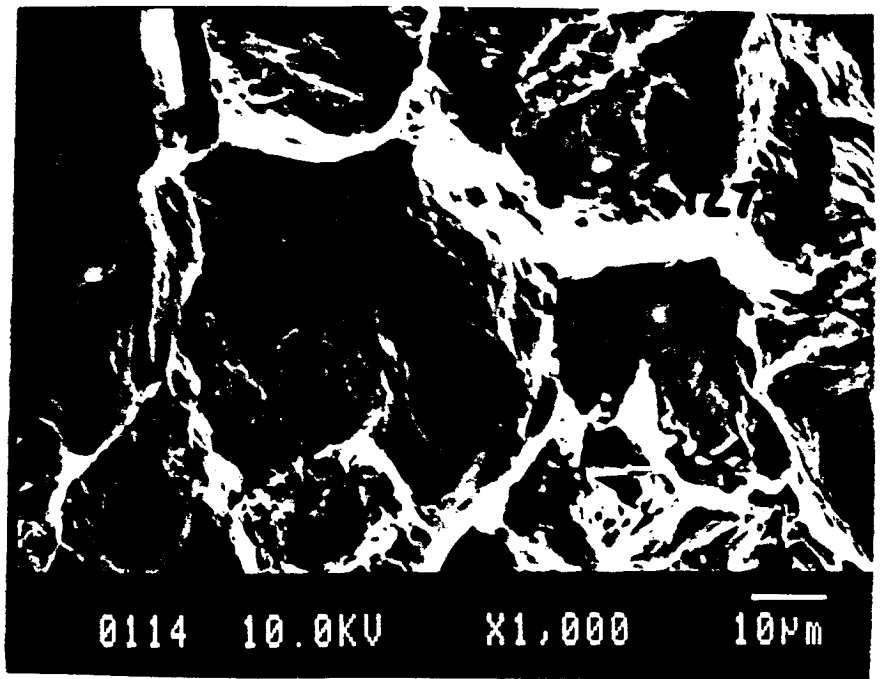
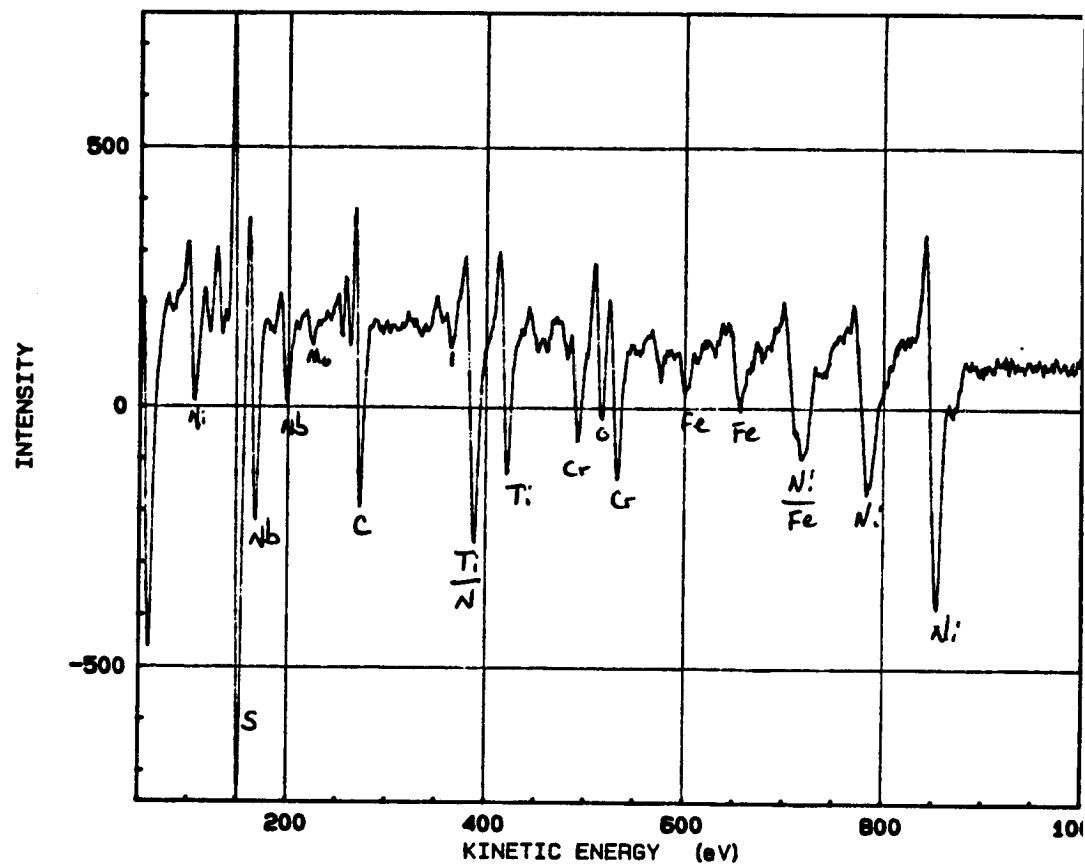
Alloy 27(CS+) Homogenized 1 hour at 1093C Spot 127d12

SAM chemical spectra of a cleaved carbide surface. Significant levels of none of the dopants are present. Note that C and O are typical system contaminants.



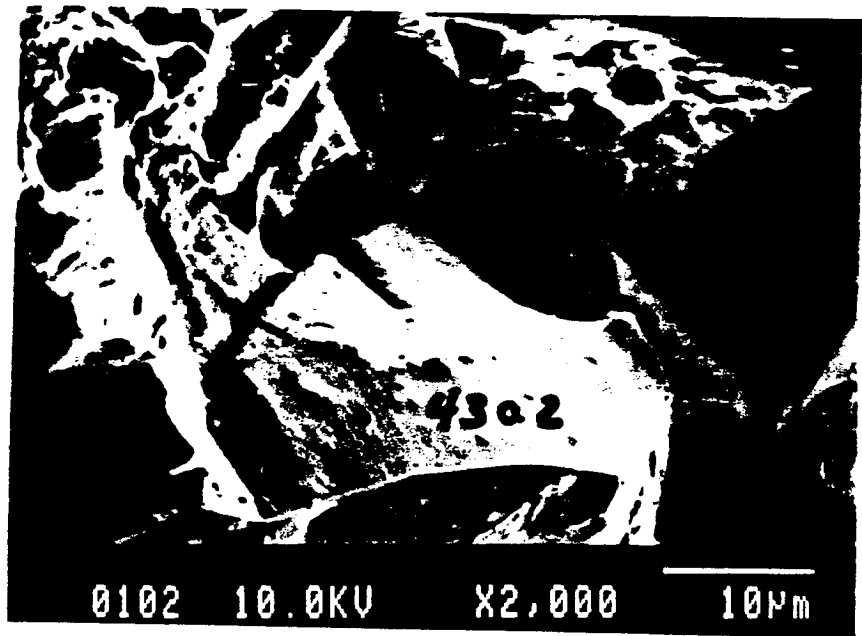
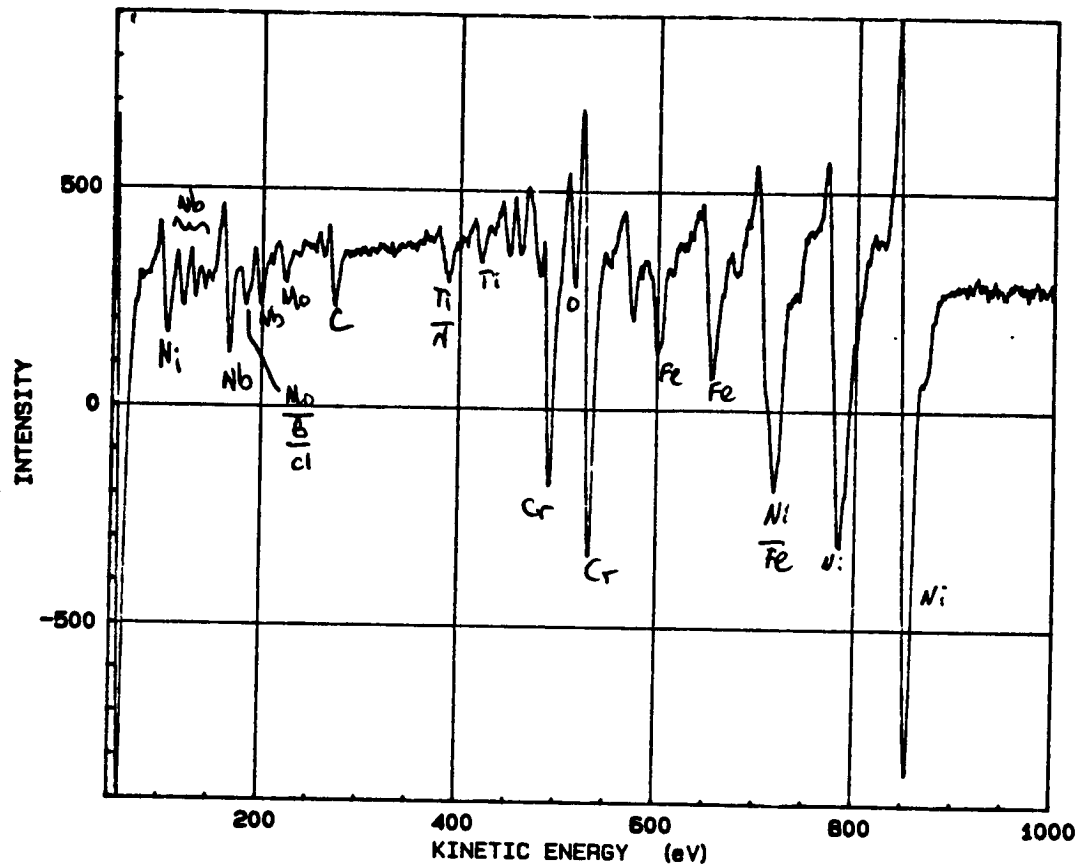
Alloy 27(CS+) Homogenized 1 hour at 1093C Spot 127142

SAM chemical spectra of a freshly fractured carbide/matrix interface surface. Significant levels of S and maybe B are present. Note that O is a typical system contaminate.



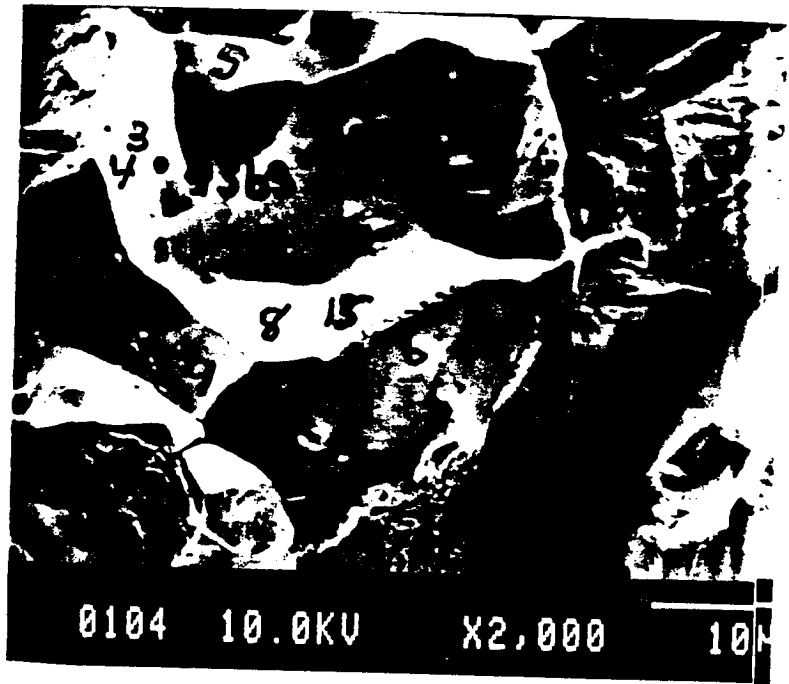
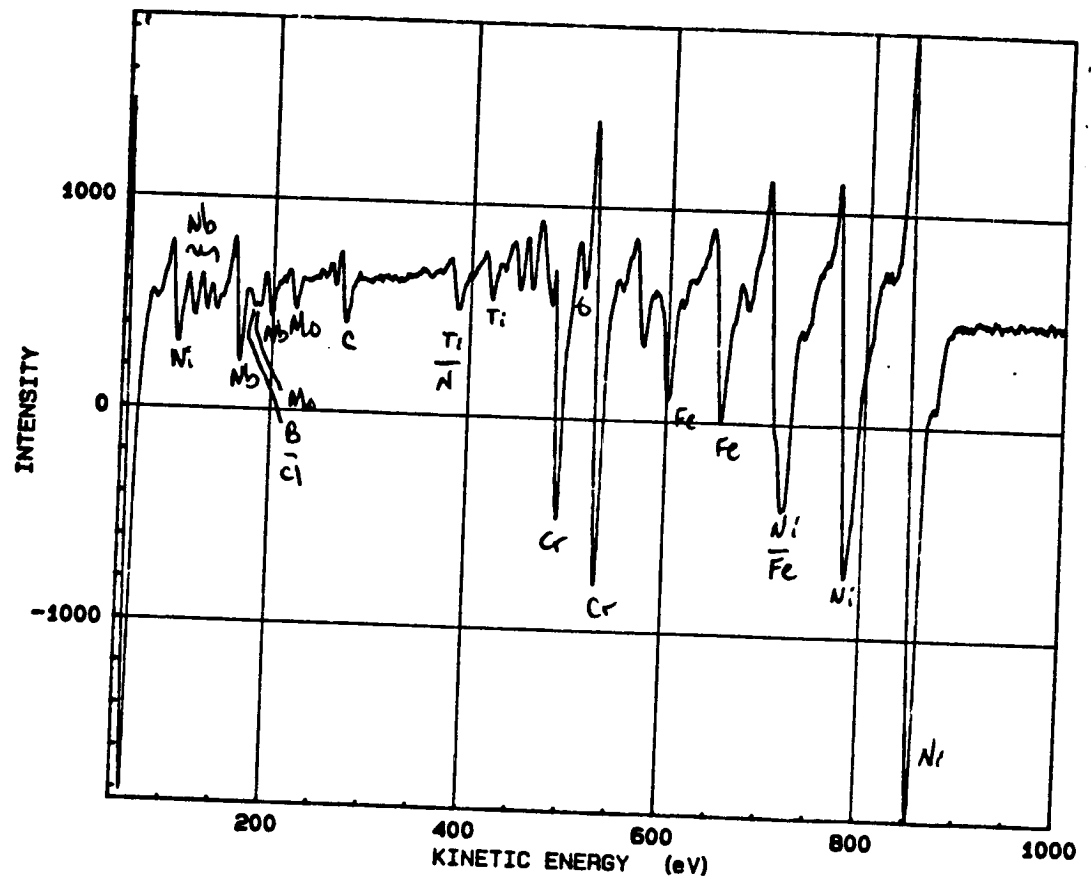
Alloy 27(CS+) Homogenized 1 hour at 1093C Spot 127g17

SAM chemical spectra of a freshly fractured eutectic surface. Significant levels of only S are present. Note that C and O are typical system contaminants.



Alloy 12 (BC) Spot #43a2

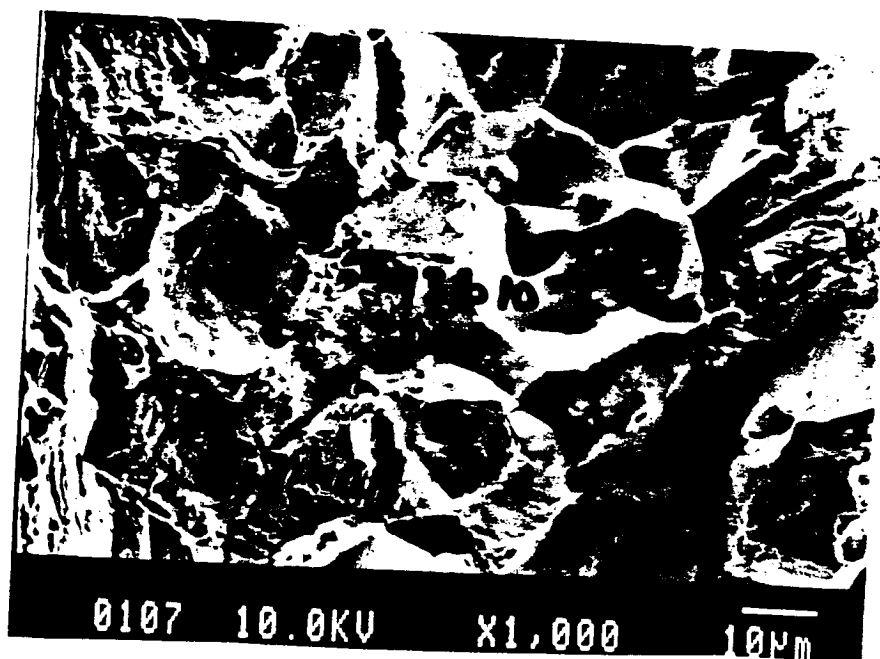
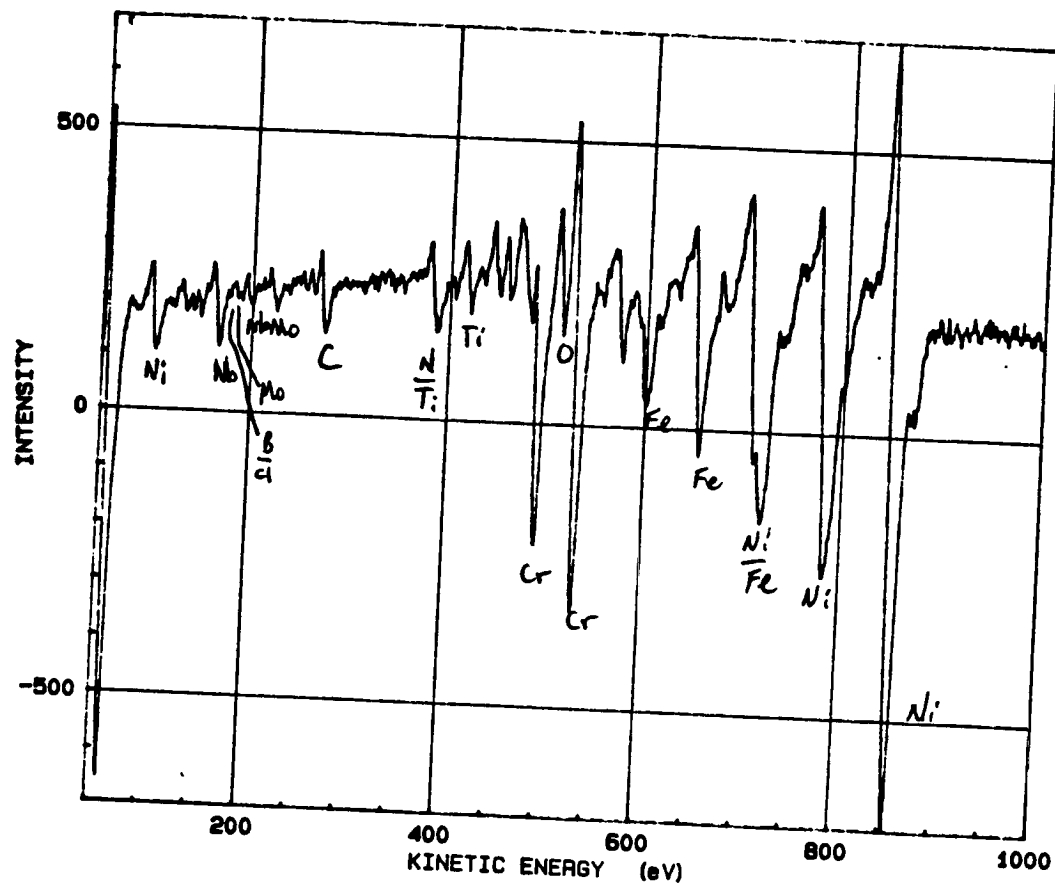
SAM chemical spectra of freshly fractured grain boundary surface. Significant levels of only B are present. Note that C and O are typical system contaminants.



Alloy 12 (BC) Spot #43b3

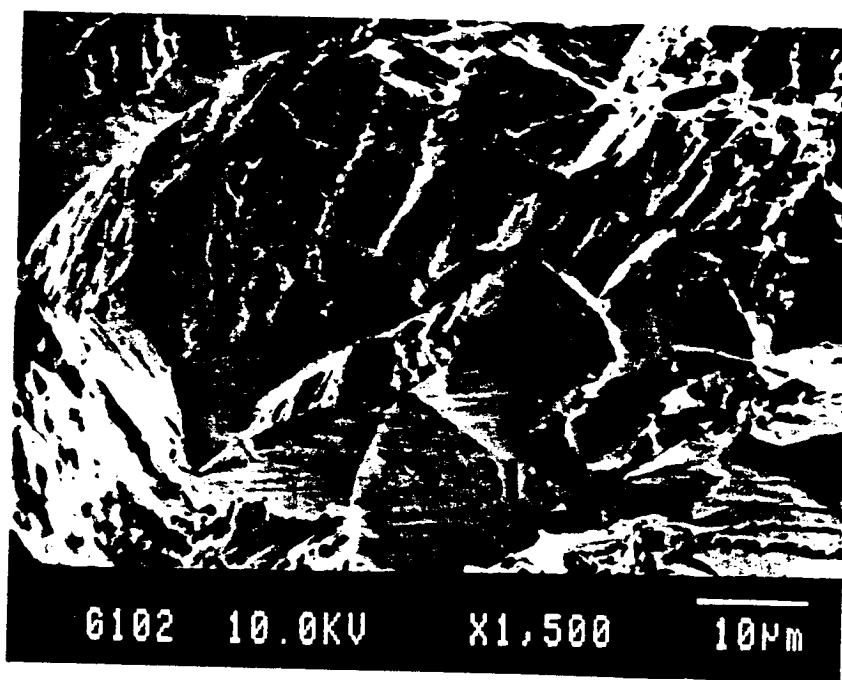
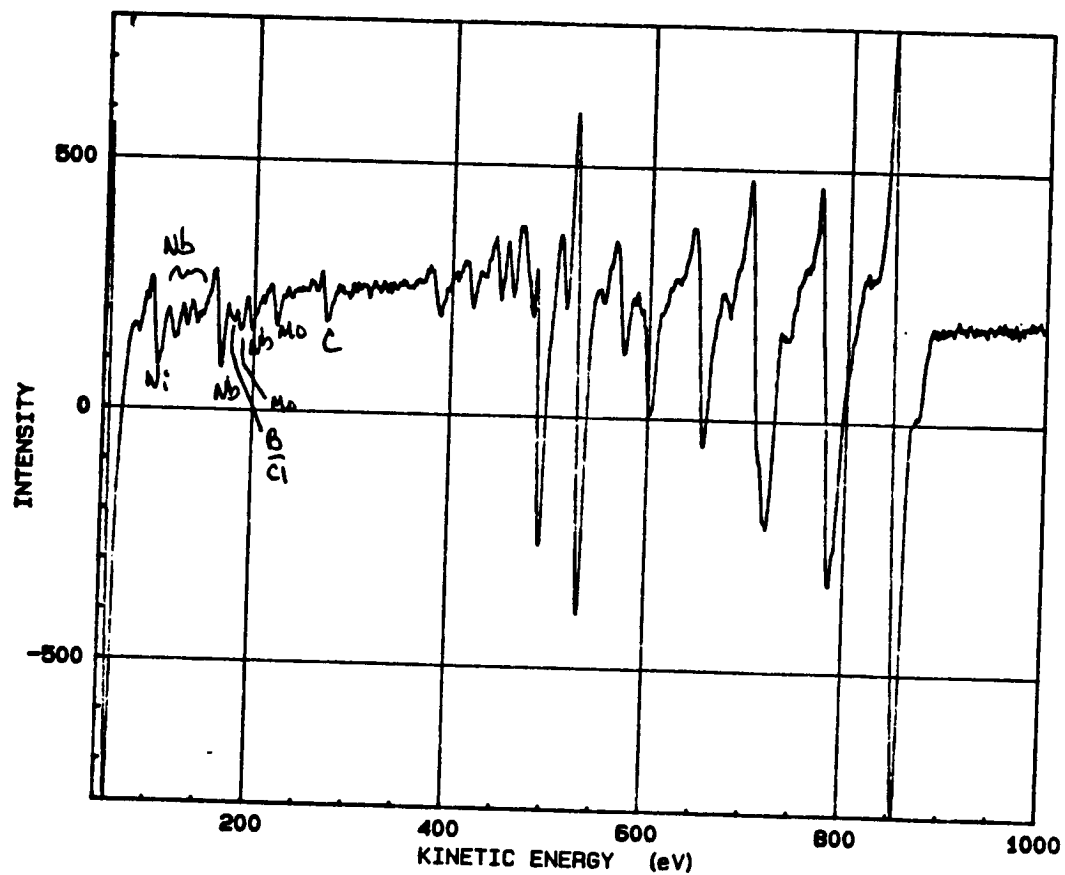
SAM chemical spectra of freshly fractured grain boundary surface. Significant levels of only B are present. Note that C and O are typical system contaminants.





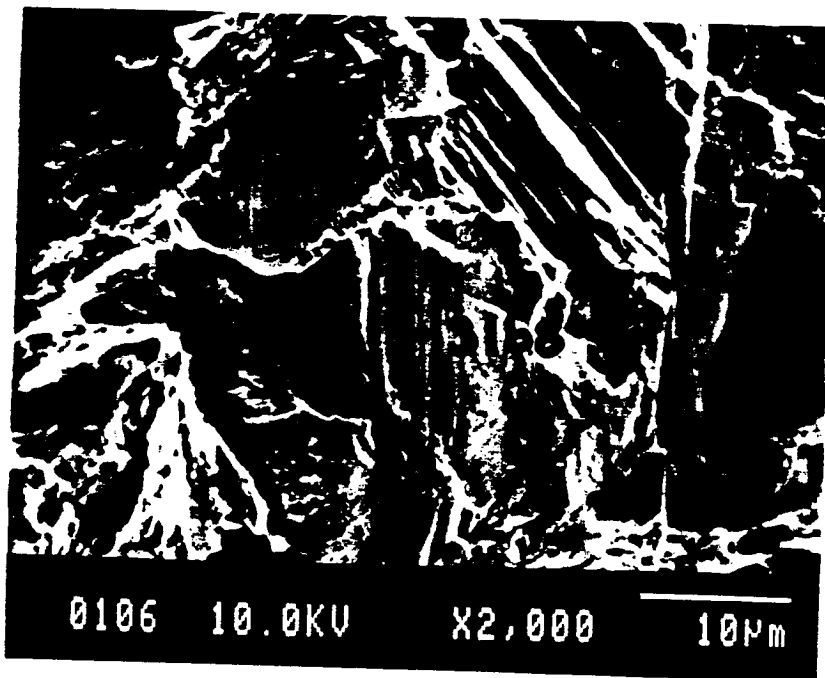
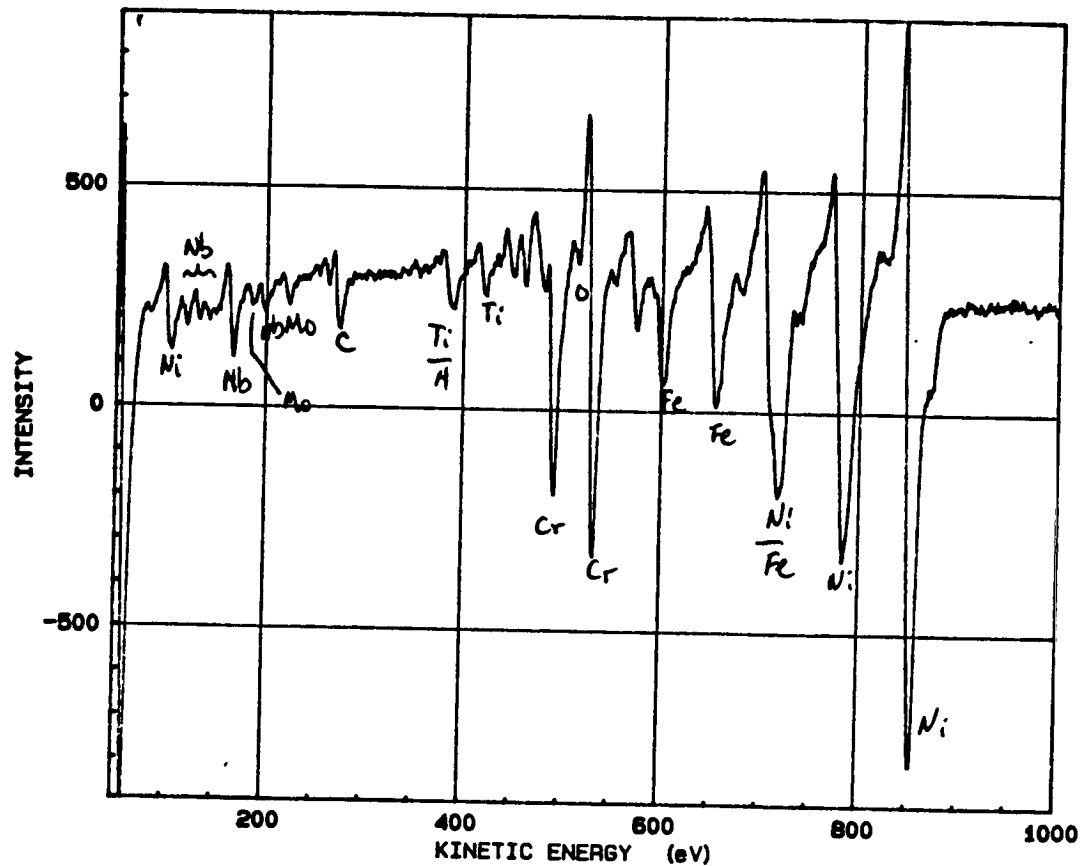
Alloy 12 (BC) Spot #43b10

SAM chemical spectra of freshly fractured matrix surface. Significant levels of none of the dopants are present. Note that C and O are typical system contaminants.



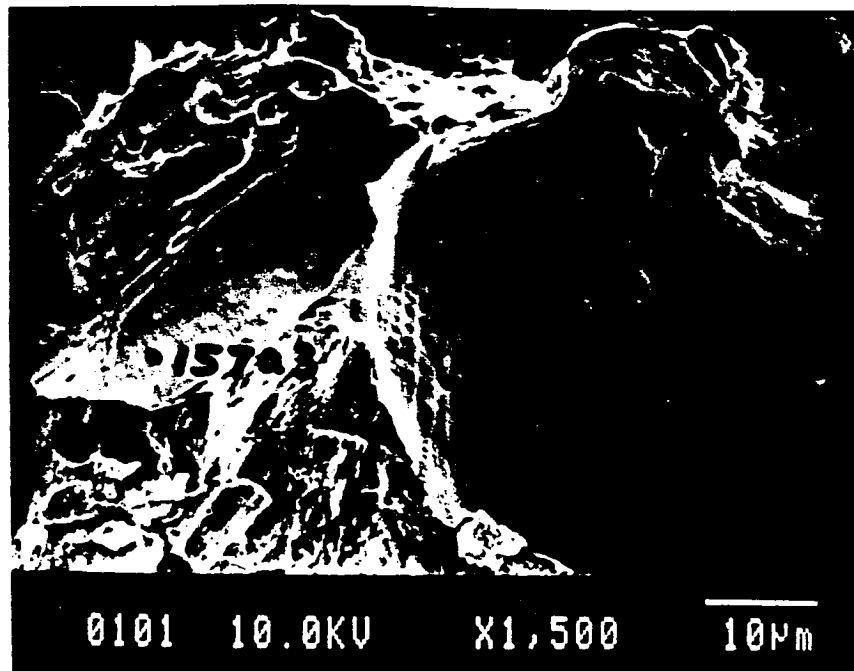
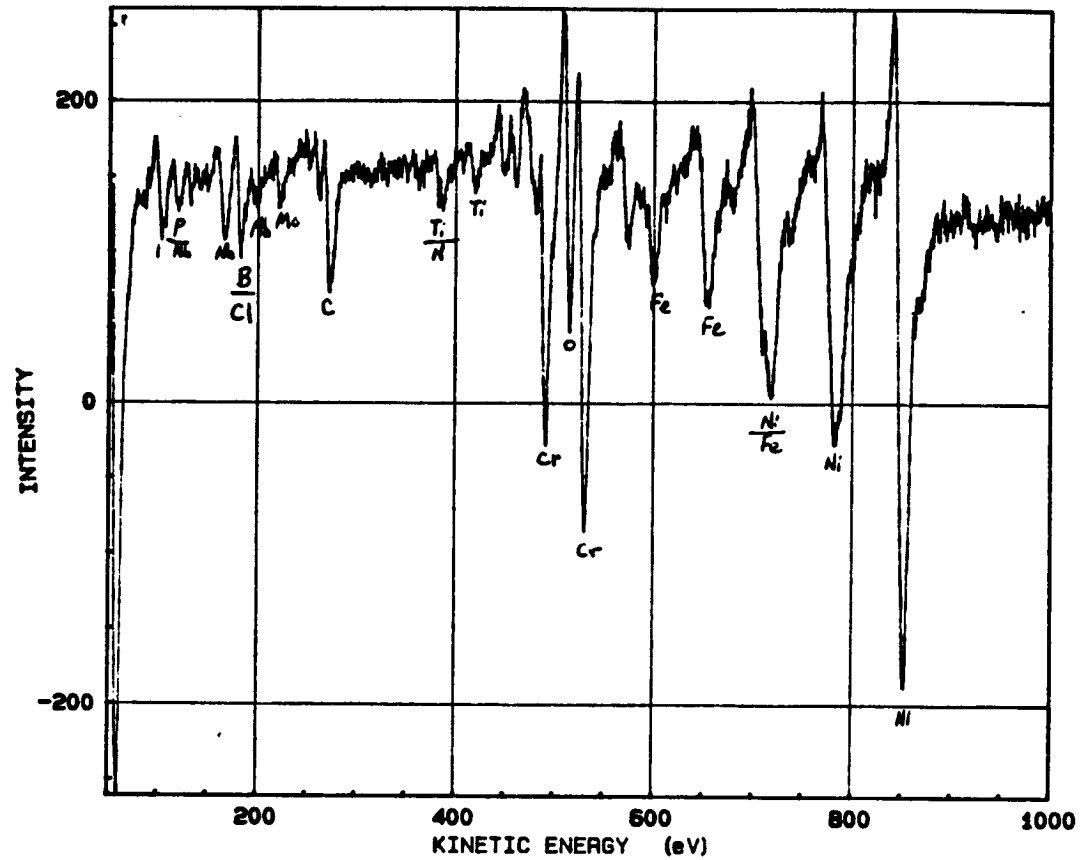
Alloy 13 (B) Spot #31a4

SAM chemical spectra of a freshly fractured grain boundary surface. Significant levels of only B are present. Note that C and O are typical system contaminants.



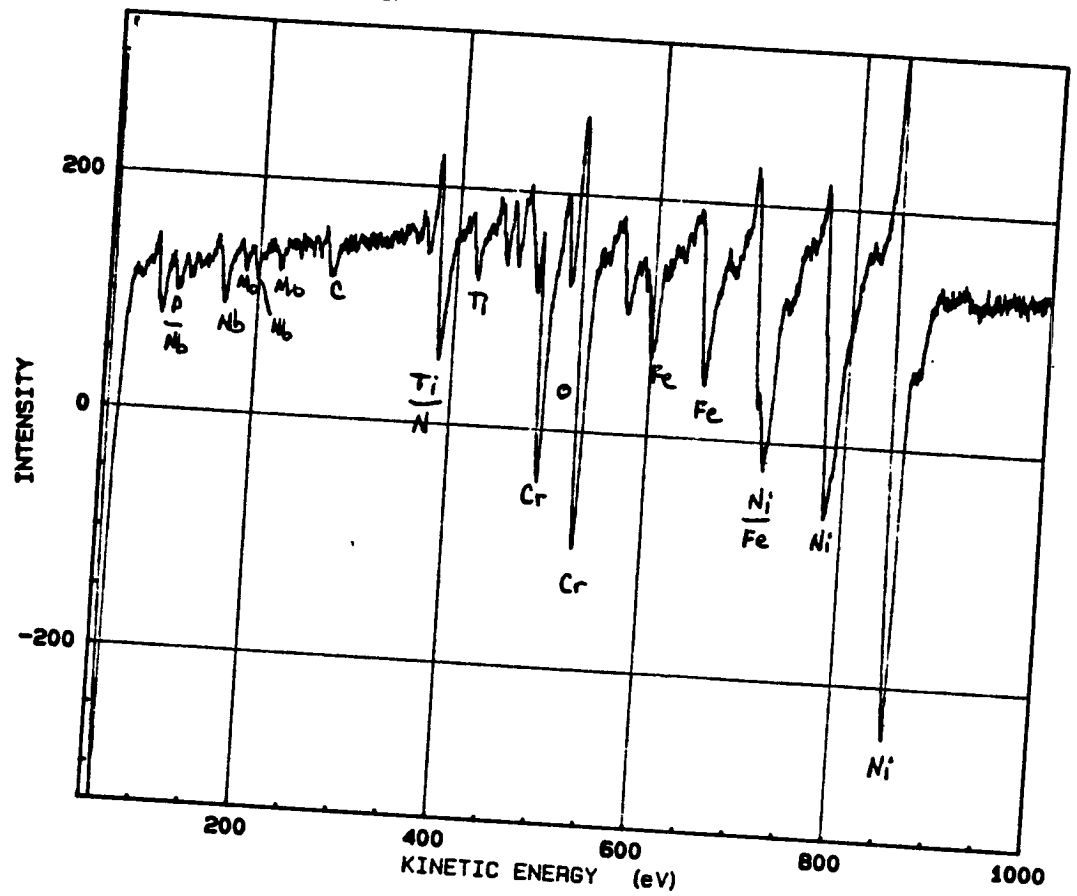
Alloy 13 (B) Spot #31b8

SAM chemical spectra of a freshly fractured matrix surface. Significant levels of none of the dopants are present. Note that C and O are typical system contaminants.



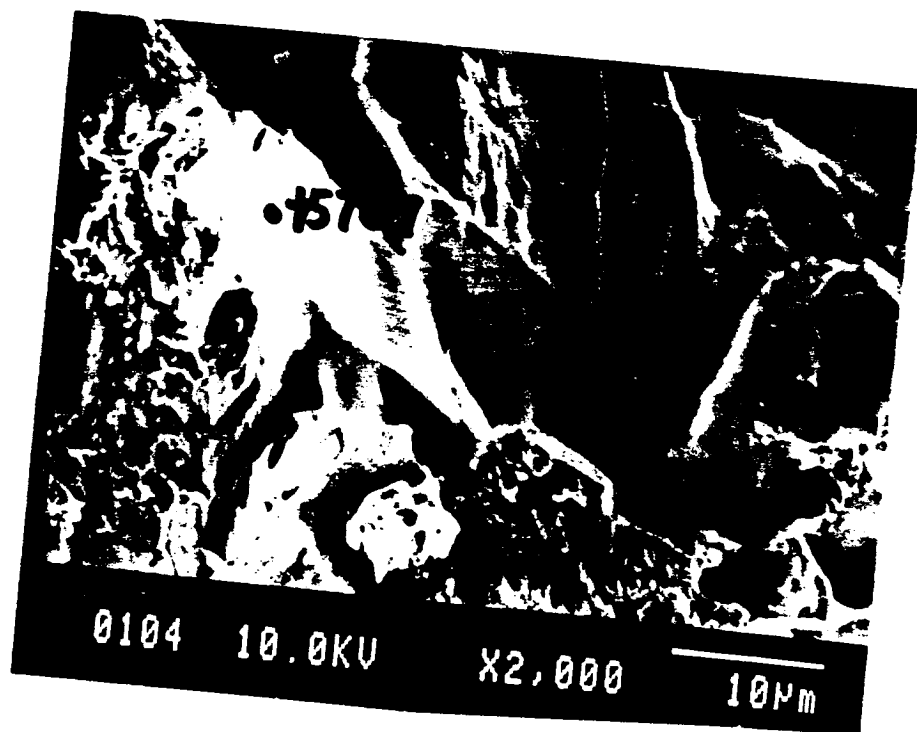
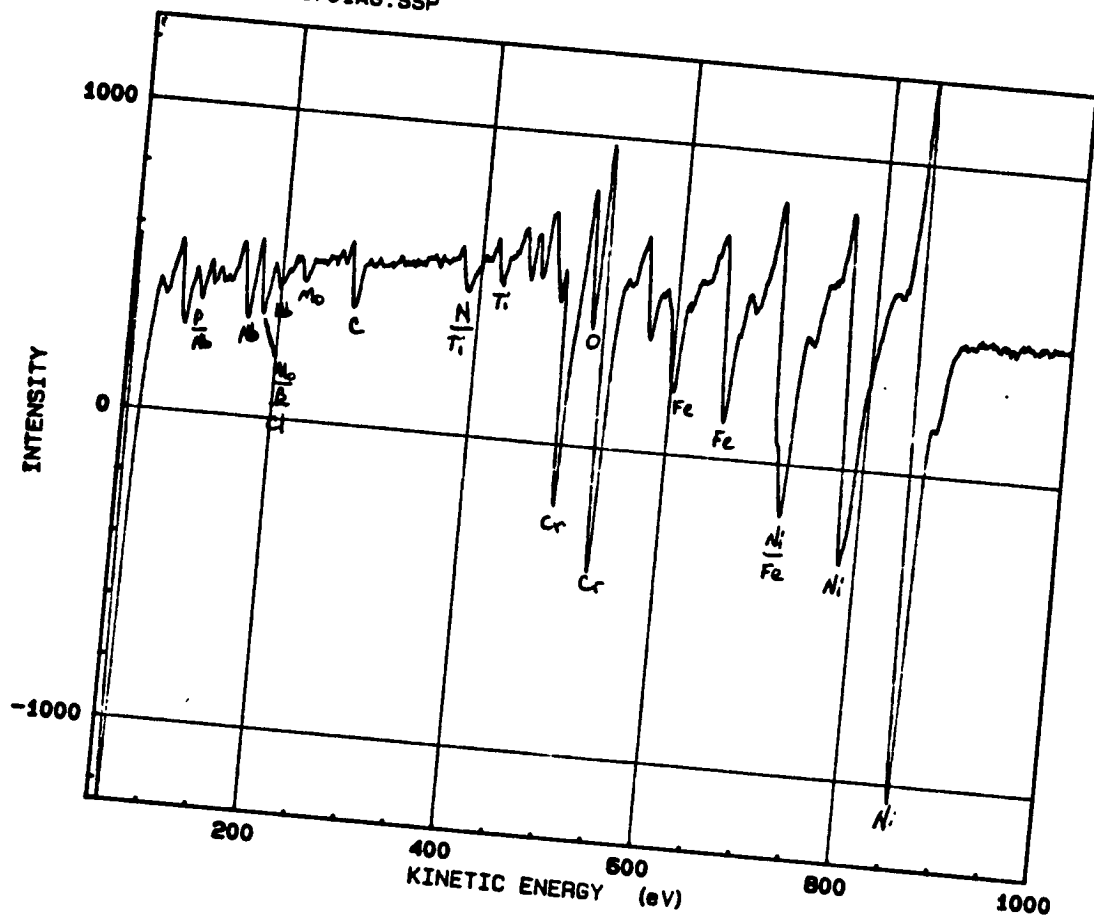
Alloy 20 (clean) Spot #157a3

SAM chemical spectra of a freshly fractured grain boundary surface. Significant levels of only B or Cl (contaminates) are present. Note that C and O are typical system contaminants.



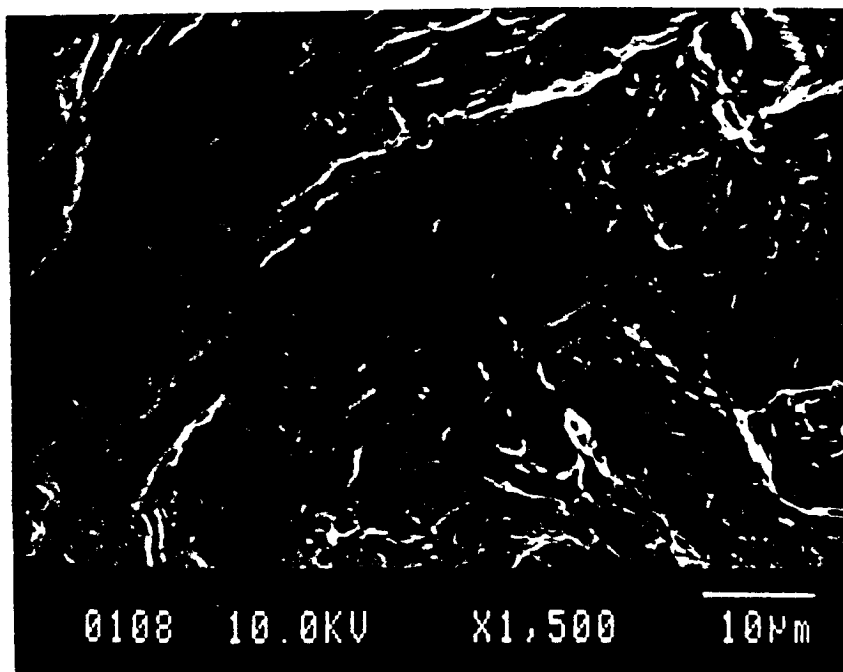
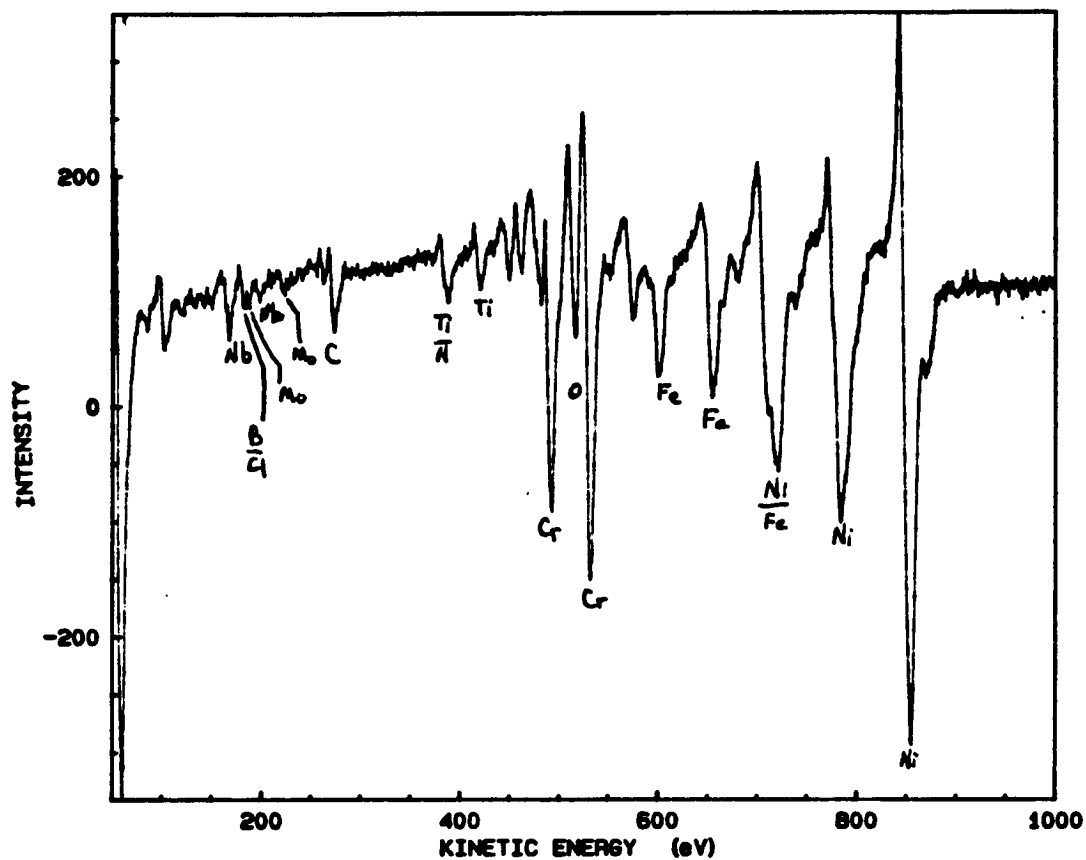
Alloy 20 (clean) Spot #157a3

SAM chemical spectra of the grain boundary surface after sputter cleaning. Significant levels of none of the dopants are present. Note that C and O are typical system contaminants.



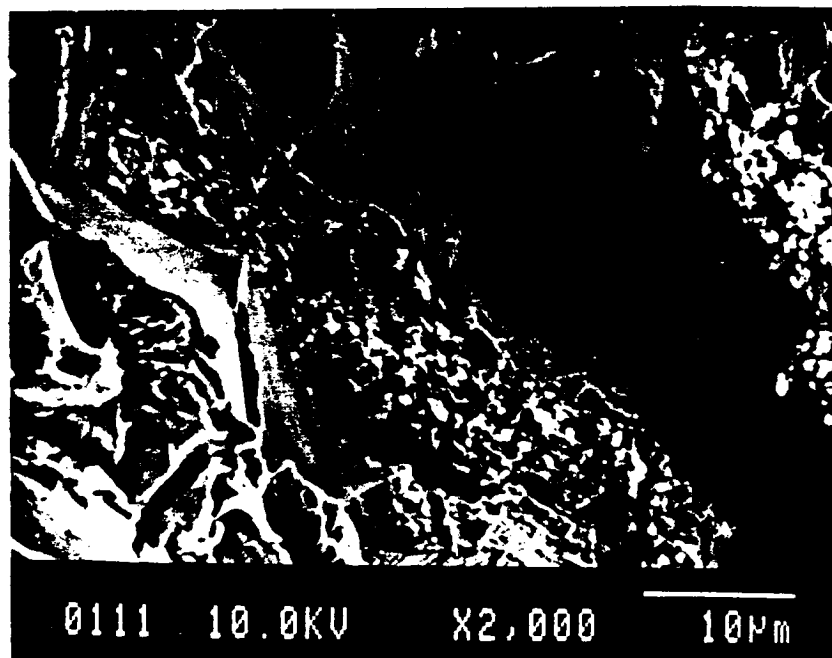
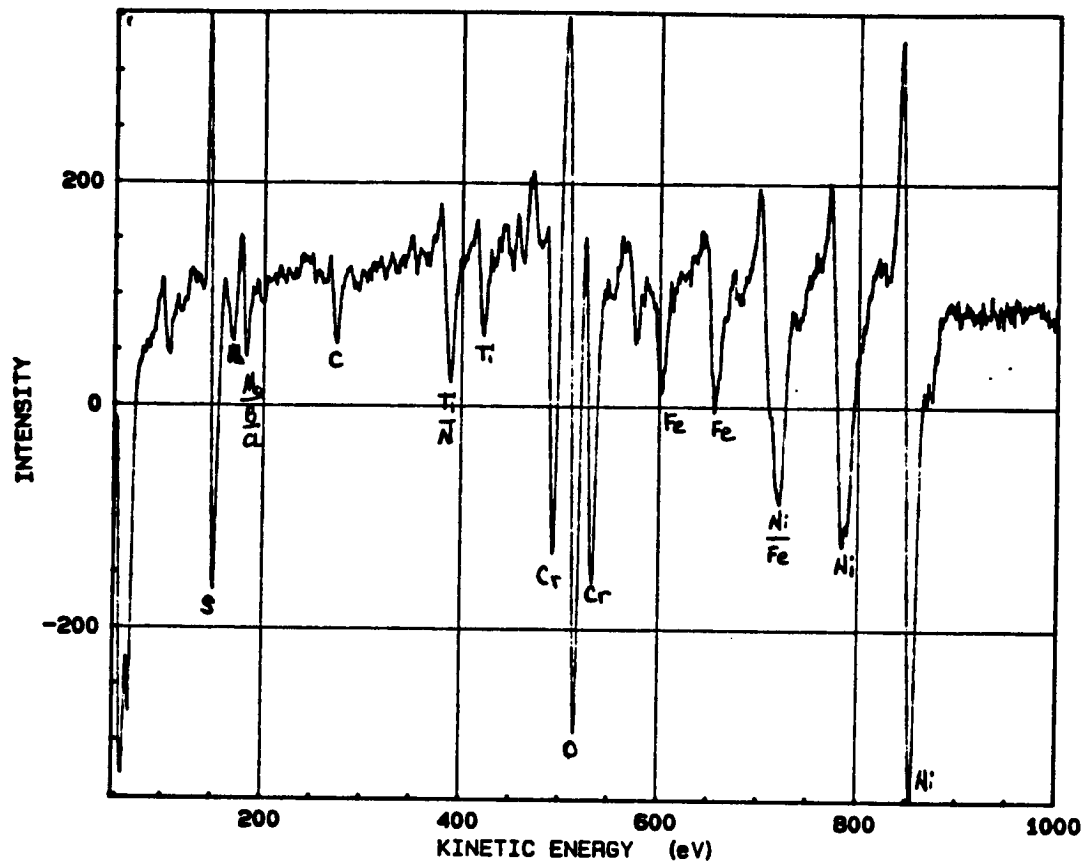
Alloy 20 (clean) Spot #157c7

SAM chemical spectra of the grain boundary surface. Significant levels of only B and Cl (contaminates) are present. Note that C and O are typical system contaminants.



Alloy 20 (clean) Spot #157d12

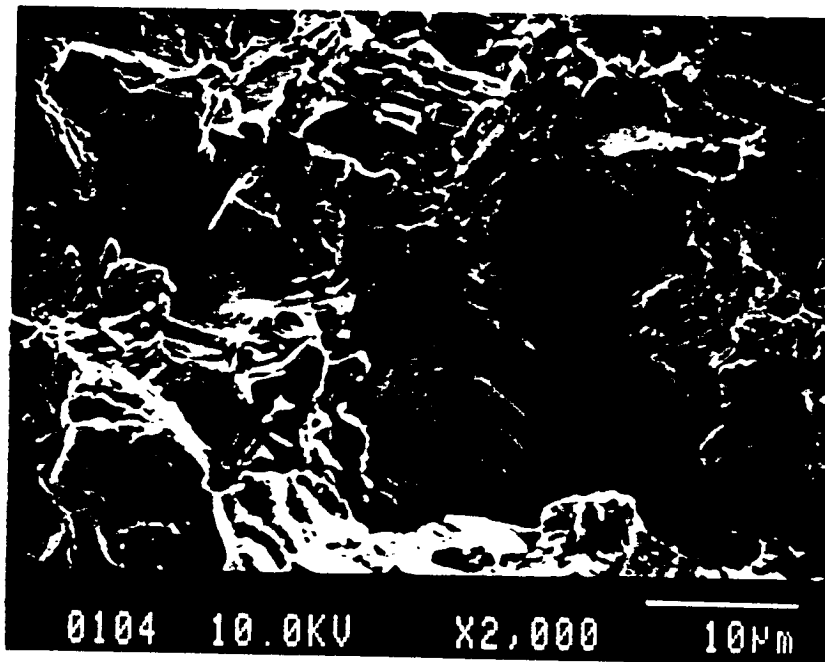
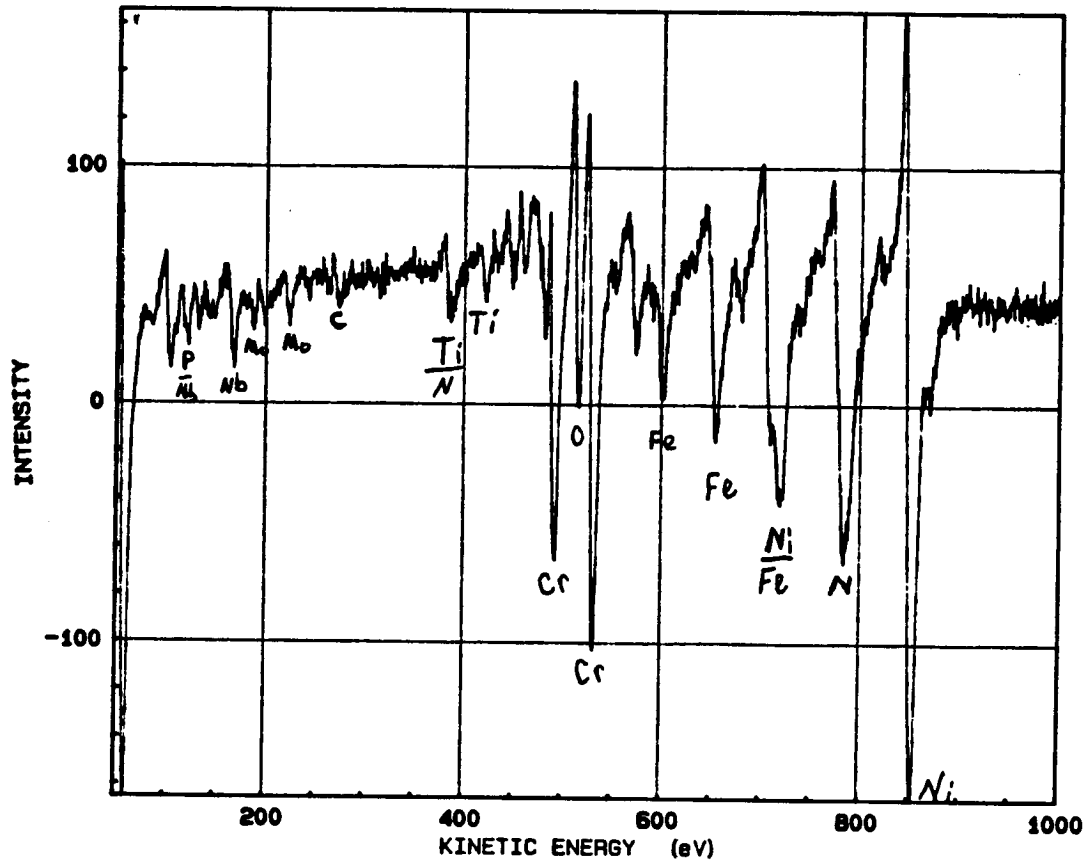
SAM chemical spectra of the matrix surface. Significant levels of only B (small) are present. Note that C and O are typical system contaminants.



Alloy 20 (clean) Spot #157f14

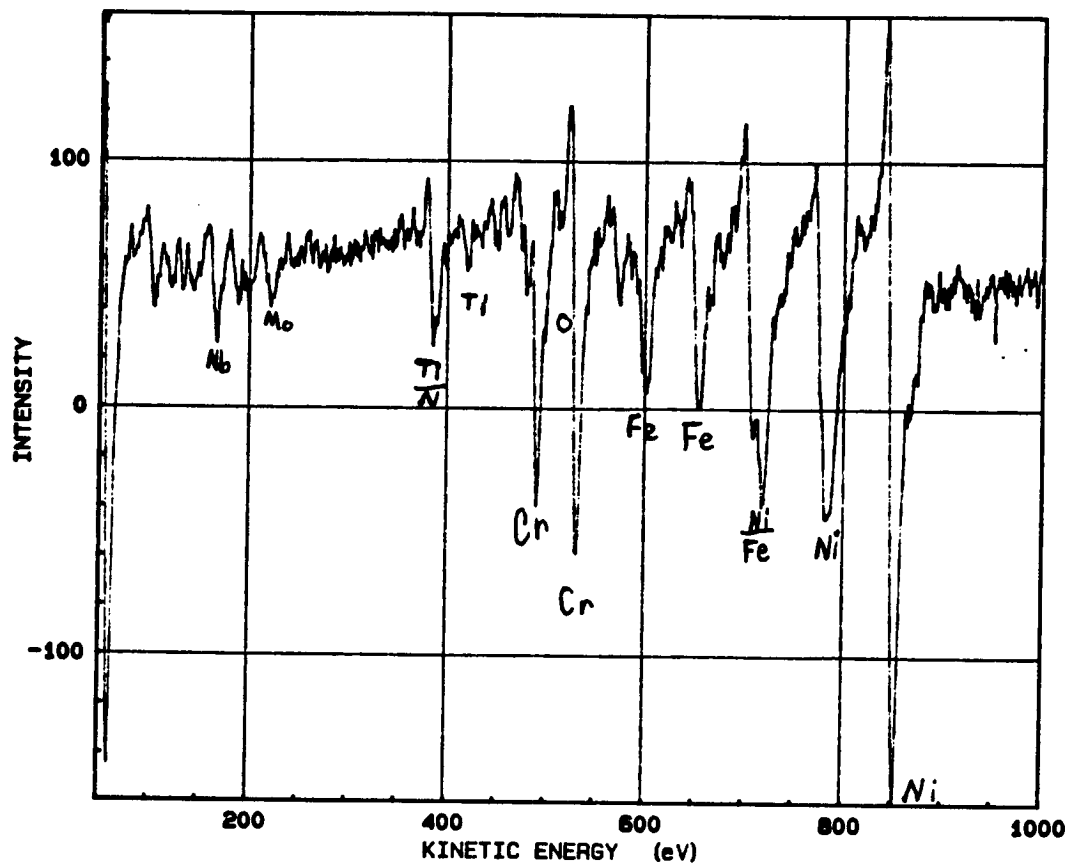
SAM chemical spectra of a freshly fractured precipitate zone surface. Significant levels of only S and B or Cl (contamination) are present. Note that C and O are typical system contaminants.





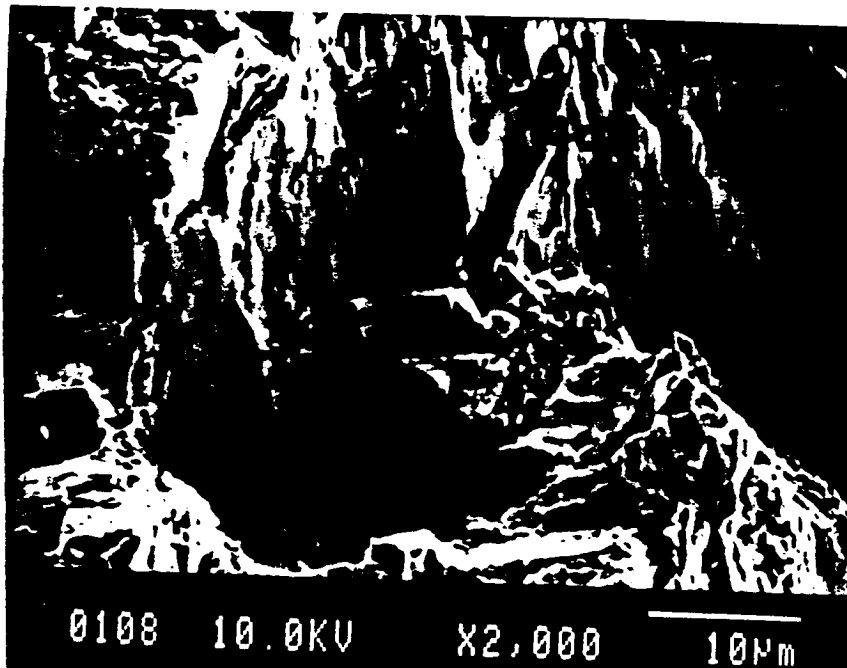
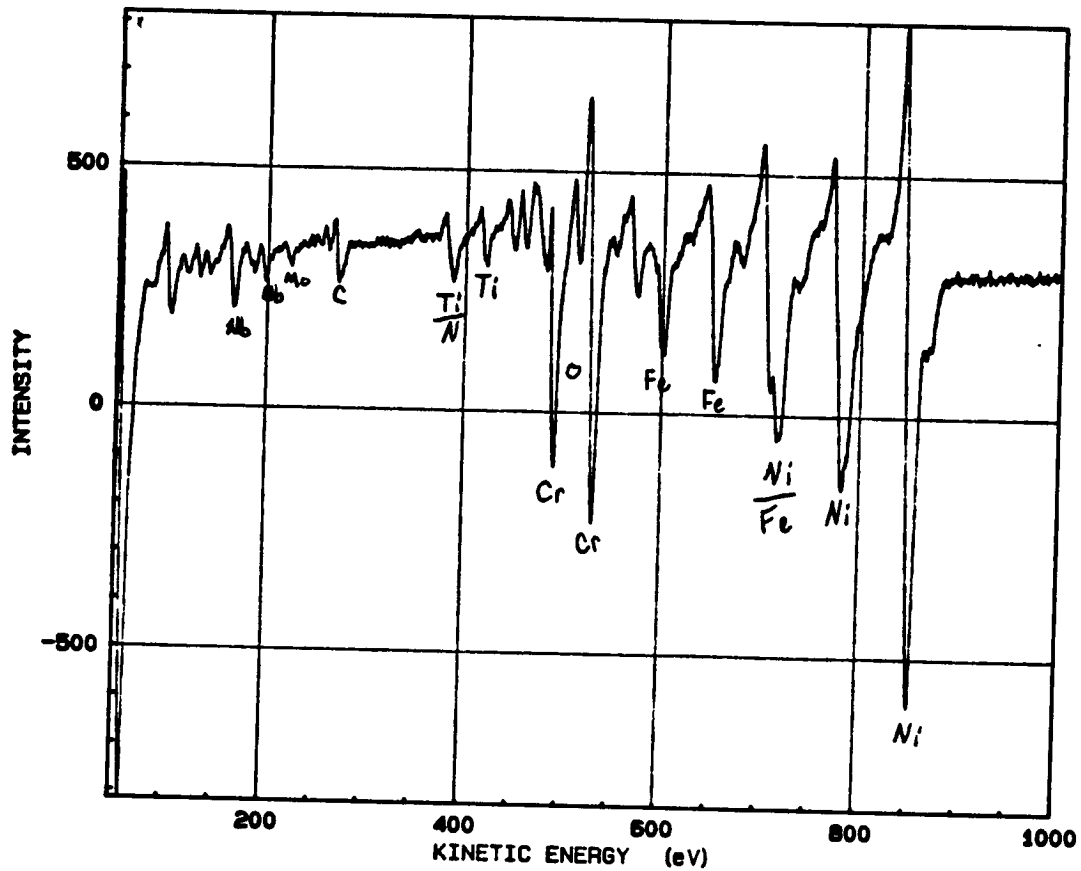
Alloy 22 (C+) Spot #171c6

SAM chemical spectra of a freshly fractured grain boundary surface. Significant levels of S (small) and P (small) are present. Note that C and O are typical system contaminants.



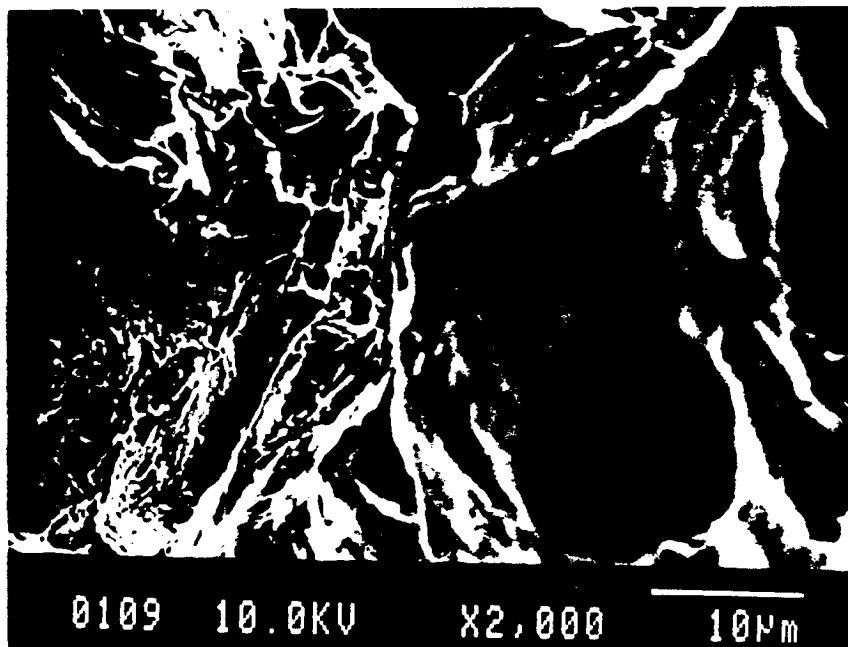
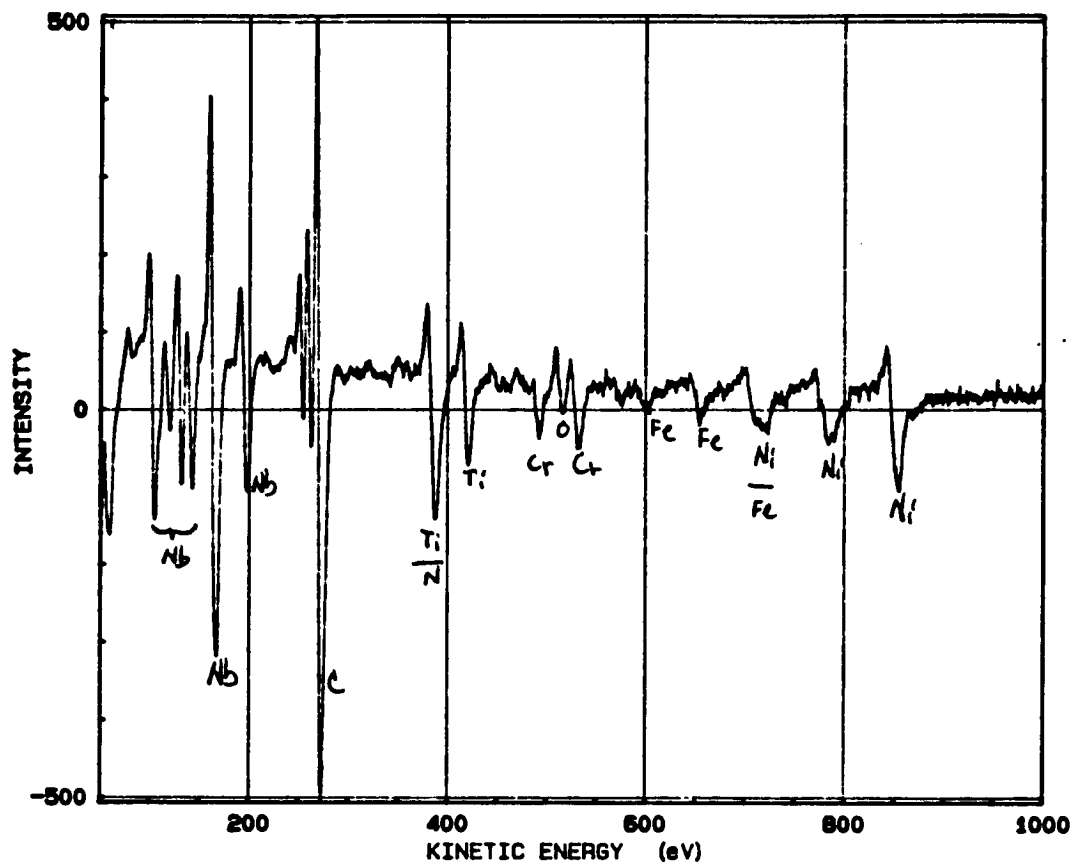
Alloy 22 (C+) Spot #171c6

SAM chemical spectra of the grain boundary surface after sputter cleaning. Significant levels of none of the dopants are present. Note that C and O are typical system contaminants.



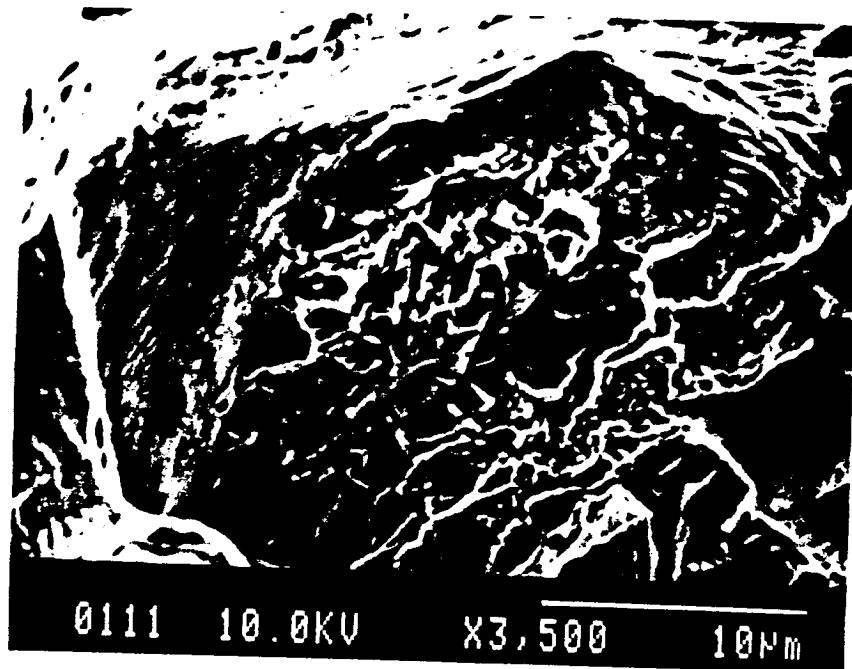
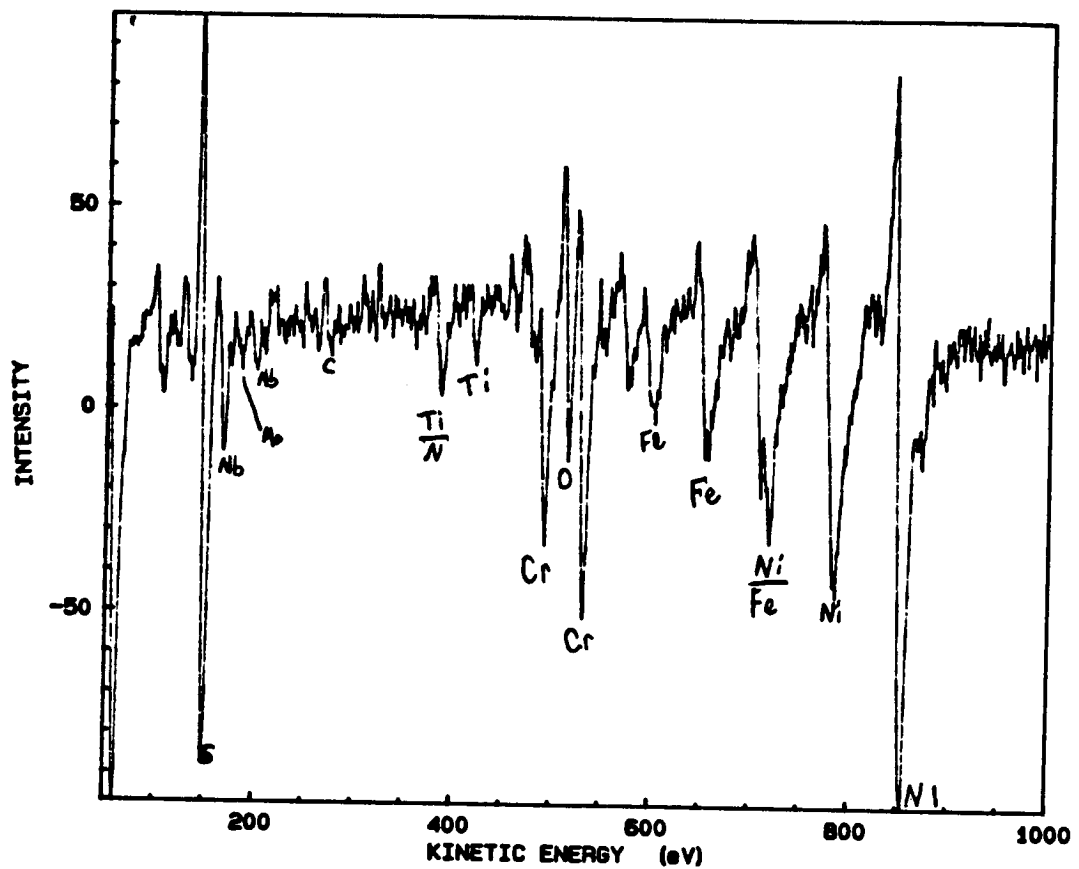
Alloy 22 (C+) Spot #171d8

SAM chemical spectra of the grain boundary matrix surface. Significant levels of none of the dopants are present. Note that C and O are typical system contaminants.



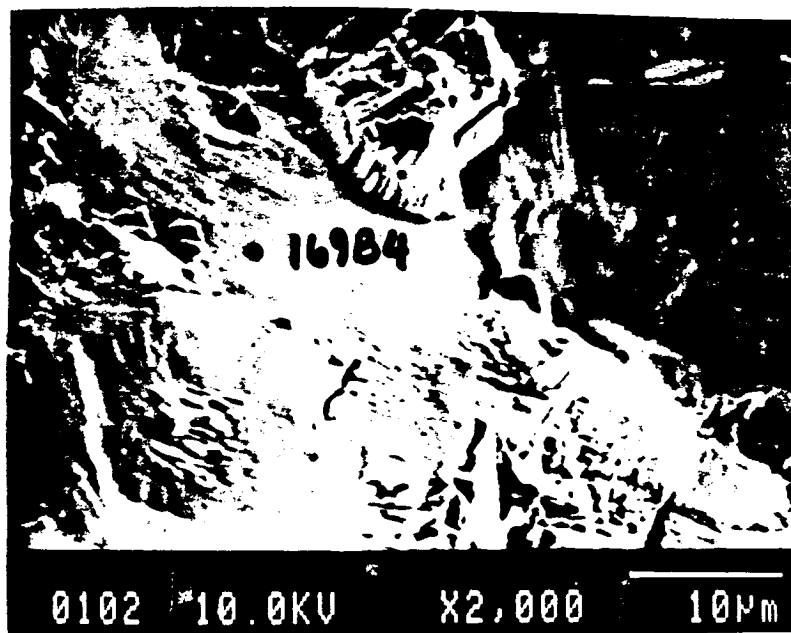
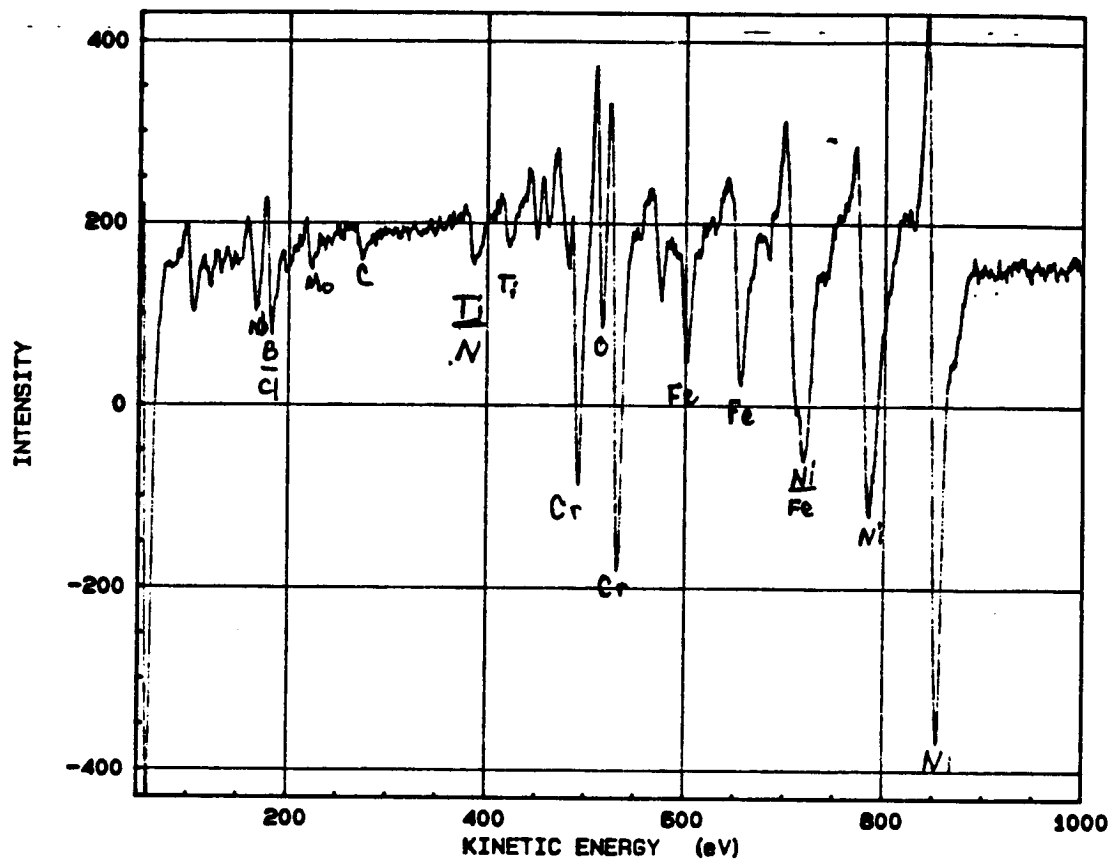
Alloy 22 (C+) Spot #171e9

SAM chemical spectra of a freshly fractured carbide surface. Significant levels of none of the dopants are present. Note that C and O are typical system contaminants.



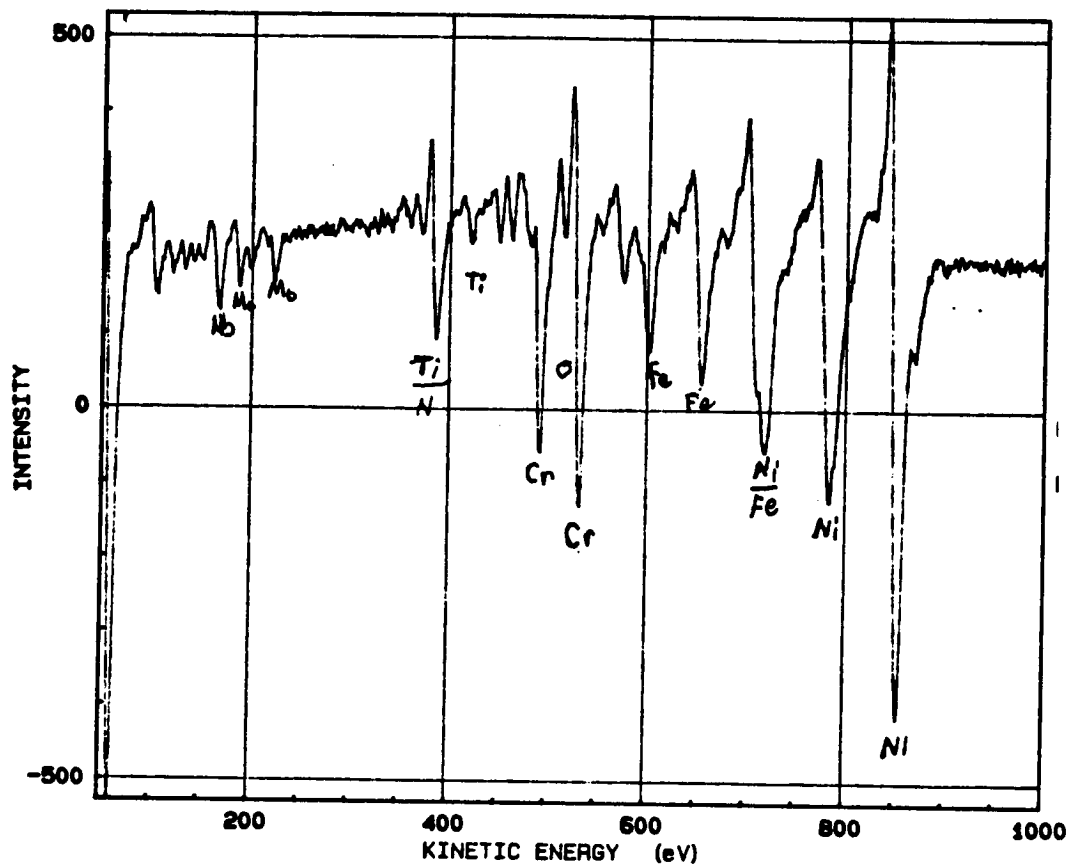
Alloy 22 (C+) Spot #171g12

SAM chemical spectra of a freshly fractured eutectic surface. Significant levels of only S are present. Note that C and O are typical system contaminants.



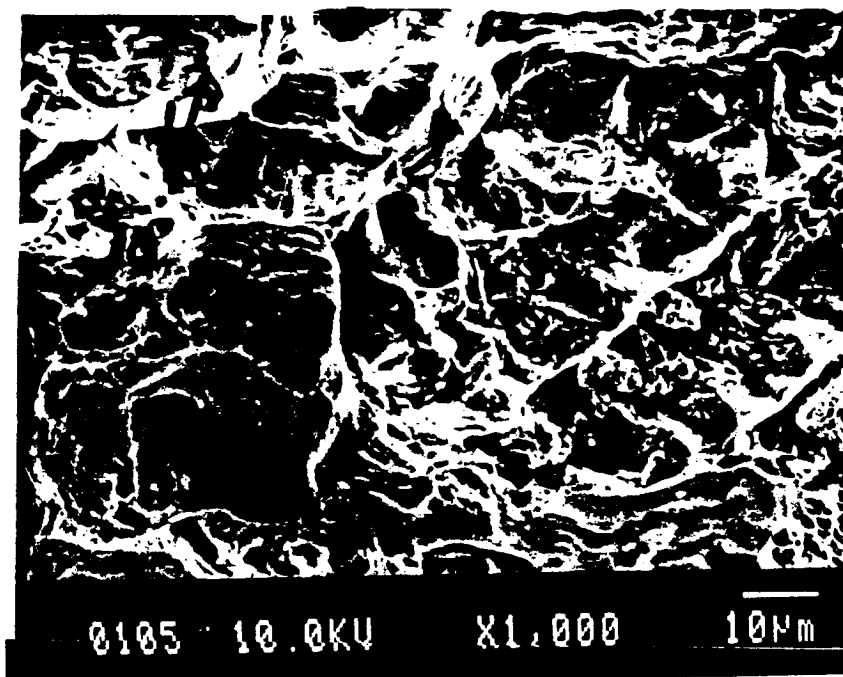
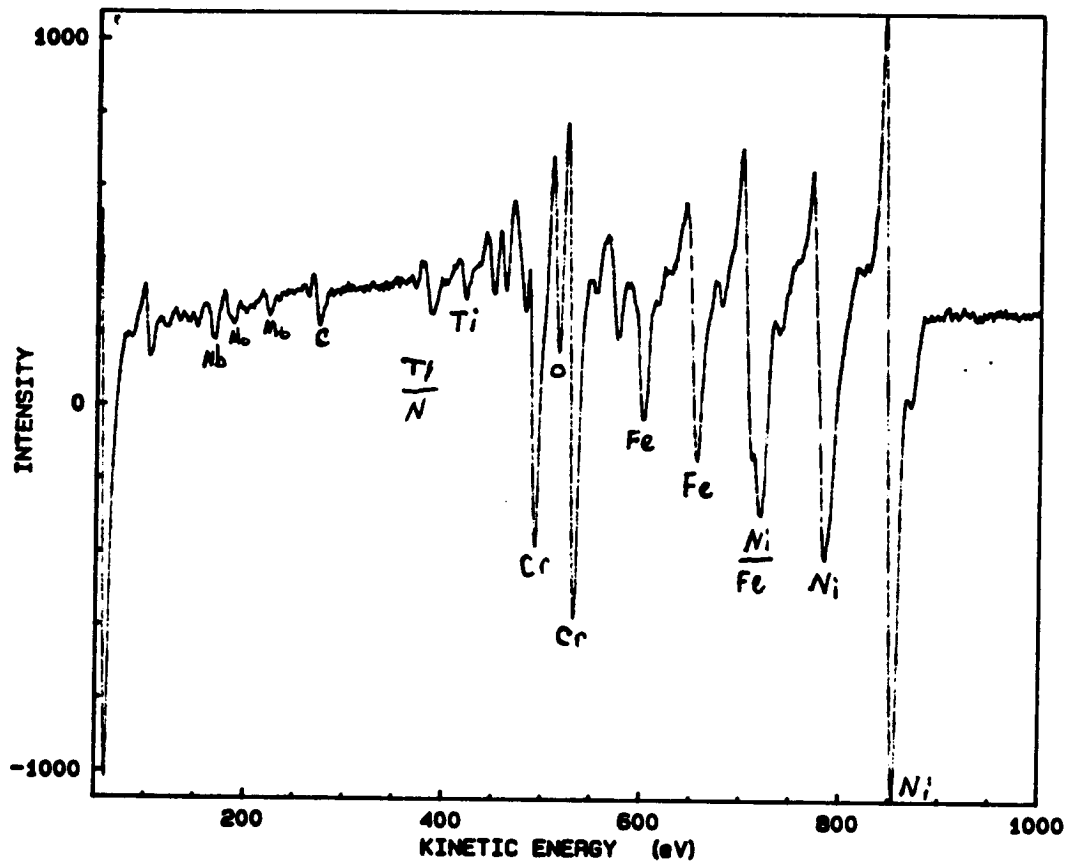
Alloy 25 (S+) Spot #169b4

SAM chemical spectra of a freshly fractured grain boundary surface. Significant levels of only B or Cl (contamination) are present. Note that C and O are typical system contaminants.



## Alloy 25 (S+) Spot #169b4

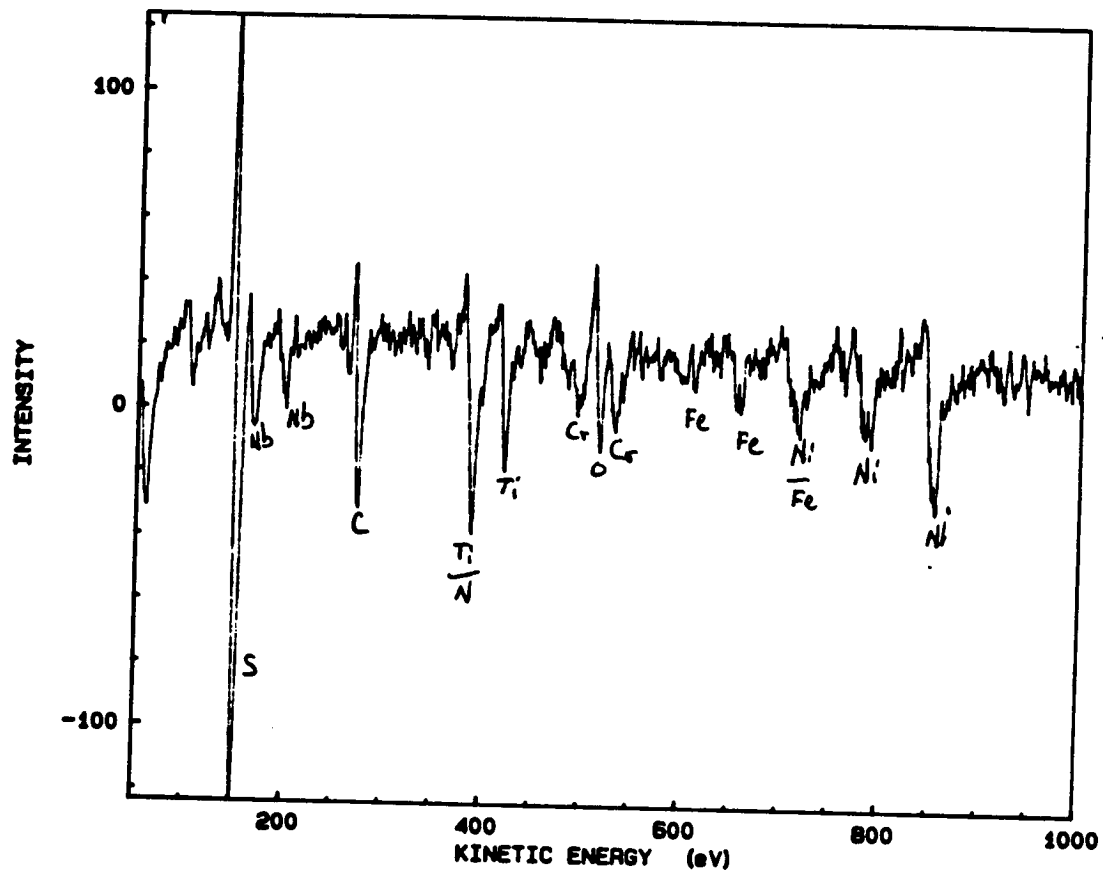
SAM chemical spectra of the grain boundary surface after sputter cleaning. Significant levels of none of the dopants are present. Note that C and O are typical system contaminants.



Alloy 25 (S+) Spot #169d12

SAM chemical spectra of a freshly fractured matrix surface. Significant levels of none of the dopants are present. Note that C and O are typical system contaminants.

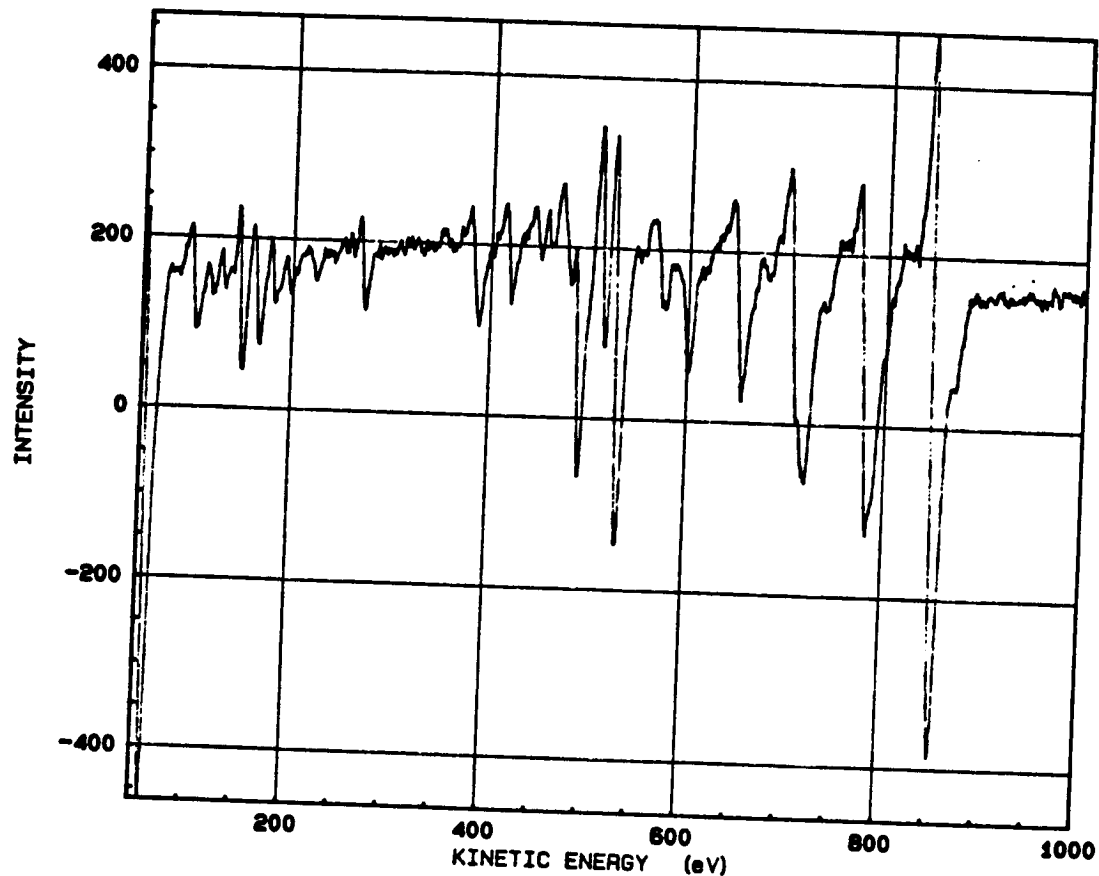




## Alloy 25 (S+) Spot #169d13

SAM chemical spectra of a freshly fractured carbide surface. Significant levels of only S are present. Note that C and O are typical system contaminants.

File : 9016901AE.SSP



Alloy 25 (S+) Spot #169b5

SAM chemical spectra of a freshly fractured eutectic surface. Significant levels of only S are present. Note that C and O are typical system contaminants.